Geochemical characterisation of the widespread Japanese tephrostratigraphic markers and correlations to the Lake Suigetsu sedimentary archive (SG06 core)

Paul G Albert*[a], Victoria C Smith[a], Takehiko Suzuki[b], Danielle McLean[a], Emma L Tomlinson[c], Yasuo Miyabuchi[d], Ikuko Kitaba[e], Darren F Mark[f], Hiroshi Moriwaki[g], SG06 Project Members[e], Takeshi Nakagawa[e]

*Corresponding author: paul.albert@rlaha.ox.ac.uk

[a] Research Laboratory for Archaeology and the History of Art, University of Oxford, Oxford, OX1 3TG, United Kingdom.

[b] Department of Geography, Tokyo Metropolitan University, Minamiosawa, Hachioji, Tokyo, Japan.

[c] Department of Geology, Trinity College Dublin, Dublin 2, Ireland.

[d] Kyushu Research Center, Forestry and Forest Products Research Institute, Kurokami 4-11-16, Kumamoto 860-0862, Japan.

[e] Research Centre for Palaeoclimatology, Ritsumeikan University, Kusatsu, 525-8577, Japan

[f] NERC Argon Isotope Facility, Scottish Universities Environmental Research Centre, Rankine Avenue, East Kilbride, Scotland G75 0QF, UK.

[g] Faculty of Law, Economics and Humanities, Kagoshima University, 1-21-30 Korimoto, Kagoshima 890-0065, Japan.

Abstract

Large Magnitude (6-8) Late Quaternary Japanese volcanic eruptions are responsible for widespread ash (tephra) dispersals providing key isochrons suitable for the synchronisation and dating of palaeoclimate archives across East Asia, the NW Pacific and beyond. The transfer of geochronological information using these eruption deposits demands high-precision and robust tephra correlations underpinned by detailed volcanic glass geochemical fingerprinting. Presented here is a major (electron microprobe; EMP) and trace element (Laser ablation inductively coupled plasma mass spectrometry; LA-ICP-MS) characterisation of near-source deposits from a series of large magnitude Japanese eruptions spanning approximately the last 150 ka. These data offer new insights into diagnostic compositional variations of the investigated volcanic sources spanning the Japanese islands. Whilst in the case of the highly productive Aso caldera (Kyushu), we are able to explore compositional variations through successive large magnitude eruptions (50-135 ka).

These near-source volcanic glass data are used to validate and refine the visible tephrostratigraphy of the intensely dated Lake Suigetsu sedimentary record (SG06 core), Honshu Island, whilst also illustrating key tephrostratigraphic tie points to other East Asian palaeoclimate records (e.g. Lake Biwa). The identification of widespread Japanese tephrostratigraphic markers in the SG06 sediment record enable us to place chronological constraints on these ash dispersals, and consequently explosive volcanism at source volcanoes situated along the Kyushu Arc, including Kikai, Ata and Aso calderas. The proximal Aso-4 Ignimbrite (Magnitude 7.7) deposits is dated here by $^{40}Ar/^{39}Ar$ at 86.4 ± 1.1 ka (2σ), and provides a chronological anchor (SG06-4963) for the older sediments of the Lake Suigetsu record. Finally, trace element glass data verify visible ash fall layers derived from other compositionally distinct source regions of Japanese volcanism, including activity along the northern Izu-Bonin arc and North East Japan Arcs. These findings underline the Lake Suigetsu record as central node in the Japanese tephrostratigraphic framework.

# 1.	Introduction

Understanding the drivers of spatial and temporal variability in the Earth's climate is a major focus of the scientific community. Polar climate records (ice cores) indicate abrupt and dramatic climate oscillations during the last glacial cycle (e.g., Dansgaard et al., 1993; Anderson et al., 2004; Steffensen et al., 2008), however to better understand the mechanisms behind these changes it is crucial to assess whether these event were as abrupt in the mid-latitudes, and if they were globally synchronous. The annually laminated (varved) and intensely ^{14}C dated sediments of Lake Suigetsu (SG06 core), Honshu Island, Japan, presents a unique record of East Asian palaeoclimate (e.g., Nakagawa et al., 2003; 2012; Bronk Ramsey et al., 2012). It is therefore essential to directly compare this key mid-latitude palaeoclimate record with those from higher latitudes to better understand the forcing mechanisms controlling past climate fluctuations.

Volcanic ash (tephra) layers preserved in the sediments of Lake Suigetsu from explosive eruptions all over Japan provide a key tool to link this palaeoclimate records with others across the SE Asia and beyond. The near synchronous deposition of tephra following explosive eruptions means it offers important time-parallel stratigraphic markers suitable for synchronisation of disparate climate archives and assessing the spatio-temporal variations in past climate (e.g., Lane et al., 2013). Furthermore, where the age of a tephra layers is established they can provide crucial chronological constraints to the host sediments. Distal tephra layers are often dated through precise correlations to directly dated near source eruption units (e.g., ^{40}Ar/^{39}Ar; ^{14}C). Conversely, tephra deposits are increasingly being indirectly dated using the varve (annual layering) or radiocarbon chronologies of precisely dated sedimentary records (e.g., Wulf et al., 2004; 2012; Albert et al., 2013; Smith et al., 2013; Tomlinson et al., 2014; Plunket et al., 2015). The chronology of the Lake Suigetsu sedimentary archive (SG06) can therefore be unlocked and exported into other distal sedimentary archives using co-located tephra layers. The increasing number of cryptotephra (non-visible) studies far from volcanic source are greatly extending the geographical extent of ash fall from individual eruptions, and consequently their application as tephrochronological markers (e.g., Pyne-O'Donnell et al., 2012; Jensen et al., 2014; Bourne et al., 2016; McLean et al., 2018). Robust tephra correlations depend upon strong stratigraphic and chronological lines of evidence, but must be underpinned by detailed glass geochemistry, essential for the reliable exchange of geochronological information between disparate records.

In order to facilitate tephra correlations centred on the key Japanese tephrostratigraphic markers we integrate new grain-specific major (EMP) and trace element (LA-ICP-MS) near-

source and medial volcanic glass data, with a new trace element datasets for the visible SG06 tephra layers. These data are used to assess compositional variability spanning the Japanese Islands, important for determining the provenance of unknown tephra deposits of Japanese origin. The near source geochemical data are used to validate and refine the tephrostratigraphy of the SG06 record, which is essential for unlocking the chronology of this key archive. Proximal $^{40}Ar/^{39}Ar$ dating of Aso-4 deposits provide the opportunity to exert new chronological constraints on the Lake Suigetsu sedimentary archive, which is important for constraining the ages of other important tephra units in close stratigraphic succession.

1.1 Japanese volcanic arcs and sources of Late Quaternary widespread tephra

Volcanoes along the islands Japan are formed as the result of subduction along the Ryukyu-Kyushu Arc, the SW Japan Arc (SWJA), the NE Japan Arc (NEJA) and the Kurile Arc (**Fig. 1**). The Philippine Sea Plate is moving northwest and descends along the Ryukyu-Kyushu Arc and SWJA (Zhao et al., 2012; Kimura et al., 2015). The subduction of the Philippine Sea plate beneath Kyushu Island can be spatially subdivided with the occurrence of both back-arc and forearc volcanism (Mahony et al., 2011). Calderas dominate along the volcanic front of Kyushu Island, whilst the back-arc is dominated by stratovolcanoes and monogenetic centres (Yoshida et al., 2013). Mahony et al., (2011) further divide the volcanism along the Kyushu volcanic front into a southern and central volcanic region on the basis of shared tectonic evolution, and are separated by a non-volcanic area (**Fig. 1**). The Kyushu Southern Volcanic Region (SVR) includes Late Quaternary calderas (Kikai, Ata, Ikeda, Aira), and extends as far north as Kirishima volcanic complex (**Fig. 1**). The Kyushu Central Volcanic Region (CVR) is comprised of Aso Caldera, and the Hohi Volcanic Zone (HVZ) that includes the Kuju volcanic complex, Yufu and Tsurumi volcanoes (**Fig. 1**). The Kyushu CVR represents an area of higher potassium volcanism relative to that of the SVR, owing to a combination of extensional tectonics and the subduction of the fluid-rich Kyushu-Palau ridge (Mahony et al., 2011). Further north-east subduction of the Philippines plate beneath SW Honshu results in rear-arc volcanism, and owing to lower rates of magma production calderas are absent, with Late Quaternary explosive activity concentrated at stratovolcanoes, specifically Daisen and Sambe (Kimura et al., 2015). Volcanism at Hakone caldera in central Honshu is attributed to collision along the intra-oceanic Izu-Bonin arc where the Pacific plate meets the Philippine Sea plate. North-west of Hakone is the iconic Mount Fuji, which sits in a complex tectonic setting at the junction between the Izu-Bonin collision and the NEJA and may also be influenced by subduction of the Philippines slab (Wantabe et al., 2006; Tani et al., 2011).

Along the NEJA beneath northern Honshu and SW Hokkaido the Pacific plate is subducting in a north-westward direction. During the Late Miocene and Pliocene the NEJA was dominated by large caldera volcanism, during the Quaternary there is a shift to a prevalence of stratovolcanoes, however a small number of Quaternary calderas are situated in the forearc region of the NEJA (Kimura and Yoshida, 2006; Acocella et al., 2008; Kimura et al., 2015). Higher eruption rates are recognised at NE Japan forearc volcanoes as appose to those in the rear-arc (Kimura, 1996). Late Quaternary calderas situated along the NEJA include Towada (Northern Honshu), Shikotsu and Toya (Hokkaido). Calderas on NE Hokkaido (e.g., Kutcharo, Mashu) are related to the Kurile Arc and the subduction of the Pacific plate beneath the Okhotsk plate (Razzhigaeva et al., 2016). Overall the complex interaction of tectonic plates causes intense volcanic activity in and around the Japanese Islands; there are more than 110 active forearc and rear-arc volcanoes (Zhao et al., 2012).

Numerous large caldera forming eruptions have occurred from volcanoes on Kyushu, NE Honshu and Hokkaido during the Late Quaternary. Magnitude (M) estimates for these events are classified following the method of Pyle (2000), and place them between M6.0-7.9 (Machida and Arai, 2003; Hayakawa 2017; Crosweller et al., 2012 [LaMEVE database]; **Table 1**). These eruptions are responsible for widespread ash dispersals mapped across the Japanese islands, the Sea of Japan, and across the Pacific Ocean (Machida and Arai, 2003; **Fig. 1**). In the Kyushu SVR Kikai caldera south of Kyushu island is the product of two large magnitude eruptions the last ca.100 ka, the Kikai Akahoya (K-Ah) is one of the largest Holocene eruptions globally (M 7.3), and is dated at between 7,165-7,303 cal yrs BP in SG06 (Smith et al., 2013), while the older M 6.0 eruption Kikai Tozurahara (K-Tz) is loosely dated at between ca. 90-95 ka (Machida 1999, Machida and Arai, 2003; Hayakawa 2017). Further to the north-east is Ata caldera (*Ibuski volcanic field*), which was at least partly generated during the M 7.5 eruption at ca.100 ka (Machida and Arai, 2003). The smaller Ikeda caldera resides in the western sector of the Ata caldera and is the product of the Ikeda M 5.4 eruption (**Table 1**). Aira caldera was produced during the enormous M 7.9 eruption which ejected approximately 463 km^3 of bulk tephra, and is most precisely dated at 30,009 ± 189 cal yrs BP in SG06 (Smith et al., 2013). Prior to the AT tephra, the Iwato eruption from somewhere within the Aira caldera produced ignimbrite units dated at ca. 55 ka (Machida and Arai, 2003). The highly active Sakurajima stratovolcano has more recently developed in the southern portion of the Aira caldera.

Further north-east in the Kyushu CVR, Aso has been a highly productive centre during the Late Quaternary with numerous Plinian eruptions of M4 or greater. These Plinian activities have been punctuated by four caldera forming M6.0 to 7.7 eruptions, Aso-1 to Aso-4 (Machida and Arai, 2003; LaMEVE database). The Aso caldera today is the product of the

M7.7 Aso-4 eruption dated at between 86.8-87.3 ka, based on its stratigraphic position in the MIS5b sediments of the northwest Pacific (Aoki, 2008). Chrono-stratigraphically between Aso-4 and the penultimate caldera forming eruption Aso-3 (123-135 ka), at least 8 Plinian fall deposits are identified outside the caldera (Ono et al., 1977). A series of post-caldera Plinian eruptions of the Aso central cones are reported after the Aso-4 eruption and have estimated ages of 60-51 ka (Miyabuchi, 2009). North-east of Aso caldera is the Hohi Volcanic Zone (HVZ), the most productive centre, producing the thickest and most widely dispersed Late Quaternary eruption deposits is the Kuju volcanic complex (Machida and Aira, 2002). The Kuju Handa Ignimbrite and associated Kuju-Pumice 1 fall, which is classified as M5.3 and dated at ca. 53.5 ka (Okuno et al., 2017).

The majority of Late Quaternary explosive volcanism that has occurred along the SWJA is concentrated at Daisen and Sambe stratovolcanoes and has been restricted to Magnitude 5 eruptions. The most widespread tephra dispersals at these volcanoes are associated with the magnitude 6.5 Daisen Kurayoshi Pumice (DKP) recently dated at 59.6 ka (Albert et al., in press) and the Sambe Kisuki (SK; ca.100 ka; Machida and Arai, 2003; Kimura, 1999). The stratovolcanoes of the Norikura volcanic zone (e.g., Ontake and Tateyama) at the southern end of the NEJA have experienced some large explosive eruptions but again these are restricted to Magnitude 6 events, most noticeable in magnitude are the eruptions of Ontake-Pumice 1 (On-Pm1; ~95 ka; **Table 1**). Southeast of Ontake, at the northern limit of the Izu-Bonin arc lies Hakone caldera, a succession of large magnitude eruptions are reported as occurring between ~250-100 ka based on their stratigraphic position in marine successions (Machida, 2008).

Further north along NEJA, Towada volcano is responsible for many widespread ash dispersals, with the largest relating to the most recent caldera forming Magnitude 6.7 eruption, Towada Hachinohe (To-H) (Hayakawa, 1985; Ikehara et al., 2017; Bourne et al., 2016). On SW Hokkaido the largest eruptions of the last 150 ka are associated with caldera forming activities at Shikotsu-1 (Spfa-1) and Toya (Toya-2) respectively (Machida and Arai, 2003). Whilst in NE Hokkaido, at the southern-most extent of the Kurile Island Arc, large explosive eruptions (M6-7) are related to the formation of Kutcharo caldera and include the Kurcharo-Shorro (Kc-Sr [or Kc-1]), Kutcharo-2/3 and Kutcharo-Hb (Kc-Hb [or Kc-4]) from youngest to eldest (Machida and Arai, 2003). Explosive activity during the early Holocene saw the formation of the Mashu caldera (Mashu-f), located on the eastern side of Kutcharo caldera (Kishimoto et al., 2009).

1.2 Lake Suigetsu (SG06)

Lake Suigetsu, Honshu Island (35º35'0''N, 135º53'0''E) is located in a small tectonic basin situated on the western side of the Mikata fault line, adjacent to Wakasa Bay. It forms the largest of the 'Mikata Five Lakes'. The catchment of the lake is small and is vegetated by warm mixed-forest and is bound by a ring of Palaeozoic hills (maximum elevation 400 m) (Yasuda, 1982; Kitagawa et al., 1995; Nakagawa et al., 2005). The main tributary feeding the five Mikata lakes is the River Hasu, which enters on the south-east side of Lake Mikata. Water feeds from Lake Mikata into Lake Suigetsu via the Seto channel, this shallow channel creates a natural coarse sediment filter meaning that only fine grained autochthonous and authigenic material enters Lake Suigetsu (Schlolaut et al., 2012). The sedimentary environment is particularly stable and allows for continuous fine-grained deposition.

The Suigetsu lake sediments have been studied for over two decades, with the 'SG93' coring campaign leading to increased interest in the sediment record (Kitagawa and van der Plicht, 1998). The SG93 coring revealed that a significant portion of the sequence contained varves ('nenko') i.e. seasonal laminations, with alternations of diatom-rich (darker coloured) and mineral-rich (lighter coloured) layers (Fukusawa, 1995; Kitagawa et al., 1995; Kitagawa and Van der Plicht, 1998). In the summer of 2006 the Lake was re-cored as part of the 'Lake Suigetsu Varved Sediment Project' with the aim to obtain a complete overlapping 'master' sediment sequence by recovering cores from four parallel boreholes (A, B, C and D, situated ~20 m apart) (see Nakagawa et al., 2012). This coring campaign successfully obtained a 73.19 m-long composite core ('SG06'), providing a continuous record of sedimentation spanning the last ~ 150 ka (Nakagawa et al., 2012). The sequence is varved between ~ 10 and 70 ka and has been extensively radiocarbon (^{14}C) dated and the varves have been counted to generate a high-resolution chronology (Staff et al. 2011, Bronk Ramsey et al., 2012; Marshall et al., 2012; Schlolaut et al., 2012) for this high-resolution palaeoenvironmental record.

The majority of the visible tephra layers preserved in the SG06 core are calc-alkaline (CA) to High-K calc-alkaline layers of Japanese arc origin (Smith et al., 2013). These tephra layers range in composition from basaltic through to rhyolitic ash units, which dominate and many have overlapping major element glass chemistries (**Fig. 2**). There are visible tephra layers derived from explosive eruption of Ulleungdo Island, South Korea (Smith et al., 2011; 2013; McLean et al., 2018), and Changbaishan on the North Korea/China border (McLean et al., 2016). The trace element compositions of a number of visible tephra layers in the SG06 core from Daisen and Sambe volcanoes, have been thoroughly analysed (Albert et al., in press). The proximity of these volcanoes to Lake Suigetsu and the prevailing westerlies mean many of the M<=5 eruptions are preserved in the lakes sediments (Albert et al., in press). The major and trace element volcanic glass chemistries of the SG06 visible tephra indicate nine

layers are from explosive activity of Daisen volcano, and five layers are from Sambe (Albert et al., in press). This facilitated the construction of a detailed eruption event stratigraphy for these two stratovolcanoes located along the South-west Japan Arc (SWJA).

2. Samples and Methods

2.1 Proximal-medial reference glass samples

Proximal and medial pumice/ash samples from large magnitude eruptions were collected to generate a detailed glass reference dataset for Japanese explosive volcanism, with a view to define the diagnostic geochemical signatures capable of aiding tephra correlations across the Asian-Pacific region and beyond. All tephra deposits analysed were erupted during the last 150 ka (**Table 1**), consistent with the estimated basal age of the Lake Suigetsu (SG06) sediment record based on low-resolution pollen analysis. Owing to the prevailing westerlies a greater emphasis was placed on volcanism south-west of Lake Suigetsu. However a smaller number of large magnitude, widespread eruptive units from stratovolcanoes and calderas in central-northern Honshu and Hokkaido are also characterised.

In the Kyushu SVR two medial ash (fall) deposits of the Kikai Tozurahara (K-Tz) were collected from Tanegashima and Yakushima Islands. Ash deposits of the Holocene caldera forming Kikai Akahoya (K-Ah) eruption were collected from along the Takatoge pass, 90 km north of Kikai caldera and from north-east of Aso caldera, at Doimakino. The Ata Ignimbrite was collected at two localities, one east of the caldera and south of Sakurajima volcano, whilst another at Fumuto along the coast. Co-ignimbrite ash fall attributed to the same eruption was also sampled from beneath the Aso-ABCD eruption sequence and above Aso-3 collected near Noga (Machida, 1996, Ono et al., 1977). The Ikeda pumice associated with caldera forming event in the west of Ata caldera was collected east of Fumuto. Further north at Aira caldera, the Aira-Iwato Ignimbrite (A-Iw) was sampled just north of Kirishima volcano, whilst Aira Tanzawa (AT) fall and flow deposits were sampled at Fumuto. Glass data is also presented for the Late-glacial eruption of Sakurajima, Sz-S from along the Takatoge Pass, this the largest magnitude event of this presently active cone located in Aira caldera.

In the Kyushu CVR at Aso caldera the following prominent tephra fall and flow units (oldest to youngest spanning ~45-135 ka) were sampled (**Table 1**), they include ignimbrite deposits associated with the last two caldera forming eruptions and a series of sub-Plinian to Plinian fall out deposits. Samples characterised include Aso-3W (fall), Aso-3A (flow), Aso-3 (main-flow), Aso-N (fall), Aso-M (Fall) Aso-D, Aso-C, Aso-B, Aso-A (fall), Aso-Y (fall), Aso-4 (flow), Aso central cone pumice (ACP) 6 to 3 (fall). The ACP samples follow the nomenclature and stratigraphy of Miyabuchi (2009), whilst the remaining samples were collected from east of

the caldera near Noga (Ono et al., 1977; Machida, 1996; **Fig. 1**). Also analysed is a distal ash candidate of the Aso-4 eruption sample over 1500 km north-east of source at Lake Mokoto, Abashiri, Northern Hokkaido. Further north-east, in the Hohi Volcanic Zone, at Kuju volcano, the Kuju-D (fall), Kuju-Handa (Ignimbrite) and Kj-P1 (Fall) deposits were all sampled (**Table 1**).

In central Honshu, at the northern extend of the Izu-Bonin arc, Hakone caldera, Hk-TAu8 pumice fall deposits (Machida, 2008) were sampled to represent glass compositions of this volcanic region. Volcanic glass data is provided from large magnitude Late Quaternary eruptions along the NEJA (including the Norikura Volcanic Zone); these include the Ontake Daiichi (On-Pm1) at Uenohara, Yamanashi Prefecture, whilst further north the Towada-Hachinohe (To-H). On Hokkaido glass data is presented for the caldera forming eruptions Shikotsu-1 (Spfa) and Toya. Kurile Arc tephra deposits from Kutcharo caldera forming eruptions, Shoro (Kc-Sr/1) and Hb eruptive units are analysed, along with the intervening Plinian Kc-2/3 activities **(Table 1)**. Younger Holocene activities of Mashu caldera (Mashu-f), situated in the eastern sector of Kutcharo are also characterised here. Full details of all sample geochemically investigated and sample localities can be found in **Table 1 and Supplementary Material 1**.

2.2 Lake Suigetsu (SG06 core) distal tephra layers

In this contribution we present and discuss new trace element volcanic glasses data for eleven visible SG06 tephra layers SG06-0967, SG06-2650, SG06-3485, SG06-3912, SG06-4963, SG06-5181, SG06-5287, SG06-5353, SG06-6344, SG06-6413 and SG06-6634, many of which are considered equivalent to large magnitude (>M6) eruptions and form widespread Japanese tephrostratigraphic markers (**Table 2**). Here these data are integrated with the trace element glass data of SWJA (Daisen and Sambe) derived SG06 layers (Albert et al., in press).

2.3 Electron microprobe (EMP)

Major and minor element volcanic glass chemistry of individual juvenile clasts was determined using a wavelength-dispersive JEOL 8600 electron microprobe in the Research Laboratory for Archaeology and the History of Art, University of Oxford. A beam accelerating voltage of 15kV was used with a 6nA current and a beam diameter of 10 μm. The instrument was calibrated with a suite of appropriate mineral standards; peak count times were 30 s for all elements except Mn (40s), Na (12s), Cl (50s), P (60s). Reference glasses from the Max Plank institute (MPI-DING suite; Jochum et al., 2006) bracketing the possible chemistries were also analysed alongside the unknown tephras. These included felsic [ATHO-G

(rhyolite)], through intermediate [StHs6/80-G (andesite)] to mafic [GOR128-G (komatiite)] glasses. All glass data has been normalised to 100 % for comparative purposes. This is of paramount importance for tephras in marine and lacustrine cores, as glass shards may absorb water from their surroundings, which often results in low totals. Analytical totals < 93% were discarded. Errors are typically < ± 0.7% RSD for Si; ~ ± 3% for most other major elements, except for the low abundance elements: Ti (~ ± 7%), Mn (~ ± 30%). Error bars on plots represent reproducibility, calculated as a 2 x standard deviation of replicate analysis of MPI-DING StHs6/80-G. Glass standard data are reported in **Supplementary Material 2**.

2.4 Laser Ablation Inductively Coupled Plasma Mass Spectrometry (LA-ICP-MS)

The analyses were performed using a Thermo Scientific iCAP Qc ICP-MS coupled to a Teledyne Photon Machines Analyte G2 193 nm eximer laser ablation system with a HelEx II two-volume ablation cell at the Department of Geology, Trinity College, Dublin. Spot sizes of 30, 25 and 20 μm were used owing to varying size of the ash particles and glassy areas available for analysis. The repetition rate was 5 Hz and the count time was 40 s on the sample and 40 s on the gas blank (background). The ablated sample was transported in He gas flow (0.65 L min^{-1}) with additional N_2 (5 ml min^{-1}) via an in house signal smoothing device (PoshDOGII). Concentrations were calibrated using NIST612 with ^{29}Si as the internal standard and using a Ca correction factor as advocated in Tomlinson et al. (2010). Data reduction was performed using Iolite 2.5 and portions of the signal compromised by the ablation of microcrysts and resin-filled voids were excluded. A small subset of samples were analysed using an Agilent 8900 triple quadrupole ICP-MS (ICP-QQQ) coupled to a Resonetics 193nm ArF excimer laser-ablation in the Department of Earth Sciences, Royal Holloway, University of London, using the analytical procedures and data reduction (Microsoft Excel) methods outlined in Tomlinson et al. (2010). Accuracies of ATHO-G and StHs6/80-G MPI-DING glass analyses across the entire data set are typically ≤5% for Rb, Sr, Y, Zr, Nb, Ba, La, Ce, Pr, Nd, Sm, Eu, Gd, Dy, Er, Yb, Hf, Ta, Th, U. Analyses of MPI-DING secondary standards run alongside tephra samples are provided in the **Supplementary Material 2,** along with the full volcanic glass data sets.

2.5 ^{40}Ar/^{39}Ar dating

A detailed sample preparation routine is discussed in Mark et al. (2010) but briefly: single crystals of hornblende were separated from 1 kg of sample after disaggregating, washing and sieving followed by magnetic and density separations and finally ultrasonic cleaning in nitric acid for 5 minutes. Hornblendes were handpicked under binocular microscope for analysis. Samples were irradiated in the CLICIT facility of the Oregon State University

TRIGA reactor using the Alder Creek sanidine (Nomade et al., 2005) as a neutron fluence monitor.

^{40}Ar/^{39}Ar analyses were conducted at the NERC Argon Isotope Facility, Scottish Universities Environmental Research Centre (SUERC) and the Berkeley Geochronology Center (BGC). Samples analyzed at BGC were run and reported blindly, without knowledge of the SUERC results (and vice versa). Details of irradiation durations, J measurements, discrimination corrections are provided in **Supplementary Material 3**. Irradiation correction parameters are also listed in the same file.

For J determinations three bracketing standard positions surrounding the unknown were used to monitor the neutron fluence. Ten measurements were made for each bracketing standard position. The weighted average ^{40}Ar*/^{39}ArK was calculated for each well, and the arithmetic mean and standard deviation of these three values was used to characterize the neutron fluence for the unknown. This approach was deemed sufficient, as due to the relatively short irradiation durations there was no significant variation between the three positions in a single level of the irradiation holder. This also facilitated high-precision measurement of the J-parameter. Note that for all J-measurements no data were rejected.

Backgrounds and mass discrimination measurements (via automated analysis of multiple air pipettes) specific to each batch are summarized in **Supplementary Material 3**. Air pipettes were run after every 2 analyses. Backgrounds were run after every analysis and subtracted from ion beam measurements (arithmetic averages and standard deviations). Mass discrimination was computed based on a power law relationship (Renne et al., 2009) using the isotopic composition of atmospheric Ar reported (Lee et al., 2006) that has been independently confirmed (Mark et al., 2011). Corrections for radioactive decay of ^{39}Ar and ^{37}Ar were made using the decay constants reported by Stoener et al. (1965) and Renne & Norman (2001), respectively. Ingrowth of ^{36}Ar from decay of ^{36}Cl was corrected using the ^{36}Cl/^{38}Cl production ratio and methods of Renne et al. (2008) and was determined to be negligible.

Samples were analyzed by total fusion with a CO_2 laser and measurements made using a MAP 215-50 (MAP2) noble gas mass spectrometer. The mass spectrometer is equipped with a Nier-type ion source and analogue electron multiplier detector. Mass spectrometry utilized peak-hopping by magnetic field switching on a single detector in 10 cycles (further details in Mark et al., 2017).

Ages were computed from the blank-, discrimination- and decay-corrected Ar isotope data after correction for interfering isotopes based on the following production ratios, determined

from fluorite and Fe-doped $KAlSiO_4$ glass. Ages and their uncertainties are based on the methods of Renne et al. (2010) and the calibration of Renne et al. (2011) for decay constant, and the Alder Creek sanidine age of Niespolo et al. (2017) 1.1891 ± 0.0008 Ma.

Where not otherwise distinguished, $^{40}Ar/^{39}Ar$ age uncertainties are stated as X ± Y/Z, where Y is the analytical uncertainty as defined above, and Z is the full external precision considering both analytical and systematic sources of uncertainty (e.g., decay constant). Age computation used the weighted (by inverse variance) mean of $^{40}Ar*/^{39}ArK$ values for the sample and standard. Outliers were tested for in both single-crystal samples and standards using a 3-sigma filter applied iteratively until all samples counted are within 3 standard deviations of the weighted mean ± one standard error. There are no outliers in the dataset. The data are reported at the 1-sigm confidence interval. All raw data and plots are reported in **Supplementary Material 2**.

2.6 The chronology of the SG06 sedimentary record

The SG06 sedimentary record is underpinned by the chronology presented in Bronk Ramsey et al. (2012), which provides an integral component of the International ^{14}C Calibration (IntCal) dataset (Reimer et al., 2013). The independent chronology of the Lake Suigetsu SG06 sedimentary sequence has subsequently been modelled on to the IntCal13 timescale implementing three successive cross-referenced Poisson-process (*'P_Sequence'*) depositional models using OxCal (ver. 4.3; Bronk Ramsey 2008; 2017). These include 775 AMS ^{14}C dates obtained from terrestrial plant macrofossils from the upper 38 m (SG06-CD) of the SG93 and SG06 sediment cores (Kitagawa and van der Plicht, 1998a, 1998b, 2000; Staff et al., 2011, 2013a, 2013b) and varve counting between 12.88 and 31.67m SG06 CD (Marshall et al. 2012; Schlolaut et al. 2012). Beyond the annually laminated and ^{14}C dated portion of the sequence the age-depth model of SG06 is based on a linear extrapolation which is anchored by deeper chronological tie points, which now includes the $^{40}Ar/^{39}Ar$ age of the Aso-4 eruption presented here.

3. Volcanic glass chemistry

3.1 Geochemical variations at Japanese arc volcanoes

In this section we outline the geochemical variation observed in the matrix glasses erupted during predominantly M5 or greater events at productive calderas and stratovolcanoes extending the length of the Japanese Islands, with an emphasis on the identification of diagnostic features useful in determining the source regions of distal tephra layers. Average major and trace element glass data of proximal-medial eruptive units analysed here are

presented in **Table 3**, and the full geochemical datasets are provided in **Supplementary Material 2**.

Vitreous tephra erupted at centres extending across the islands of Japan show Low-K (Tholeiitic) through to High-K Calc-alkaline (HKCA)/Shoshonitic affinities (**Fig. 2A**). The K_2O content offers a first order major element discriminator of Japanese eruptive source regions (**Fig. 3A**). The highest K_2O content observed in Japanese glasses analysed here are associated with the volcanism in the Kyushu CVR (**Fig. 1**), specifically the HKCA rhyolitic products of Aso Caldera, and the Kuju volcanic complex (HVZ; **Fig. 2A Fig. 3**). The HKCA eruptive products of Aso caldera are some of the most compositionally distinctive in Japan, with K_2O > 3 wt.% at ~ 66 wt.% SiO_2, and the most evolved glasses analysed extending to 6 wt.% in K_2O (Aso-N; **Fig. 2**). Consequently the Aso caldera glasses reside on very distinct evolutionary trends using either CaO content plotted against SiO_2 making attribution of tephra to volcanic source straightforward (**Fig. 2A**). The HKCA eruptive products of Kuju volcano extend to higher K_2O contents than glasses erupted further south in the Kyushu SVR. However, there is some compositional overlap with the most K_2O-rich glasses erupted at Aira (A-Iw), thus making major element distinctions between Aira and Kuju tephra challenging (**Fig. 2**).

The volcanic glasses of explosive products erupted at forearc calderas in the Kyushu SVR (Kikai, Ata, Aira; **Fig. 1**) reside on a transitional CA to HKCA trend, and show large degrees of major element compositional overlap (**Fig. 2**). Further north-east the tephra deposits erupted along the SWJA beneath Honshu, at Daisen and Sambe stratovolcanoes, show dacite to rhyolite glasses that extend from CA through to HKCA compositions (Albert et al., in press) and partially overlap at a major element level with those erupted at volcanic centres in the Kyushu SVR, the CVR (Kuju) and the Norikura volcanic chain (Ontake) (**Fig. 2**).

The dacite-rhyolitic eruptive products of calderas situated in forearc positions along the NEJA show lower K_2O content than those at calderas on Kyushu (**Fig. 2**). Shikotsu (Spfa-1; 2.5-2.7 wt.% K_2O) and Toya (Toya; 2.5-3.0 wt.% K_2O) calderas along the NEJA (SW Hokkaido) erupted glasses with CA affinities that are lower in K_2O content than those erupted in the Kyushu SVR. The NEJA centres of Shikotsu and Toya centres (SW Hokkaido) also erupt glasses with higher K_2O content than those CA glasses erupted at the southern tip of the Kurile Island Arc at Kutcharo caldera (1.7-2.3 wt.% K_2O). Those calderas located closest to the trench in the forearc produced distinctive arc tholeiitic (Low-K) glass compositions (**Fig. 2**). Late Quaternary-Holocene silicic tholeiitic (Low-K) large magnitude eruptions are recognised at Hakone (Izu-Bonin arc), Towada (NEJA) and Mashu (Kurile arc) calderas. Mashu has erupted low-K rhyolitic glasses (0.61-0.82 wt.% K_2O) which are

distinctive, whilst K_2O content in the Hakone (1.03-1.56 wt.% K_2O) and Towada (1.03-1.27 wt.% K_2O) dacite to rhyolite glasses is slightly more elevated (**Fig. 2**).

Discriminating the volcanic glasses of the forearc calderas in the Kyushu SVR from those in the rear-arc along the SWJA (Daisen and Sambe) and in the Norikura volcanic zone (Ontake) can be partially achieved using SiO_2 vs. FeOt content of the glasses (**Fig. 2C**). Kyushu SVR forearc caldera glasses reside on a trend of higher FeOt content at overlapping SiO_2 content. Glasses erupted from the Kuju volcanic complex (Kyushu CVR), appear to be more akin to those erupted from the SWJA volcanoes (Daisen and Sambe), however there is a degree of convergence at this high SiO_2 content with glass compositions erupted along the Kyushu SVR (**Fig. 2C**). A SiO_2 vs CaO Harker diagram provides a useful means to distinguish the Daisen and Sambe SWJA products (Albert et al., in press), however again the Kuju glasses reside a point of convergence between the two suites (**Fig. 2B**). The Kuju glasses do typically extend to higher SiO_2 content than the eruptive products erupted from Daisen. Whilst compared to Sambe rhyolitic glasses with similar K_2O content, the Kuju glasses extend to higher SiO_2 content **(Fig. 2A).**

SiO_2 vs CaO is also useful for separating the eruptive products of the Kyushu SVR calderas (Aira, Ata, Kikai) from those volcanoes along the NEJA (Towada, Shikotsu) and southern Kurile Island Arc (Kutcharo, Mashu), where the glasses of the former reside on a trend of lower CaO at a given SiO_2 content (**Fig. 2B**). The main exception to this being the rhyolitic Toya deposits which are characterised by glasses with exceptionally low CaO content (0.33-0.43 wt.%; **Fig. 2B**). Whilst a SiO_2 vs FeO harker diagram largely separates the eruptive products of Daisen from those of Kyushu SVR and NEJA calderas, overlap still exist with the products of Ontake volcano (Norikura volcanic zone) (**Fig. 2C**).

Consistent with their subduction genesis, all glasses erupted at volcanic sources extending the Japanese Islands display enrichment in fluid mobile Large Ion Lithophile elements (LILE e.g., Rb, Ba, K) relative to insoluble high field strength elements (HFSE), specifically Nb and Ta and the Rare Earth Elements (REE; La to Yb) (**Fig. 4**). Many of the Kyushu SVZ and NEJA calderas have erupted silicic tephra with overlapping levels of incompatible trace element enrichment and subsequently similar mantle normalised profiles (**Fig. 4**). Fluid mobile elements are highly variable between felsic deposits of the different Japanese volcanic sources, and as such are coupled to the K_2O content of the volcanic glasses. Rubidium is a particularly useful discriminator of Japanese volcanic sources (**Fig. 3-4**). Low-K (Tholeiitic) glasses erupted at forearc calderas, Towada (NEJA), Hakone (Izu-Bonin) and Mashu (Kurile arc), show the lowest levels of Rb enrichment (**Fig. 3-5**). With increased K_2O content at CA sources of the Southern Kurile Arc (Kutcharo) and the NEJA (Toya/Shikotsu)

Rb content also increases. The higher K_2O content of the silicic magmas erupted at centres in both the SVR (Kikai, Ata, Ikeda, Aira) and CVR of Kyushu, see the greatest highest levels of enrichment of Rb (**Fig. 3-4**). Similarly, Th content also displays a similar relationship to K_2O, meaning Th content is variable at the different source regions of Japan and offers a key means to compositionally decipher eruption deposits (**Fig. 5**) The lowest Th content glasses are observed in the Low-K tholeiitic dacite to rhyolite glasses of Mashu, Hakone and Towada (**Fig. 3-5**). Silicic tephra deposits erupted from forearc calderas on Hokkaido (NEJA/Southern Kurile Arc) show lower Th contents than those glasses erupted in both the Kyushu SVR and the CVR (**Fig. 3-5**). Enrichment of the LREE is typical in the genesis of fluid rich magmas, as such variations in the contents of La and Ce again broadly follow K_2O content (**Fig. 4**). Tholeiitic (Low-K) sources show restricted LREE enrichment relative to the HREE, for instance at Mashu (Kurile Arc) and Hakone (Izu-Bonin Arc) calderas this in manifested as a flat REE profile and low La/Yb ratios (**Fig. 4; Table 3**). Of the Japanese sources investigated the HKCA glasses erupted at Aso, Kuju, Aira, and Ontake, are some of the most enriched in fluid mobile trace elements (**Fig. 3-4**). The rhyolitic glasses of Kutcharo/Mashu (Kurile Arc) and Hakone (Izu-Bonin Arc) display particularly low Nb and Ta contents relative to the silicic glasses erupted on Kyushu island (SVR and CVR), the NEJA and the SWJA (**Fig. 4**).

The glasses erupted along the SWJA show strong depletions in the Middle and Heavy REE (**Fig. 4**), including low-Y contents **(Fig. 5A)**, a feature that was previously recognised in the glasses erupted at Daisen and Sambe volcanoes (Kimura et al., 2015; Albert et al., in press). New trace element glass data presented here confirms this feature is also observed in the Kuju volcanic products of the HVZ, which some consider the southern extent of the SWJA (Shibata et al., 2014; **Fig. 4**). This middle and heavy REE depletion provides a useful diagnostic feature of these volcanoes. This feature, coupled with overall arc variations in Th and REE content of Japanese volcanic glasses, make a Y vs. Th bi-plot particularly robust tool for compositionally spreading the volcanic sources of Japan (**Fig. 5A-B**).

3.1.1 Kyushu SVR geochemical variations

In this section of we explore the geochemical variations between the eruptive products of large magnitude eruptions of the calderas of the Kyushu SVR (Kikai, Ata, Aira) for the purpose of tephra correlations. These sources have tapped both low (~ 74 wt.%) and high (> 77 wt.%) SiO_2 transitional CA to HKCA rhyolitic magmas with largely overlapping major element glass chemistries (**Fig. 2**), making specific source attribution of tephra deposits from this region more challenging. Overall, moving north to south between calderas in the SVR, there appears a trend of decreasing K_2O content (**Fig. 3**) of the rhyolitic glasses erupted

despite overlapping SiO_2 content, with the lowest K_2O rhyolites erupted at Kikai caldera and the highest at Aira (**Fig. 3**). The high-SiO_2 rhyolites erupted at Kikai caldera (K-Tz) can be distinguished from those erupted at Aira caldera based on lower Al_2O_3 content at overlapping SiO_2 (**Fig. 2D**). Distinguishing Kikai (K-Ah) and Ata low-SiO_2 rhyolites relies on the Ata glasses extending to subtly lower CaO and FeOt contents than those of Kikai caldera (**Fig. 2C**).

Trace element concentrations offer useful means to distinguish the eruptive products of the Kyushu SVR calderas. Irrespective of relating to high- or low-SiO_2 rhyolites, the Kikai caldera volcanic glasses have lower Nb and Ta contents than the volcanic glasses with similar SiO_2 contents erupted at either Ata or Aira calderas (**Fig. 3-4**). Aira (AT, A-Iw) and Ata (Ikeda) high-SiO_2 rhyolitic glasses share very similar mantle normalised trace element profiles **(Fig. 4)**. Indeed, they share significantly steeper REE profiles than those of Kikai caldera (**Fig. 4**), reflected in more elevated La/Yb ratios **(Table 3)**. High-SiO_2 rhyolites erupted at Aira are most easily distinguished from those of Ata based on their higher concentrations of Rb, Th and U content (**Fig. 3-4**). Zirconium content appears to vary between eruptive units at the respective Kyushu SVR calderas. The high-SiO_2 rhyolites of Kikai and Ata show significantly lower Zr content relative to the lower-SiO_2 rhyolites erupted at the same source (**Fig. 5B**).

3.1.2 Kyushu CVR Compositional variations

In this section we explore the compositional variation in the deposits sampled from the CVR and the challenges of distinguishing the products of successive eruptions from the same volcanic centre. Here we have concentrated on two volcanic centres in the Kyushu CVR which are responsible for a series of large magnitude eruptions during the Late Quaternary, Kuju volcano and Aso caldera. As highlighted above the HKCA eruptive products of Aso caldera plot on a distinctive evolutionary trend, consequently they are easily distinguished from those erupted further north-east in the HVZ at Kuju volcano (**Fig. 2**).

Focusing specifically on eruption units at Kuju volcano, and the activity at ~53-55 ka (**Table 2**), moving up through the complex eruptive succession of Kj-D (fall), Kj-Hd (Hanada Ignimbrite) and Kj-P1, all tephra units show volcanic glasses with overlapping major element glass chemistries (**Fig. 2**). The precise temporal relationship between these chemically overlapping eruptive units is unclear, only the Kj-Hd ignimbrite deposit is dated (**Table 1**), yet somewhat peculiarly the overlying Kj-P1 (Plinian fall) deposit is considered time-equivalent, rather than the underlying Plinian deposit Kj-D (Okuno et al., 2017; Tsuji et al., 2017). A subtle feature of possible distinction is that the glasses of the uppermost fall deposit (Kj-P1) extend to higher SiO_2 and lower FeOt compared to the units stratigraphically below **(Fig. 2C)**. Distinguishing the three units on the basis of trace element glass chemistry has not

been achieved here owing to the absence of sufficiently large enough and crystal free matrix glass for LA-ICP-MS analysis. Kuju-D was not successfully analysed at a trace element level, whilst only a single analysis was obtained for the Kj-P1 and Kj-Hd deposits. Importantly these analyses, combined with that of the older Kj-Mg tephra, all verify that Kuju HKCA rhyolites display a SWJA-type chemistry with depletions in the Middle and Heavy REE (**Fig. 4**), reflected by their high La/Yb ratios (**Table 3**).

Deposits explosively erupted at Aso caldera between 50-135 ka range from trachy-dacite through to rhyolitic (63.4-75.0 wt.% SiO_2; 3.3-6.5 wt.% K_2O; **Fig. 2**). The most heterogeneous eruptions deposits investigated at Aso are associated with the caldera forming eruptions, Aso-3 and Aso-4 (**Fig. 6**). The Aso-3 glasses reside on a trend of higher K_2O at a given SiO_2 content relative to the younger eruptive products Aso-4 and straddle the HKCA/Shoshonitic classification boundary (**Fig. 2A**). There is significant compositional overlap between temporally distinct eruptive units of the volcano, with very few deposits showing unique major element glass compositions (**Fig. 2; Fig. 6**). The most distinctive glasses being those with the most elevated SiO_2 and K_2O content. These include the silicic end-member of the Aso-3 caldera forming eruption deposits, and fall out from Plinian eruptions Aso-N, Aso-Y and ACP3 (**Fig. 6**). Successive eruptive units from Aso caldera show trace element glass compositions that overlap with one another (**Fig. 6D**).

The basal fall (Aso-3W) and the lower most ignimbrite unit (Aso-3A) are largely dominated by the most silicic rhyolitic glass compositions produced during the caldera forming eruption (~70 wt.% SiO_2; ~5 wt.% K_2O). Less evolved glasses (63-66 wt.% SiO_2) were found in the upper and more voluminous portion of the ignimbrite (**Fig. 6**), which is broadly consistent with the findings of Kaneko et al., (2015), who also report the appearance of the least evolved magmas in the later phase of the eruption. However our data do not extend to the most primitive compositions (53-62 wt.% SiO_2) reported by Kaneko et al. (2015), indicating that perhaps our Aso-3 sampling is not completely representative. Significant variation is observed in the levels of incompatible trace element enrichment of the Aso-3 glasses (235-335 ppm Zr; 12.5-18.1 ppm Th). Strontium clearly behaves compatibly and therefore the least evolved glasses are recognised by more elevated Sr content (~500 ppm), whilst the most silicic rhyolitic glasses display lower Sr content (~240 ppm).

Plinian fall units between the Aso-3 and Aso-4 caldera forming eruptions at Noga Cave can be broadly distinguished on chemo-stratigraphic grounds using their position relative to the Ata tephra marker (99.3 ± 6.0 ka; Section 3.2.3) in the sequence. The four Plinian fall units (Aso-N to Aso-I) that occur beneath the Ata tephra all reside on the trend of higher K_2O content consistent with the older Aso-3 deposits, and including some geochemical overlap

with the Aso-3 upper Ignimbrite deposits. Excluding the distinctive high-K_2O (6.3 wt.%) Aso-N Shoshonitic glasses (**Fig. 2A**), the remaining three units (Aso-M, Aso-K, Aso-I) all have overlapping major element chemistries (**Fig. 6**), yet these tephra deposits compositionally differ from the four Plinian fall deposits stratigraphically above the Ata tephra, Aso-ABCD (**Fig. 6**). Aso-ABCD glasses show broadly overlapping chemistries, but can be distinguish from the older Aso-M to Aso-I deposits owing to their higher SiO_2, and lower CaO and FeOt (**Fig. 6C**). Aso-D is seemingly distinguishable from Aso-ABC on the basis that the glasses extend to subtly higher CaO content (**Fig., 6C**).

Eruption deposits Aso-M, Aso-K and Aso-I glasses are difficult to distinguish at a trace element level, one feature is that of note is that the Aso-M glasses contain subtly more elevated Sr, relative to Aso-K and Aso-I (**Fig. 6F**). Aso-K and Aso-I volcanic glasses are indistinguishable at a major and trace element level. Aso-ABCD glasses show considerable variation in their incompatible trace element contents, importantly Aso-B and Aso-C are restricted to lower levels of enrichment compared to those Aso-A and Aso-D (**Fig. 6**). Whilst Aso-B and Aso-C are indistinguishable from one another they also show lower Sr content than the glasses of Aso-A and Aso-D (**Fig. 6D**). The Aso-A and Aso-D fall deposits have glasses with overlapping trace element concentrations, yet Aso-D glasses extending to higher levels of enrichment (e.g., Th; Zr; **Fig. 6C-D**).

The Aso-4 ignimbrite deposits are distinctive owing to their compositional heterogeneity (**Fig. 6**), proximal glasses from Noga Cave reveal three distinct glass populations, with two rhyolitic populations dominating and being most easily distinguished using the CaO content (**Fig. 6C**). Component 1 glasses show the lowest CaO content (1.0-1.2 wt.%) are associated with higher SiO_2 (71.8-72.6 wt.%) content. Component 2 rhyolites show higher-CaO (1.4-1.6 wt.%) and are associated with the lower SiO_2 content glasses (70.4-71.9 wt.%). A third component, observed in the Aso-4 ignimbrite deposit, is derived from dark scoriaeous deposits, and have a less evolved trachy-dacite composition (ca. 65-66 wt.% SiO_2). These primitive compositions are lower in K_2O content than Aso-3 glasses with comparative SiO_2 content (**Fig. 2A; Fig. 6**). The two rhyolitic components of the Aso-4 (1 and 2) tephra are most easily distinguished at a trace element level using their Sr content. Component 1 glasses display lower Sr (131-184 ppm) at overlapping Th content relative to the component 2 (146-619 ppm Sr) rhyolites (**Fig. 6F**). The component 1 low-Sr rhyolitic glasses were restricted to the lowermost Aso-4 ignimbrite deposits (ITJ40**; Table 1**). Aso-4 glasses display a wide range in incompatible trace element contents (e.g., 165-311 ppm Zr; 9.1-17.7 ppm Th) consistent with their significant major element variation. The Aso-4 range in incompatible trace element concentrations encapsulates that of the combined Aso-ABCD succession. Aso-4 high Th content component 1 glasses display lower Sr content than the Aso-D and

Aso-A glasses at equivalent Th (**Fig. 6F**). Furthermore these same Aso-4 glasses show lower Y content than the Aso-A and Aso-D deposits (**Fig. 6E**).

Volcanic glasses of the successive ACP (6-3) Plinian fall deposits show trace element concentrations that overlap with those of the older Aso activities (**Fig. 6**). The most silicic ACP deposits, ACP3, are further distinguishable from the ACP6-4 as they show the lowest Sr contents (**Fig. 6F**). Consistent with major element compositional overlap, ACP4 and ACP5/6 glasses show trace element concentrations that broadly overlap with Aso-4 component 1 and 2 glasses (**Fig. 6**). Yttrium in the ACP4 glasses appear to be offset to higher concentrations relative to the older Aso-4 deposits at overlapping Th content, more consistent with the Aso-ABCD glasses (**Fig. 6E**), further reinforcing the importance of subtle variations in the REE contents of the Aso glasses and in particular Y content.

3.2 SG06 Tephra correlations, stratigraphic and geochronological constraints

In the following section we utilise the new proximal-medial major and trace element volcanic glass dataset to explore the provenance of the distal Lake Suigetsu (SG06) tephra layers,. Geochemical correlations are explored in figures **5-10**, whilst the fully integrated SG06 tephrostratigraphy developed and discussed below is presented in **Figure 11**. **Table 4** contains the new trace element volcanic glass data for the SG06 layers, along with their major element compositions. These tephra layers and correlations to source are grouped based on similar volcanic source regions and in accordance with key diagnostic features outlined above. All specific tephra correlations outlined below are summarised in **Table 2**.

3.2.1 *SWJA (Daisen and Sambe)*

Thirteen layers of the twenty-four visible SG06 tephra layers characterised at a trace element level showed signatures consistent with those erupted along the SWJA. These layers were deemed most likely to derive from Daisen and Sambe owing to their volcanic glasses showing distinctively low-Y (**Fig. 5A**) and middle/heavy REE contents, a characteristic of SWJA volcanism, a feature often referred to as adakitic (Kimura et al., 2015). Subsequent, major element comparisons of the visible SG06 layers to chrono-stratigraphically relevant proximal units at the two volcanoes facilitated the construction of an integrated proximal-distal eruption event stratigraphy for the SWJA (Albert et al., in press). Major element similarities between two further visible SG06 tephra layers and known eruption deposits from the two volcanoes, resulted in a total of nine layers being correlated to eruptions at Daisen and five to Sambe volcano (Albert et al., in press). The precise correlations between the SG06 visible tephra layers and Daisen and Sambe eruptions units are listed in **Table 2,** along with SG06 age estimates**.** The SG06 eruption stratigraphy for

Daisen volcano highlights periods of intense, closely spaced large magnitude eruptions. Furthermore, the chronology of the SG06 record, particularly during the varved-radiocarbon timeframe, provides unrivalled constraints on ages of eruptions at the two volcanoes. Arguably the most significant Daisen eruptive unit discovered in the SG06 record relates to the Daisen Kurayoshi Pumice (DKP) - SG06-4281 (59.6 ± 5.5 ka [2σ]). Machida and Arai (2003) recognise this tephra as one of the key Japanese tephrostratigraphic markers. This tephra is traced over 600 km NE of the volcano, and provides a useful marker for constraining Late Quaternary sedimentary sequences in Japan (Albert et al., in press). Importantly the SG06 tephrostratigraphic record demonstrated that this eruption deposit is temporally distinct from the widespread Sea of Japan SAN1 marine tephra (= SG06-4141) preventing erroneous synchronisation of terrestrial and marine archives around the MIS3/4 transition (e.g., Ikehara et al., 2004).

Albert et al. (in press) recognised that tephra SG06-4141 showed a trace element signature consistent with the eruptive products of the SWJA. However, this layer correlated to the widespread Sea of Japan SAN1 marine marker layer, had a major element composition that subtly differed from those of Daisen and Sambe (higher-SiO_2 rhyolites). Whilst the trace element glass data of SG06-4141 was most consistent with the Daisen eruptive products, no obvious proximal candidate was recognised in the volcanic stratigraphy of either Daisen or Sambe volcanoes. Consequently, this layer is discussed further in the context of explosive volcanism in the Kyushu CVR (**Section 3.2.2.1**).

3.2.2 Kyushu Central Volcanic Region (CVR)

3.2.2.1 Kuju volcano

As outlined above tephra SG06-4141, dated at 54.4 ± 1.6 ka [2σ], displays a SWJA type geochemical signature; yet no prominent chrono-stratigraphically relevant eruption units is recognised at either Daisen or Sambe volcanoes. Instead the possibility is explored that this tephra deposit derived from an alternative source region, one that has produced magmas with a similar low-Y/HREE affinity. Albert et al. (in press) recognised that SG06-4141/SAN1 had a major element composition consistent with the eruptive products of Kuju volcano (Kj-Hd) in the HVZ of central Kyushu (**Fig. 7**). Crucially the Kj-Hd Ignimbrite, and the associated Kuju-P1 Plinian fall are dated at ~53.5 ka (Okuno et al., 2017) which is broadly consistent with the age of the SG06-4141/SAN1. Trace element glass analyses presented here for Kuju eruptive units (Kuju-P1 and Miyagi), verify that the volcano has also erupted magmas displaying low-Y and middle and heavy REE contents, consistent with those erupted at Daisen and Sambe (**Fig. 3; Fig. 5**). Therefore the new trace element glass data presented here support the previous assignment of SG06-4141/SAN1 to explosive activity at Kuju

volcano (**Fig. 8D**). Linking SG06-4141 to a specific eruptive unit at Kuju is more challenging, major element glass data from the Kj-P1 (Fall), the Kj-Hd (Ignimbrite) and Kj-D (Fall) are all largely indistinguishable from one another (**Fig. 2**) and trace element glass data presented here is not sufficient enough to discriminate the individual units.

Glass chemistry aside, the Kj-P1 fall has a strong eastward dispersal towards Shikoku Island (Tsuji et al., 2017), inconsistent with the SAN1 layers distribution further north-east in the Sea of Japan. Instead we tentatively suggest that the distal tephra may relate to a co-ignimbrite ash plume dispersed from the voluminous Kj-Hd Ignimbrite, indeed widespread ash dispersals can often the product of co-ignimbrite plumes (e.g., Smith et al., 2016). Irrespective of specific source attribution, the robust correlation of the widespread Sea of Japan SAN1 marine layer (Ikehara et al., 2004) to SG06-4141 (Albert et al., in press) places important age constraints on this event layer capable of synchronising marine and terrestrial palaeoclimate archives in the region.

3.2.2.2 Aso Caldera

Comparisons with new proximal glass datasets from Aso caldera confirm that three visible SG06 layers (SG06-3912; SG06-4963; SG06-5287) unequivocally show HKCA major and trace element signatures consistent with the volcano (**Fig. 6-7**).

Previously, Smith et al., (2013) assigned both the geochemically indistinguishable SG06-4963 and SG06-4979 tephra layers to the Aso-4 caldera forming eruption based on their major element chemistry. However, the thinner tephra layer SG06-4979 is only identified in a single borehole in the SG06 coring campaign, and subsequently was not been identified in the subsequently taken boreholes of the SG14 coring campaign, for this reason SG06-4979 is no longer considered a primary tephra deposit (McLean et al., in prep). Smith et al. (2013) used major element glass chemistry to relate SG06-5287 to the Aso-ABCD eruptive succession.

The SG06-3912 tephra was previously unassigned to volcanic source, however the trace element signature of these HKCA glasses, including enrichment of the LILE (Rb) and HFSE (Th, U, Zr) are all consistent with those erupted from Aso caldera (**Fig. 5; 6; 8**). Based on the SG06 age-depth model SG06-3912 has an interpolated age of 50.0 ± 0.3 ka (2σ), this broadly corresponds to a succession of pumice fall out deposits from the Aso central cone (Miyabuchi, 2011). Geochemical comparisons to these Plinian fall deposits reveal that SG06-3912 has a major and trace element composition consistent with the Aso central cone pumice (ACP) 4 fall unit (**Fig. 6G-H**). ACP4 represents one of the largest post-caldera eruptions, with a total thickness reaching 159 cm at 3.5 km outside of the caldera rim with a

volume of 0.43 km^3 (Miyabuchi, 2011). Its identification as a visible layer in the SG06 record dramatically expands the known distribution of ash fall from this eruption, and may provoke a future reassessment of the eruptive volume and magnitude estimates (M4.6; **Table 1**). It also seems likely that this eruption deposits may be traced into other sedimentary records across Japan. Importantly for the volcanic history of Aso caldera, Plinian deposits associated with ACP4-6 are all identified above the Kuju Handa/P-1 tephra in the volcanic stratigraphy. With the Kuju Handa/P-1 eruptive units correlated to SG06-4141 which is dated at 54.4 ± 1.6 ka (2σ) (Albert et al., in press), the SG06 record can place new chronological constraints on this succession of Plinian eruptions at Aso caldera, illustrating a period of intense activity spanning just 4-5 thousand years.

The major element glass chemistry of SG06-4963 is perfectly consistent with Aso-4 glass data generated on the proximal succession from Noga Cave (**Fig. 6**) and verifies the previous correlation of Smith et al. (2013). Trace element data reveals that the HKCA rhyolitic tephra display identical levels of incompatible trace element enrichment to the proximal Aso-4 ignimbrite deposits (**Fig. 8**). Importantly both diagnostic rhyolitic components (1 and 2) of the eruption sequence are identified in the SG06-4963 layer (**Table 4**), and this is illustrated by the variations in Sr content of the glasses (**Fig. 6F**). SG06-4963 shows a sub-population of volcanic glasses with significantly lower levels of incompatible trace element enrichment than are observed in the proximal sequence investigated here (e.g., 4-5 ppm Th). The glass composition of the trachy-dacite glasses (component 3) found in the proximal Aso-4 ignimbrite deposits are not observed in the distal SG06 tephra (**Fig. 6**).

The ^{40}Ar/^{39}Ar data (*n* = 25) from the proximal Aso-4 deposit sampled define a single population with an age of 86.4 ± 1.1 ka (2 σ). When plotted on an isotope correlation plot the data define an inverse isochron with an initial trapped component that is indistinguishable from atmosphere ^{40}Ar/^{36}Ar (Lee et al., 2006; Mark et al., 2011) and an ^{40}Ar/^{39}Ar age that overlaps with the weighted mean age (**Supplementary Material 3**). The data are statistically robust defining a Mean Weight Square Deviates (MWSD) of 1 and a p-value of 0.4. We interpret the ^{40}Ar/^{39}Ar weighted mean age of 86.4 ± 1.1 ka (2 σ) to represent the age of eruption for the Aso-4 event. This age is in strong agreement with the previous age estimates derived based on the stratigraphic position of the Aso-4 tephra in orbitally tuned marine isotope records. Where, Aoki (2008) dated the Aso-4 tephra at 86.8-87.3 ka, based on its stratigraphic position in the MIS5b (5.2) sediments of the northwest Pacific.

The unequivocal (major and trace element) geochemical agreement between Aso-4 and SG06-4963 mean that the ^{40}Ar/^{39}Ar age has been imported into the SG06 age-depth model and provides a new chronological anchor for this deeper portion of the record. Importantly

the age of this tephra helps to impose tighter age constraints on the linearly interpolated age estimates of tephra deposits in the deeper portion of the Suigetsu record for instance this helps constrain the age of underlying K-Tz tephra (**Section 3.2.3**).

New data presented here from a distal Aso-4 tephra layer recovered from Lake Mokoto (**Fig. 6**), northern Hokkaido, has both major and trace element concentrations consistent with the proximal Aso-4 deposits and SG06-4963, therefore confirming visible ash fall from this M7.7 eruption over 2000 km NE and is consistent with reported occurrences in the Sea of Okhotsk (Aoki, 2008; Derkachev et al., 2016). The Aso-4 ^{40}Ar/^{39}Ar age presented here offers key independent age constraint on the MIS5b (5.2) sediments of the western-Pacific region.

The HKCA rhyolitic tephra layer SG06-5287 was previously assigned to Aso-ABCD on the basis of major element glass data (Smith et al., 2013), here we review this correlation in the context of the comprehensive major and trace element data presented through the entire eruptive succession sampled at Noga Cave beneath the Aso-4 ignimbrite (**Table 1**; **Fig. 6**). SG06-5287 stratigraphic position above the Ata tephra (SG06-5353/**Section 3.2.3**) in the SG06 record immediately rules out the pre-Ata Aso-NMKI Plinian units. Consistent with its stratigraphic position above the Ata tephra, SG06-5287 instead has a major element composition broadly consistent with all four Plinian fall out units (Aso-ABCD; **Fig. 6**). However, major element data reveal that lower most fall unit Aso-D pumices are dominated by glasses with more elevated CaO content than those of SG06-5287, with the distal tephra instead consistent with the lower CaO content of Aso-ABC (**Fig. 6C**). Trace element data reveals that there is very little geochemical overlap between the SG06-5287 tephra layer and those of Aso-C and Aso-B fall units, which display restricted levels of incompatible trace element enrichment (**Fig. 6**), this means we can exclude the two thinner fall units (C and B) in the succession. SG06-5287 glasses show Y and Th contents consistent with the Aso-A glasses. Whilst they do also overlap with Aso-D, glasses these proximal deposits largely extend to higher levels of incompatible trace element enrichment, which are absent in the distal SG06-5287 deposit (**Fig. 6D-F**). Major and trace element glass data indicate that the distal tephra SG06-5287 can be most confidently assigned to the uppermost, and thickest pre-Aso-4 eruption deposit, Aso-A (**Fig. 6A-F**). The SG06 age-depth model allows us to provide an interpolated age estimate of 97.9 ± 6.0 ka (2σ) for the Aso-A eruption deposit. Importantly, in terms of the tempo of explosive activity at Aso caldera, this correlation would indicate that Aso-CBD, stratigraphically below Aso-A and above the Ata tephra (99.3 ± 6.0 ka; **Section 3.2.3**) were emplaced in a particularly short interval of time perhaps as little as ~ 1 ka, which would be consistent with the absence of any clear palaeosols between the proximal eruptive units.

Age-models for many East Asian Late Quaternary marine and terrestrial sedimentary archives are constrained by ages of Aso derived tephra layers preserved. Here we explore just some of these tephra correlations with a view to highlighting the importance of comparing proximal and distal glass chemistries when constructing tephrochronological based age-depth models.

In the Pacific ICDP borehole U1436A (-2H-1-56-58cm) a 6 cm thick tephra unit is correlated to the Aso-ABCD eruption deposits, whilst a thinner overlying layer of undefined thickness (U1436A-2H-1-25-27 cm), is attributed to the Aso-4 caldera forming eruption (Schindlbeck et al., 2018). The 6 cm thick tephra is inconsistent with the glasses erupted during the Aso-ABCD succession, but are instead entirely consistent with the two dominant rhyolitic components of the Aso-4 caldera forming eruption (**Fig. 6**). The overlying layer attributed to Aso-4 is geochemically consistent with the underlying 6 cm thick ash layer, and again the Aso-4 proximal glasses. Glass geochemistry and layer thickness indicate that the thicker layer relates to the Aso-4 caldera forming eruption, not Aso-ABCD, and that the overlying layer is probably re-worked volcanic glass from the same event. Consequently, erroneous age information has been transferred in to the age-models of this core.

In a second borehole, U1437B (-2H-6-78-80cm) Schindlebeck et al. (2018) identify a 2 cm tephra deposit attributed to the Aso-3 caldera forming eruption. Comparisons to proximal glass data sets here reveal that this tephra does not display the elevated and distinctive levels of K_2O content seen in the proximal tephra at overlapping SiO_2 content (**Fig. 6**). Whilst the distal tephra does unequivocally display a Aso-type glass chemistry, the correlation of this marine tephra to the Aso-3 events is not supported by our proximal glass data, particularly given the additional absence of less evolved glass compositions also diagnostic of this eruption. Again this points to the erroneous transfer of age information into the marine sedimentary record. Conversely, Sagawa et al. (2018) report Aso-3 tephra from the East China Sea, their marine tephra glass data is entirely consistent with our proximal deposits showing a wide range in composition from trachy-dacite to rhyolite (**Fig. 6**). This discovery highlights the significant potential of this marker layer, also reported in Lake Biwa (Nagahashi et al., 2007), to link palaeoclimate records over vast areas.

3.2.3 *Kyushu Southern Volcanic Region (SVR)*

Six layers (SG06-0967, SG06-2650, SG06-3668b, SG06-5181, SG06-5353, and SG06-6413 **Table 2**) are assigned to explosive volcanism at calderas situated in the Kyushu SVR (Aira, Ata and Kikai). All six tephra deposits show glasses with rhyolitic CA affinity, with the higher SiO_2 tephra (SG06-2650 and SG06-5181) residing at the boundary with the HKCA classification (**Fig. 7**). These tephra deposits all lie on a trend of lower CaO at a given SiO_2

content than the majority of CA deposits erupted at NEJA (excluding Toya glasses) and Kurile Arc sources (**Fig. 7**). Whilst these tephra units appear to lie on a similar major element trends (e.g., SiO_2 vs. CaO) to the eruption products of Daisen they can be easily distinguish them based on their higher FeOt content at a given SiO_2 (**Fig. 2**) and relative enrichment in the HREE compared to SWJA volcanism (**Fig. 8**).

3.2.3.1 Kikai Caldera

Two SG06 tephra layers have previously been assigned to explosive eruptions of Kikai caldera during the last 100 ka. The Holocene tephra SG06-0967 was correlated by Smith et al. (2013) to the Kikai-Akahoya (K-Ah) eruption based on major element data comparisons. Whilst SG06-5181 was correlated to the Lake Biwa tephra layer (BT-25; Nagahashi et al., 2007), which is considered the distal equivalent of the Kikai Tozurahara (K-Tz) in the absence of proximal glass data (Smith et al., 2013).

New major and trace element glass data from K-Ah samples collected from along the Takatoge Pass and further north at Doimakino (near Aso caldera) verify the correlation of SG06-0967 to the K-Ah eruption (**Supplementary Fig. 1; Fig. 8-9**). Distal K-Ah ash fall recorded in the SG06 record show significant trace element geochemical heterogeneity mirrored by the near source deposits (**Fig. 8-9**). This heterogeneity offers a useful diagnostic feature of this eruption, given that many widespread Japanese tephra are very homogeneous. The major and trace element concentrations of Lake Biwa K-Ah tephra (BIW07-06-1.45m; Kigoshi et al., 2014) are consistent with those of SG06-0967. In turn these data are consistent with BT-3/K-Ah data from Kimura et al. (2015). The most precise eruption age for the K-Ah is derived from the SG06 age-depth model (Smith et al., 2013), which places the eruption at 7,253 ± 46 IntCal13 yrs BP. This tephra has a widespread distribution over Kyushu, Shikoku and much of Honshu Island (**Fig.1**; Machida and Arai, 2003). Consequently, it offers a key chronostratigraphic marker for Holocene palaeoenvironmental and archaeological (Jōmon) sequences (see Moriwaki et al., 2016).

SG06-5151 has a major and trace element composition indistinguishable from the near source deposits of K-Tz collected from Tanegashima and Yaku Islands south-east of Kikai caldera (**Fig. 5; 7; Fig. 8-9**). Despite a slight major element discrepancy between SG06-5151 and BT25 (**Supplementary Figure 1D**; Nagahashi, et al., 2007; Kimura et al., 2015), possibly owing to different analytical conditions; the trace element data here verify their geochemical agreement, and strengthening this tephra tie-point between the two important palaeoclimate records (**Fig. 9A-D**). A diffuse layers of K-Tz is reported in a Uwa Basin core, on Shikoku Island (UT 7.78; Tsuji et al., 2017), however subtle differences exist between the composition of this tephra and the glass data presented here for the K-Tz/SG06-5151 (**Fig.**

9). Given the major element similarity between the evolved (>77 wt.% SiO_2) products of the volcanoes of the Kyushu SVR, this correlation would benefit from more detailed trace element investigations.

K-Tz is not well dated, its stratigraphic position between Ontake-Pm1 (MIS 5.3) and Aso-4 (MIS5.2) sediments mean it has been loosely attributed an age of ca. 95 ka (Smith et al., 2013). Whilst the tephra has a fission track age of 98 ± 26 ka (Danahara, 1995). The SG06 age-depth model is likely to provide one of the most reliable age estimates for this eruption, with an interpolated age of 94.5 ± 4.8 ka (2σ). Consequently, this age can be transferred to other palaeoclimate records preserving the same ash unit, for instance other lacustrine sequences (e.g., Lake Biwa; Nagahashi et al., 2007; **Fig. 12**) and marine records (e.g., East China Sea; Sagawa et al., 2018).

3.2.3.2 Ata Caldera

SG06-5353 has a major and trace element signature consistent with the proximal deposits of the Ata Ignimbrite (**Fig. 8-9**). This tephra is also entirely consistent with the compositions of the Ata co-ignimbrite ash sampled from beneath the Aso-ABCD succession at Noga Cave (**Fig. 9**), and other distal occurrences of the Ata tephra (e.g., UT8.89; Tsuji et al., 2017) Combined proximal, medial and distal major and trace element glass data here confirm that the caldera forming eruption tapped a particularly homogeneous rhyolitic magma **(Fig. 7-10)**. Currently, the age of the widely dispersed Ata tephra (**Fig. 1**) is poorly constrained. Ata stratigraphic positon between MIS5.4 and MIS5.3 in the marine record have been used to infer an age of ca. 105-110 ka (Oba, 1991). Fission Track and K-Ar dating place the eruption age at 100 ± 27 (Danhara, 1995), and 108 ± 3 ka (Matsumoto and Ui, 1997), respectively. The SG06 age-depth model allows us to provide an interpolated age of 99.3 ± 6 ka (2σ) for the Ata eruption.

3.2.3.3 Aira Caldera

SG06-2650 the thickest layer in the SG06 record is related to the rhyolitic caldera forming eruption of Aira- AT (Smith et al., 2013) and is classified as an M 7.9 event. The new trace element data presented here verifies the correlation (**Fig. 8B; 9E-F**), and furthermore provides a strong geochemical match for the AT layer reported in Lake Biwa reinforcing this stratigraphic tie-point between the two records (**Fig. 9E-F**; Kigoshi et al., 2011; Kimura et al., 2015). The AT presents a key widespread tephrostratigraphic marker for Japan being traced across much of Kyushu, Honshu and Hokkaido Islands, and also across the Korean Peninsula (Machida and Arai, 2003**; Fig. 1)**. Its stratigraphic position close to the MIS 3/2 transition enhances its potential as a key marker for assessing spatial variations in

palaeoenvironmental change. Furthermore it is also used to constrain archaeological sequences, specifically the tephra provides a marker separating the Early Upper Palaeolithic and the Late Upper Palaeolithic in Japan (Ono, 2002). The distribution of the tephra is likely to be extended through future cryptotephra studies of Pacific marine cores.

3.2.3.4 Unresolved Kyushu SVR tephra layers

The remaining two layers attributed to explosive volcanism in the Kyushu SVR are more difficult to attribute to a specific source eruption. The dominant glass population of SG06-3668 was correlated to the Sambe Ikeda (SI) eruption (Albert et al., press). This tephra dated by the SG06 age-depth model at 46,295 ± 418 IntCal13 years BP contained a small secondary glass population (Component 2) which revealed volcanic glasses inconsistent with Sambe volcanism based on their multi-element trace element profile (**Fig. 8B**). Albert et al. (in press) indicated that it might reflect contemporaneous activity from another source. Glass chemistry indicates a partial overlap with the eruptive products of the Kyushu SVR, and specifically Aira caldera products (AT; **Supplementary Figure 1**). Trace element data from these glasses show some similarity to the magmas erupted at Aira caldera (**Fig. 8**), however following closer inspection, variation in the trace element compositions of these secondary glasses perhaps indicate multiples sources and indicate analysis of background ash (**Fig. 5**).

SG06-6413 is dated using in the SG06 record at ~125 ka and has a CA affinity which would normally be considered more akin to volcanism on the NEJA, however the trace element concentrations of this tephra are more comparable with a Kyushu SVR origin. Specifically, these low-SiO_2 rhyolites display more elevated Th and Rb content than the most silicic CA products analysed from NEJA sources (**Fig. 5**). While, considerable trace element overlap exists with the products of Kikai caldera, the distal tephra displays far more enriched HREE contents (**Fig. 8A**). Conflicting geochemical features mean the origin of this layer cannot yet be resolved.

3.2.4 Izu-Bonin Arc (Hakone and Fuji)

Tholeiitic (Low-K) tephra layers SG06-6344 (dacite-rhyolite) and SG06-3485 (basaltic-andesite) display trace element signatures that are characterised by low levels of incompatible trace element enrichment, in particular low contents of LILE (e.g., Rb) and HFSE (e.g., Th, U), whilst also displaying flat REE profiles, reflected by low La/Yb ratios (**Fig. 8C**; **Table 4**). Incompatible trace element ratios such as Zr/Y are consistent in the volcanic glasses of SG06-3485 (2.92 ± 0.21 [1σ]) and SG06-6344 (3.12 ± 0.04 [1σ]) which is likely to indicate a similar source region. The nearest and most likely source of Low-K

volcanism to Lake Suigetsu is the northern sector of the Izu-Bonin Arc, and specifically Hakone caldera, whilst more distally tholeiitic (silicic) volcanism is known to occur further south along the Izu-Bonin Arc (Schindlbeck et al., 2018), and at Towada (NEJA) and Mashu (Kurile Arc) calderas (**Fig. 7**).

3.2.4.1 Hakone Caldera

Comparing the major and trace element compositions of SG06-6344 and Hakone tephra (Hk-TAu8) reveals significant similarity; the K_2O content of these Hakone caldera glasses are more comparable than those of Mashu caldera (**Fig, 11A**). Whilst Towada glasses show similar K_2O content, they are lower in FeOt and CaO content relative to the SG06-6344 tephra **(Fig., 10B)**. Both SG06-6344 and Hk-Tau8 share identical trace element profiles (**Fig. 8C**), and overlapping concentrations of incompatible trace elements (**Fig. 10E**). Towada tholeiitic rhyolitic glasses display more elevated contents of Rb, Th, U and LREE compared to SG06-6334 (**Fig. 8C**). Whilst trace element glass data from Mashu caldera enable us to rule out an origin from volcanism along the southern portion of the Kurile arc, owing to the significantly more elevated Nb and Ta contents of the SG06-6344 glasses (**Fig. 8C**).

Glass data strongly support an origin of SG06-6344 from Hakone caldera, the volcano was particularly active between ~100-250 ka based on the intercalation of multiple tephra units within the marine successions (Machida, 2008). Hakone sample Hk-Tau8 was erupted during this interval, yet this deposit is considered too old to be the proximal equivalent of SG06-6344 which has an interpolated age of 123.3 ± 7.5 ka (2σ). Instead it is more probable that the SG06-6344 relates to an eruption from within the Kissawa Lower Pumice series, which represent the youngest activity of this period of intense activity at the volcano. Some of the Kissawa Lower Pumice series deposits are distributed to the west of the volcano. Near-source geochemical investigations are needed to further explore this correlation, and could offer important geochronological constraints on the eruptive history of Hakone caldera.

3.2.4.2 Ko-Fuji

Given that the trace element profile and incompatible trace element ratios of the basaltic-andesite tephra SG06-3485 (**Table 4**; Smith et al., 2013) are very similar to that of the Hakone tephra/SG06-6344 (**Fig. 8**), we must consider that the provenance of this tephra relates to a nearby volcanic source. Marine records indicate that basaltic-andesite deposits are typical of volcanism along the Izu-Bonin arc (Schindlbeck et al., 2018), but the closest source of these compositions to Lake Suigetsu is Mount Fuji west of Hakone caldera, positioned at the junction between the Izu-Bonin Arc and the NEJA (Kaneko et al., 2010).

Marine tephra layers from the Izu-Bonin Arc (Schindlbeck et al., 2018) indicate that the basaltic-andesite products are typically lower in both K_2O and Al_2O_3 at overlapping MgO content compared to the SG06-3485 tephra layer. The high-Al_2O_3 basaltic-andesite tephra in SG06 appears more akin to the Fuji eruptive products (**Fig. 10C-E**). Whole-rock and melt inclusion data from scoria sampled from both Ko- (100-20 ka) and Shin-Fuji (20 ka to present) deposits display more elevated K_2O contents (Togahsi and Terashima, 1997; Watanabe et al., 2006; Kaneko et al., 2010) compared to the basaltic-andesites reported from further south along the Izu-Bonin Arc (**Fig. 10C**). From the sparse data available, the younger Shin-Fuji deposits tend to be more enriched in K_2O contents relative to the older Ko-Fuji deposits, which instead display a lower-K affinity. SG06-3485 displays K_2O contents more consistent with Ko-Fuji activity (**Fig. 10**). The basaltic-andesite deposits of the Ko- and Shin- Fuji can be also be distinguished from those erupted further south along the Izu-Bonin Arc based on their more elevated Zr/Y ratios (**Fig. 10E**). Absolute concentrations of Y and Zr in the eruptive products of Ko- and Shin-Fuji clearly distinguish the products of the two eruptive periods of the volcano, and SG06-3485 glasses are entirely consistent with those of the older Ko-Fuji activities (**Fig. 10E**), which is in agreement with the tephra deposits age in the SG06 record, which at 43,713 ± 300 IntCal13 yrs BP pre-dates Shin-Fuji activity.

Clearly this distal tephra reflects a large magnitude eruption of Ko-Fuji, perhaps its occurrence and thickness (0.5 cm) in Lake Suigetsu 250 km NW of source suggest the eruption was similar in magnitude to the younger Shin-Fuji AD 1707 Plinian eruption (M5.2), which was responsible for ash dispersed up to 250 km east of source (Miyagi, 1984, Machida, 1964). The usefulness of this tephra as marker layer for linking sedimentary archives is still to be explored, given the limited knowledge of the frequency and magnitude of eruptions from Ko-Fuji (Kaneko et al., 2010), and also because these primitive melt compositions are unlikely to yield diagnostic geochemical fingerprints suitable for deciphering successive tephra units erupted from the volcano.

4.1.3.5 Group 5: North East Japan Arc

In the lower portion of the SG06 sequence tephra SG06-6634 displays a CA affinity that is broadly consistent with the eruption deposits of the NEJA, as such they are lower in K_2O at overlapping SiO_2 content with those from the Kyushu SVR or CVR (**Fig. 7**). SG06-6634 is dated at ~130 ka using the SG06 age-depth model, and was previously considered a possible correlative of the Kc-Hb tephra (Smith et al., 2013) Proximal glass data indicate that this tephra is inconsistent with Kutcharo (Kurile Arc) activity owing to their more elevated K_2O (**Fig. 10**) and Nb-Ta content (**Fig. 8D**). The SG06-6634 tephra displays some compositional overlap with the products of Akagi volcano (**Fig., 10A**), however Akagi glasses

display lower FeOt content at overlapping CaO (**Fig. 10B**). The most evolved glasses in the SG06-6344 overlap with the rhyolitic products of Shikotsu caldera, SW Hokkaido (Spfa-1; Fig. 10A-B). Chronologically the Suigetsu tephra cannot be related to this eruption (**Table 1**), yet compositional similarities extend a range of trace elements (**Fig. 8D**), most significantly the more restricted Rb and Th content of the SG06-6344 glasses, a feature of the NEJA tephra units analysed here (**Fig. 5, 8**). For now the precise origin of this tephra remains unresolved.

3.3 The Lake Suigetsu (SG06) tephrostratigraphy

Table 2 and **Figure 11** summarise all the proximal-distal SG06 tephra correlation that have been established using new major and trace element glass data sets presented. The Lake Suigetsu (SG06) record preserves many of the key Japanese widespread tephra layers (**Fig. 11**) recognised by Machida and Arai (2003). The Lake Suigetsu sediment record is recognised as a central node in the tephrostratigraphic framework of Japan, owing to the range of different volcanic sources that have contributed ash fall to the lake (Smith et al., 2011; Smith et al., 2013; McLean et al., 2016; McLean et al., 2018; Albert et al., in press; this study). The prevailing winds mean visible ash fall layers recorded are predominantly from volcanic source regions west of lake (SWJA, the Kyushu CVR and SVR). Explosive volcanism at Daisen (nine layers) and Sambe (five layers) have been the dominant source of ash fall events (Albert et al., in press), whilst visible ash layers are confirmed from a further seven volcanic sources; Aso (three), Kikai (two), Ata (one), Aira (one), Kuju (one). Trace element glass data here enables us to also verify visible ash fall layers from explosive volcanism elsewhere in Japan, including for the moment uncorrelated eruption along the northern Izu-Bonin arc (Hakone, Fuji) and North East Japan Arcs.

Initial cryptotephra investigations conducted on the Lake Suigetsu sediments (SG14 core) indicated that there are significantly more layers preserved non-visibly, with some from very distal sources, for example one cryptotephra layer derived from Mashu caldera over 1000 km NE of the lake (McLean et al., 2018). These cryptotephra layers provide huge potential to further integrate the tephrostratigraphic frameworks of the disparate Japanese source regions. Therefore, resolving major and trace element volcanic glass signatures of the different Japanese source volcanoes is of paramount importance for establishing the origin of such widely dispersed cryptotephra deposits.

Using the stratigraphy and chronology of the SG06 sequence is crucial for refining the Late Quaternary tephrochronology of Japan, particularly since it clearly resolves the relative-age ordering of closely spaced tephrostratigraphic markers. Tephra correlations reveal at least 10 precise tephrostratigraphic ties points linking the Lake Suigetsu (SG06) and Lake Biwa

palaeoclimate archives during the last 100 ka (**Fig. 11**). The SG06 age-depth model provides some of the most reliable age estimates for many of the widespread tephra layers identified which are unsuitable for direct dating methods (e.g., $^{40}Ar/^{39}Ar$). Thus the detailed geochemical fingerprinting presented here for the SG06 tephra layers is fundamental to robustly unlocking this chronological information, and facilitating its transfer into other key palaeoclimate and archaeological archives across East Asia and beyond. Many of the large magnitude eruption deposits recorded in the Lake Suigetsu record are found in marine sequences beyond the Japanese Island (e.g., AT, Aso-4, K-Tz) as such they present an important means to evaluate the synchronous or asynchronous response of terrestrial (e.g., Lake Suigetsu) and marine climate proxies to abrupt Late Quaternary climate variability in East Asia.

4. Conclusions

Numerous tephra layers preserved in the Lake Suigetsu (SG06 core) sediments are associated with large magnitude explosive eruptions and were deposited during the associated widespread ash dispersals, making them key to synchronising palaeoclimate archives across Japan, the NW Pacific and beyond. Crucially they provide an essential means to unlock the unrivalled chronological constraints of this archive, whereby SG06 tephra ages can be transferred into other records (palaeoclimate, archaeological and volcanic) containing the same eruption deposits. This transfer of geochronological information demands high-precision tephra correlations, which is particularly pertinent in distal sedimentary records where multiple volcanic source regions can contribute fine-grained ash fall, often preserved as non-visible (cryptotephra) layers. To facilitate tephra correlations centred on the key Japanese tephrostratigraphic markers we integrate new grain-specific major (EMP) and trace element (LA-ICP-MS) proximal and medial volcanic glass data with existing major element and new trace element glass datasets for the SG06 tephra layers.

These data offer new insights into diagnostic compositional variations of the investigated volcanic sources spanning the Japanese Islands. LILE, K and Rb, are very useful for discriminating the different Japanese volcanic source regions. The forearc calderas of Kyushu (SVR and CVR) are higher in K_2O and Rb contents than those situated along the North East Japan and Kurile Arcs. Thorium behaves broadly similar to K_2O (and Rb), whereby higher K_2O rhyolites from the Kyushu SVR (Kikai, Ata, Aira) and CVR (Aso, Kuju) are more enriched in Th than those from the NEJA (Toya, Shikotsu) or Kurile Arc (Kutcharo). Contents of Nb and Ta also vary significant between different Japanese volcanic sources, with lowest contents associated with lower-K volcanic sources, with the Kurile Arc

(Kutcharo/Mashu) tephra deposits particularly depleted in Nb content. REE element contents can also be useful, Low-Y and HREE content (high-La/Yb ratios) in volcanic glasses is a feature of the SWJA volcanism (Daisen and Sambe), whilst also being recognised at Kuju volcano in the Hohi Volcanic Zone. Flat REE profiles are typically related to Low-K tholeiitic sources, those erupted along the Izu-Bonin arc (Hakone) and Kurile arc (Mashu) show lower La/Yb ratios than those observed along the NEJA (Towada). Glass data presented here from individual volcanoes illustrate issues of repeatedly erupted glass compositions through eruptive successions, highlighting the importance of both the proximal and distal stratigraphic control when underpinning tephra correlations.

The geochemical data are used to validate and refine the tephrostratigraphy of the SG06 record **(Fig. 11)**. Here we are able to offer new chronological constraints on the explosive volcanism at calderas situated along the Kyushu Arc, including Kikai, Ata and Aso. Correlations between the SG06 tephra layers and eruption units at Aso caldera demonstrate the two-way transfer of geochronological information. Proximal Aso-4 (Magnitude 7.7) eruption deposits are proximally dated here by $^{40}Ar/^{39}Ar$ at 86.4 ± 1.1 ka (2σ), and provide a chronological anchor (SG06-4963) to the Lake Suigetsu age model beyond the radiocarbon timeframe. Distal ash fall from Plinian eruption of Aso are dated using the SG06 age-depth model, Aso-A (SG06-5287) is dated at 97.9 ± 6.0 ka, whilst a younger eruption, Aso central cone pumice 4 (SG06-3912) is more precisely dated precisely at 50.0 ± 0.3 ka (2σ). Proximal-distal correlations between the volcanic stratigraphy of Aso caldera and the SG06 record provide important new constraints on the tempo of explosive activity at this volcano. Whilst the prevailing winds mean visible ash fall layers recorded in Lake Suigetsu are predominantly from volcanic source regions west of lake (SWJA, Kyushu CVR and SVR), trace element glass data here enables us to also verify visible ash fall layers from explosive volcanism elsewhere in Japan, including the Izu-Bonin and North East Japan Arcs.

Acknowledgements

References

Acocella, V., Yoshida, T., Yamada, R., Funiciello, F., 2008. Structural control on late Miocene to Quaternary volcanism in the NE Honshu arc, Japan. Tectonics 27 (5), https://doi.org/10.1029/2008TC002296

Albert, P.G., Smith, V.C., Suzuki, T., Tomlinson, E.L., Nakagawa, T., McLean, D., Yamada, M., Staff, R.A., Schlolaut, G., Takemura, K., Nagahashi, Y., Kimura, J-I, Suigetsu 2006 Project Members in press. Constraints on the frequency and dispersal of explosive eruptions at Sambe and Daisen volcanoes (South-West Japan Arc) from the distal Lake Suigetsu record (SG06 core). Earth-Science Reviews

Albert, P.G., Tomlinson, E.L., Lane, C.S., Wulf., S., Smith, V.C., Coltelli, M., Keller, J., Lo Castro, D., Manning, C.J., Muller, W., Menzies, M.A., 2013. Late glacial explosive activity on Mount Etna: implications for proximal-distal tephra correlations and the synchronisation of Mediterranean archives. Journal of Volcanology and Geothermal Research, 265, 9-26.

Albert, P.G. et al. (2012). Marine-continental tephra correlations: Volcanic glass geochemistry from the Marsili Basin and the Aeolian Islands, Tyrrhenian Sea, Italy. Journal of Volcanology and Geothermal Research 229-230, 74–94.

Aoki., K., 2008. Revised age and distribution of ca. 87ka Aso-4 tephra based on new evidence from the northwest Pacific Ocean. Quaternary International 178 (1), 100-118.

Andersen, K.K. et al. (2004). High-resolution record of Northern Hemisphere climate extending into the last interglacial period. Nature 431, 147-151.

Bourne., A. J., Abbott, P.M., Albert, P.G., Cook, E., Pearce, N.J.G., Ponomareva, V., Svensson, A., Davies, S.M., 2016. Underestimated risks of recurrent long-range ash dispersal from northern Pacific Arc volcanoes. Nature Scientific Reports 6, 2983. doi:10.1038/srep29837

Bronk Ramsey, C. et al. (2012). A Complete Terrestrial Radiocarbon Record for 11.2 to 52.8 kyr B.P. Science 338, 370–374.

Crosweller, H.S., Arora, B., Brown, S.K., Cottrell, E., Deligne, N.I., Guerrero, N.O., Hobbs, L., Kiyosugi, K., Loughlin, S.C., Lowndes, J., Nayembil, M., Siebert, L., Sparks, R.S.J., Takarada, S., Venzke, E., 2012. Global database on large magnitude explosive volcanic eruptions (LaMEVE). Journal of Applied Volcanology 1:4. https://doi.org/10.1186/2191-5040-1-4

Danhara, T., 1995. Towards precise measurement of zircon and glass fission track geochronology for Quaternary tephras. The Quaternary Research (Japan), 34 (1995), pp. 221-237 (In Japanese with English captions).

Dansgaard, W. et al. (1993). Evidence for general instability of past climate from a 250-kyr ice-core record. Nature 364, 218-220.

Derkachev, A.N., Nikolaeva, N.A., Gorbarenko, S.A., Portnyagin, M.V., Ponomareva, V.V., Nürnberg, D., Sakamoto, T., Iijima, K., Liu, Y., Shi, X., Lv, H., Wang, K., 2016. Tephra layers of in the quaternary deposits of the Sea of Okhotsk: Distribution, composition, age and volcanic sources. Quaternary International 425, 248-272.

Hayakawa, Y., 2010. Hayakawa's 2000-year eruption database and one million year tephra database. http://www.hayakawayukio.jp/database. Updated regularly.

Hayakawa Y (1985) Pyroclastic geology of Towada volcano. Bull Earthq Res Inst. Univ Tokyo 60:507–592.

Ikehara, K., Usami, K., Kanamatsu, T., Arai, K., Yamaguchi, A., Fukuchi, R., (2017). Spatial variability in sediment lithology and sedimentary processes along the Japan Trench: use of deep-sea turbidite records to reconstruct past large earthquakes. Geological Society, London, Special Publications, 456, 3. https://doi.org/10.1144/SP456.9

Ikehara, K., Kikkawa, K., Chun, J-H., 2004. Origin and Correlation of Three Tephras That Erupted During Oxygen Isotope Stage 3 Found in Cores from the Yamato Basin, Central Japan Sea. The Quaternary Research 43, 201-212. In Japanese.

Jensen, B.J.L. Pyne-O'Donnell, S., Plunkett, G., Froese, D.G., Hughes, P.D.M., Sigl, M., McConnell, J.R., Amesbury, Matthew J. Blackwell, P.G., van den Bogaard, C., Buck, C.E., Charman, D.J., Clague, J.J., Hall, V.A., Koch, J., Mackay, H., Mallon, G., McColl, L., Pilcher, J.R., 2014. Transatlantic distribution of the Alaskan White River Ash. Geology (2014) 42 (10): 875-878.

Kaneko, K., Inoue, K., Koyaguchi, T., Yoshikawa, M., Shibata, T., Takahashi, T., Furukawa, K., 2015. Magma plumbing system of the Aso-3 large pyroclastic eruption cycle at Aso volcano, Southwest Japan: Petrological constraint on the formation of a compositionally stratified magma chamber. Journal of Volcanology and Geothermal Research 303, 41-58. https://doi.org/10.1016/j.jvolgeores.2015.07.016

Kaneko, T., Yasuda, A., Fujii, T., Yoshimoto, M., 2010. Crypto-magma chambers beneath Mt. Fuji. Journal of Volcanology and Geothermal Research 193 (3-4), 161-170.

Kigoshi, T., Kumon, F., Hayashi, R., Kuriyama, M., Yamada, K., Takemura, K., 2014. Climate changes for the past 52 ka clarified by total organic carbon concentrations and pollen composition in Lake Biwa, Japan. Quaternary International 333, 2-12.

Kishimoto, H., Hasegawa, T., Nakagawa, M., Wada, K., Tephrostratigraphy and eruption style of Mashu volcano, during the last 14,000 years, eastern Hokkaido, Japan. Bulletin of Volcanological Society of Japan 54, 15-36 (in Japanese with English abstract)

Kitagawa, H., Fukuzawa, H., Nakamura, T., Okamura, M., Takemura, K., Hayashida, A., Yasuda, Y., 1995. AMS ^{14}C dating of varved sediments from lake Suigetsu, Central Japan and atmospheric 14C change during the Lake Pleistocene. Radiocarbon 37, 371-378.

Kitagawa, H. and van der Plicht, J. 1998a. Atmospheric radiocarbon calibration to 45,000 yr B.P.: Late Glacial fluctuations and cosmogenic Isotope production, Science, 279: 1187-1190

Kitagawa, H. and van der Plicht, J. 1998b. A 40,000-year varve chronology from Lake Suigetsu, Japan; extending the (super 14) C calibration curve, Radiocarbon, 40: 505-515

Kitagawa, H. and van der Plicht, J. 2000. Atmospheric radiocarbon calibration beyond 11,900 cal Bp from Lake Suigetsu laminated sediments, Radiocarbon, 42: 370-381.

Kimura, J.-I. (1996). Near synchroneity and periodicity of Quaternary explosive volcanism in the southern segment of Tohoku-honshu arc: a study facilitated by tephrochronology. Quaternary International 34–36, 99–105.

Kimura, J-I., Nagahashi, Y., Satoguchi, Y., Chang, Q., 2015. Origins of felsic magmas in Japanese subduction zone: Geochemical characterizations of tephras from caldera-forming eruptions <5Ma. Geochem. Geophys. Geosysts., 16, 2147-2174, doi:10.1002/2015GC005854.

Kimura, J-I, Yoshida, T., 2006. Contributions of Slab Fluid, Mantle Wedge and Crust to the Origin of Quaternary Lavas in the NE Japan Arc. Journal of Petrology 47 (11), 2185-2232. doi:10.1093/petrology/egl041.

Kimura, J-I., Okada, S., Nakayama, K., Umeda, K., Kusano, T., Asahara, A., Tateno, M., Danhara, T., 1999. Fission Track Ages of Tephras from Daisen and Sambe Volcanoes and Their Volcanological Implications. Quaternary Research (Daiyonki-Kenkyu) 38, 145-155.

Lee, J. Y., Marti, K., Severinghaus, J. P., Kawamura, K., Yoo, H. S., Lee, J. B. and Kim, J. S., 2006. A redetermination of the isotopic abundances of atmospheric Ar. Geochimica et Cosmochimica Acta, 70 (17), pp. 4507-4512.

Lane, C.S., Brauer, A., Blockley, S.P.E., Dulski, P., 2013. Volcanic ash reveals time-transgressive abrupt climate change during the Younger Dryas. Geology 41 (12): 1251-1254.

Machida, H., 1964. Tephrochronological study of volcano Fuji and adjacent areas. J. Geogr. (Tokyo), 73, 293-308 (in Japanese with English Abstract).

Machida, H. 2008 Geomorphology and geology in the South Kanto District during the Last 420 ka: An overview. in The Japan Association for Quaternary Research 2009. Digital book: Progress in Quaternary Research in Japan, Japan Association for Quaternary Research, CD-ROM and booklet, 30p. (in Japanese).

Machida, H. and Arai, F., 2003. Atlas of tephra in Japan and its surrounding area, 2nd edition. University of Tokyo Press, Tokyo, 336p. (In Japanese, title translated).

Machida, H., 1999. Quaternary Widespread Tephra Catalog in and around Japan: Recent Progress. The Quaternary Research (Daiyonki-Kenkyu) 38, 194-203.

Mahoney, S.H., Wallace, M.L., Miyoshi, M., Villamor, P., Sparks, R. S. J., Hasenaka, T., (2011), Volcano-tectonic interactions during rapid plate-boundary evolution in the Kyushu region, SW Japan, Geol. Soc. Am. Bull., 123, 2201–2233, doi:10.1130/B30408.1.

Mark, D. F., Gonzalez, S., Huddart, D. and Böhnel, H., 2010. Dating of the Valsequillo volcanic deposits: Resolution of an ongoing archaeological controversy in Central Mexico. Journal of human evolution, 58 (5), pp. 441-445.

Mark, D. F., Stuart, F. M. and de Podesta, M., 2011. New high-precision measurements of the isotopic composition of atmospheric argon. Geochimica et Cosmochimica Acta, 75 (23), pp. 7494–7501.

Mark, D.F., Renne, P.R., Dymock, R.C., Smith, V.C., Simon, J.I., Morgan, L.E., Saff, R.A., Ellis, B.S., Pearce, N.J.G., 2017. High precision 40Ar/39Ar dating of Pleistocene tuffs and temporal anchoring of the Matuyama-Brunhes Boundary. Quaternary Geochronology, 39, 1-23.

Marshall, M., Schlolaut, G.,Nakagawa, T.,Lamb, H., Brauer, A., Staff, R., Bronk Ramsey, C., Tarasov, P., Gotanda, K., Haraguchi, T., Yokoyama, Y., Yonenobu, H., Tada, R., Suigetsu 2006 Project Members, 2012. Anovel approach to varve counting using mXRF and X-radiography in combination with thin-section microscopy, applied to the Late Glacial chronology from Lake Suigetsu, Japan. Quaternary Geochronology 13, 70-80.

Matsumoto, A, Ui, T., 1997. K-Ar age of Ata pyroclastic flow deposit, Southern Kyushu, Japan. Bulletin of the Volcanological Society of Japan, 42 (1997), pp. 223-225 (in Japanese with English abstract).

McLean, D., Albert, P.G., Nakagawa, T., Suzuki, T., Yamada, K., Kitaba, Haraguchi, T., Kitagawa, J., SG14 Project Members, Smith, V.C., in prep. Refined Lake Suigetsu (central Japan) visible tephrostratigraphy using the SG14 core. Journal of Quaternary Science.

McLean, D., Albert, P.G., Nakagawa, T., Suzuki, T., Staff, R.A., Yamada, K., Kitaba, I., SG14 Project Members, Smith, V.C., (2018). Integrating the Holocene tephrostratigraphy for East Asia using a high-resolution cryptotephra study from Lake Suigetsu (SG14 core), central Japan. Quaternary Science Reviews, 183, 36-38.

McLean, D., Albert, P.G., Nakagawa, T., Staff, R., Suzuki, T., Suigetsu 2006 Project Members; Smith, V.C., 2016. Identification of the Changbaishan 'Millennium' (B-Tm) eruption in the Lake Suigetsu (SG06) sedimentary archive, Japan: Synchronisation of hemispheric-wide palaeoclimate archives. Quaternary Science Reviews 150, 301-307.

Moriwaki, H., Nakamura, N., Nagasako, T., Lowe, D.J., Sangawa, T., 2016. The role of tephra in developing chronostratigraphy for palaeoenvironmental reconstruction and archaeology in southern Kyushu, Japan, since 30,000 cal. BP: An integration. Quaternary International 397, 79-92.

Miyabuchi, Y., 2009. A 90,000-year tephrostratigraphic framework of Aso Volcano, Japan. Sedimentary Geology 220 (3–4), 169-189. https://doi.org/10.1016/j.sedgeo.2009.04.018.

Miyabuchi, Y., 2011. Post-caldera explosive activity inferred from improved 67-30 ka tephrostratigraphy at Aso Volcano, Japan. Journal of Volcanology and Geothermal Research, 205(3-4), 94-113. doi: 10.1016/j.jvolgeores.2011.05.004

Miyaji, N., 1984. Wind effect on the dispersion of the Fuji 1707 Tephra. Bull. Volcanol. Soc. Jpn., 29 (Second Series) 17-30 (in Japanese with English abstract).

Nakagawa, T. et al. (2003). Asynchronous Climate Changes in the North Atlantic and Japan During the Last Termination. Science 299, 688–691.

Nakagawa, T. et al. (2012). SG06, a fully continuous and varved sediment core from Lake Suigetsu, Japan: stratigraphy and potential for improving the radiocarbon calibration model and understanding of late Quaternary climate changes. Quaternary Science Reviews 36, 164–176

Niespolo, E.M., Rutte, D., Deino, A.L. & Renne, P.R. (2017) Intercalibration and age of the Alder Creek sanidine 40Ar/39Ar standard. Quaternary Geochronology, 39, 205-213.

Nomade, S., Renne, P. R., Vogel, N., Deino, A. L., Sharp, W. D., Becker, T. A., Jaouni, A. R. and Mundil, R., 2005. Alder Creek sanidine (ACs-2): A Quaternary 40Ar/39Ar dating standard tied to the Cobb Mountain geomagnetic event. Chemical Geology, 218 (3-4), pp. 315-338.

Oba, T., 1991. The eruptive age of Aso-4 and Ata tephra on the basis of the oxygen isotopic stratigraphy. The Earth Monthly (Gekkan Chikyu), 13 (1991), pp. 224-227 (In Japanese)

Okuno, M., Nagaoka, S., Saito-Kokuba, Y., Nakamura, T., Kobayashi, T., 2017. AMS radiocarbon dates of pyroclastic-flow deposits on the southern slope of the Kuju volcanic group, Kyushu, Japan. Radiocarbon 59, 483-488.

Ono, K., Matsumoto, Y., Miyahisa, M., Teraoka, Y., and Kanbe, N., (1977). Geology of the Taketa district. Quadrangle series, scale 1:50,000. Geol. Surv. Japan, 145 pp.

Plunkett, G., Coulter, S.E., Ponomareva, V.V., Blaauw, M., Klimaschewski, A., Hammarlund, D., 2015. Distal tephrochronology in volcanic regions: Challenges and insights from Kamchatkan lake sediments. Global and Planetary Change 134, 2015, 26-40 https://doi.org/10.1016/j.gloplacha.2015.04.006.

Pyle, D.M., 2000. Sizes of volcanic eruptions. In Encyclopedia of Volcanoes. Edited by: Sigurdsson H, Houghton BF, McNutt SR, Rymer H, Stix J. Academic Press, London; 2000.

Pyne-O'Donnell, S.D.F., Hughes, P.D.M., Froese, D.G., Jensen, B.J.L., Kuehn, S.C., Mallon, G., Amesbury, M.J., Charman, D.J., Daley, T.J., Loader, N.J., Mauquoy, D., Street-Perrott, A., Woodman-Ralph, J., 2012. High-precision ultra-distal Holocene tephrochronology in North America. Quaternary Science Reviews 52, 6-11. https://doi.org/10.1016/j.quascirev.2012.07.024.

Razzhigaeva, N.G., Matsumoto, A., Nakagawa, M., 2016. Age, source, and distribution of Holocene tephra in the southern Kurile Islands: Evaluation of Holocene eruptive activities in the southern Kurile arc. Quaternary International 397, 63-78. https://doi.org/10.1016/j.quaint.2015.07.070

Reimer, P.J., Bard, E., Bayliss, A., Beck, J.W., Blackwell, P.G., Ramsey, C.B., Buck, C.E., Cheng, H., Edwards, R.L., Friedrich, M. and Grootes, P.M. 2013. IntCal13 and Marine13 radiocarbon age calibration curves 0–50,000 years cal BP. Radiocarbon, 55: 1869-1887.

Renne, P. R. and Norman, E. B., 2001. Determination of the half-life of ^{37}Ar by mass spectrometry. Physical Review C, 63 (4), 047302.

Renne, P. R., Sharp, Z. D. and Heizler, M. T., 2008. Cl-derived argon isotope production in the CLICIT facility of OSTR reactor and the effects of the Cl-correction in $^{40}Ar/^{39}Ar$ geochronology. Chemical Geology, 255 (3-4), pp. 463-466.

Renne, P.R., Cassata, W.S. & Morgan, L.E., 2009. The isotopic composition of atmospheric argon and $^{40}Ar/^{39}Ar$ geochronology: Time for a change? Quaternary Geochronology, 4 (4), pp. 288-298.

Renne, P. R., Mundil, R., Balco, G., Min, K. and Ludwig, K. R., 2010. Joint determination of ^{40}K decay constants and $^{40}Ar*/^{40}K$ for the Fish Canyon sanidine standard, and improved accuracy for $^{40}Ar/^{39}Ar$ geochronology. Geochimica et Cosmochimica Acta, 74 (18), pp. 5349–5367.

Renne, P.R., Mundil, R., Balco, G., Min, K. and Ludwig, K. R., 2011. Response to the comment by W. H. Schwarz et al. on "Joint determination of 40K decay constants and $^{40}Ar*/^{40}K$ for the Fish Canyon sanidine standard, and improved accuracy for $^{40}Ar/^{39}Ar$ geochronology. Geochimica et Cosmochimica Acta, 75, pp. 5097-5100.

Sagawa, T., Nagahashi, Y., Satoguchi, Y., Holbourn, A., Itaki, T., Gallagher, S.J., Saavedra-Pellitero, M., Ikehara, K., Irino, T., Tada, R., 2018. Integrated tephrostratigraphy and stable isotope stratigraphy in the Japan Sea and East China Sea using IODP Sites U1426, U1427, and U1429, Expedition 346 Asian Monsoon. Progress in Earth and Planetary Science 5:18 https://doi.org/10.1186/s40645-018-0168-7

Schindlbeck, J.C., Kutterolf, S., Straub, S.M., Andrews, G.D.M., Wang, K-L., Mleneck-Vautravers, M.J., 2018. One Million Years tephra record at IODP Sites U1436 and U1437: Insights into explosive volcanism from the Japan and Izu arcs. Island Arc 27 (3). https://doi.org/10.1111/iar.12244

Schlolaut, G., Marshall, M., Brauer, A., Nakagawa, T., Lamb, H., Staff, R., Bronk Ramsey, C., Bryant, C., Brock, F., Kossler, A., Tarasov, P., Yokoyama, Y., Tada, R., Haraguchi, T., Suigetsu 2006 Project Members, 2012. An automated method for varve interpolation and its application to the Late Glacial chronology from Lake Suigetsu, Japan. Quaternary Geochronology 13, 52e69. http://dx.doi.org/10.1016/j.quageo.2012.07.005.

Shibata, T., Yoshikawa, M., Itoh, J-I., Ujike, O., Miyishi, M., Takemura, K., 2014. Along-arc geochemical variations in Quaternary magmas of northern Kyushu Island, Japan. In Gomez-Tuena, A., Straub, S.M., Zellmer, G.F. (Eds). Orogenic Andesites and Crustal Growth. Geological Society, London, Special Publications, 385, 15–29.

Smith, V.C., Isaia, R., Engwell, S., Albert, P.G., 2016. Tephra dispersal during the Campanian Ignimbrite (Italy) eruption: implications for ultra-distal ash transport during the large caldera-forming eruption. Bulletin of Volcanology 78:45.

Smith, V.C., Staff, R.A., Blockley, S.P.E., Bronk Ramsey, C., Nakagawa, T., Mark, D.F., Takemura, K., Danhara, T., Suigetsu Project Members, 2013. Identification and correlation of visible tephras in the Lake Suigetsu SG06 sedimentary archive, Japan: chronostratigraphic markers for synchronising of east Asian/west Pacific palaeoclimatic records across the last 150 ka. Quaternary Science Reviews 67, 121-137.

Smith, V.C., Smith, V.C., Mark, D.F., Staff, R.A., Blockley, S.P.E., Bronk-Ramsey, C., Bryant, C.L., Nakagawa, T., Han, K.K., Weh, A., Takemura, K., Danhara, T., Suigetsu 2006 Project Members, 2011b. Toward establishing precise Ar/Ar chronologies for Late Pleistocene palaeoclimate archives: an example from the Lake Suigetsu (Japan) sedimentary record. Quat. Sci. Rev. 30, 2845–2850.

Stoenner, R.W., Oa, S. & Katcoff, S., 1965. Half-Lives of Argon-37 Argon-39 and Argon-42. Science, 148(3675), pp. 1325.

Sun, S., McDonough, W.F., 1989. Chemical and isotopic systematics of 630 oceanic basalts: implications for mantle composition and processes. In: 631 A.D. Saunders, Norry, M.J. (Editor), Magmatism in Ocean Basins.

Staff, R.A., Bronk Ramsey, C., Bryant, C.L., Brock, F., Payne, R.L., Schlolaut, G., Marshall, M.H., Brauer, A., Lamb, H.F., Tarasov, P.E., Yokoyama, Y., Haraguchi, T., Gotanda, K., Yonenobu, H., Nakagawa, T., Suigetsu 2006 Project Members, 2011. New C-14 determinations from Lake Suigetsu, Japan: 12,000 to 0 cal BP. Radiocarbon 53, 511-528.

Staff, R.A., Nakagawa, T., Schlolaut, G., Marshall, M.H., Brauer, A., Lamb, H.F., Bronk Ramsey, C., Bryant, C.L., Brock, F., Kitagawa, H., van der Plicht, J., Payne, R.L., Smith, V.C., Mark, D.F., MacLeod, A., Blockley, S.P.E., Schwenninger, J., Tarasov, P.E., Haraguchi, T., Gotanda, K., Yonenobu, H., Yokoyama, Y., Suigetsu 2006 Project Members., 2013a. The multiple chronological techniques applied to the Lake Suigetsu (SG06) sediment core. Boreas, 42, 2, 259-266.

Staff, R.A., Schlolaut, G., Bronk Ramsey, C., Bronk, F., Bryant, C.L., Kitagawa, H., van der Plicht, J., Marshall, M.H., Brauer, A., Lamb, H.F., Payne, R.L., Tarasov, P.E., Haraguchi, T., Gotanda, K., Yonenobu, Y., Nakagawa, T., 2013b. Integration of the old and new Lake Suigetsu (Japan) terrestrial radiocarbon calibration data sets. Radiocarbon 55, 4, 2049-2058.

Steffensen, J.P., Andersen, K.K., 1, Bigler, M., Clausen, H.B., Dahl-Jensen, D., Fischer, H., Goto-Azuma, K., Hansson, M., Johnsen, S.J., Jouzel, J., Masson-Delmotte, V., Popp, T., Rasmussen, S.O., Röthlisberger, R., Ruth, U., Stauffer, B., Siggaard-Andersen, M-L., Sveinbjörnsdóttir, A.E., Svensson, A., , White, J.W.C 2008. High-Resolution Greenland Ice Core Data Show Abrupt Climate Change Happens in Few Years. Science 321, Issue 5889, pp. 680-684. DOI: 10.1126/science.1157707

Tani, K., Fiske, R.S., Dunkley, D.J., Ishizuka, O., Oikawa, T., Isobe, I., Tatsumi, Y., 2011. The Izu Peninsula, Japan: Zircon geochronology reveals a record of intra-oceanic rear-arc magmatism in an accreted block of Izu–Bonin upper crust. Earth and Planetary Science Letters 303, Issues 3–4, 225-239.

Togashi, S., Terashima, S., 1997. The behaviour of gold in unaltered island arc tholeiitic rocks from Izu-Oshima, Fuji, and Osoreyama volcanic areas, Japan. Geochimica et Cosmochimica Acta, Volume 61 (3), 543-554. doi: 10.1016/S0016-7037(96)00369-9

Tomlinson, E.L., Albert, P.G., Wulf, S., Brown, R., Smith, V.C., Keller, J., Orsi, G., Bourne, A.J., Menzies, M.A. 2014. Age and geochemistry of tephra layers from Ischia, Italy: constraints from proximal-distal correlations with Lago Grande di Monticchio. Journal of Volcanology and Geothermal Research, 287, 22-39.

Tsuji, T., Ikeda, M., Kishimoto, H., Fujita, K., Nishizaka, N., Onishi, K., 2017. Tephra fallout Hazard assessment for VEI5 Plinian Eruption at Kuju Volcano, Japan, Using TEPHRA2. IOP Conf. Series: Earth and Environmental Sciences 71. doi :10.1088/1755-1315/71/1/012002

Tsuji,T., Ikeda, M., Furusawa, A., Nakamura, C., Ichikawa, K., Yanagida, M., Nishizaka, N., Ohnishi, K., Ohno, Y., 2017. High resolution record of Quaternary explosive volcanism recorded in fluvio-lacustrine sediments of the Uwa basin, southwest Japan. Quaternary International 471, 278-297 doi.org/10.1016/j.quaint.2017.10.016.

Watanabe, S., Widom, E., Ui, T., Miyaji, N., Roberts, A.M., 2006. The evolution of a chemically zoned magma chamber: The 1707 eruption of Fuji volcano, Japan. Journal of Volcanology and Geothermal Research 152, Issues 1–2, 1-19.

Wulf, S., Kraml, M., Brauer, A., Keller, J., Negendank, J.F.W., 2004. Tephrochronology of the 100 ka lacustrine sediment record of Lago Grande di Monticchio (southern Italy). Quaternary International 122, 7–30.

Wulf, S., Keller, J., Paterne, M., Mingram, J., Lauterbach, S., Opitz, S., Sottili, G., Giaccio, B., Albert, P.G., Satow, C., Tomlinson, E.L., Viccaro, M., Brauer, A., 2012. The 100-133 ka record of Italian explosive volcanism and revised tephrochronology of Lago Grande di Monticchio. Quaternary Science Reviews, 58, 104-123.

Yoshida, T., et al. (2013), Evolution of late Cenozoic magmatism and the crust-mantle structure in the NE Japan Arc, Geol. Soc. Spec. Publ., 385, 335–387, doi:10.1144/SP385.15.

Zhao, D., Yanada, T., Hasegawa, A., Umino, N., Wei, W., 2012. Imaging the subducting slabs and mantle upwelling under the Japanese Islands. Geophysical Journal International, Volume 190, Issue 2, 1 August 2012, Pages 816–828, https://doi.org/10.1111/j.1365-246X.2012.05550.

Table Captions

Table 1: Eruption deposits the focus of geochemical characterisation spanning the Japanese Islands. Those stared and marked in bold are recognised as widespread Japanese tephra markers (Machida and Arai, 2003). Dispersal, eruption magnitudes and volumes estimates follow Machida and Arai (2003), and the LaMEVE database (Crosweller et al, 2012). Magnitude calculations follow Pyle (2000). Corresponding sampling localities are listed in Supplementary Table 1. Pum = Pumice; Ign. = Ignimbrite.

Table 2: The visible SG06 tephra layers which have been the focus of trace element geochemical fingerprinting. Also shown are the arc region, source and eruption specific correlations based on the geochemical data presented. The core sections marked in bold were sampled for chemical analysis. Composite depth of the base of the tephra is taken from the SG06 correlation model. Ages in IntCal13 yrs BP are provided for all tephra layers within the ^{14}C timeframe (<50 ka) and beyond are presented in ka (uncertainties represent either 95.4%, or 2σ).

Table 3: Major and trace element glass chemistry of proximal deposits investigated to develop a reference glass dataset associated with large magnitude eruptions at Japanese volcanic sources.

Table 4: Major and trace element glass chemistry of SG06 tephra layers correlated to source volcanic deposits in this contribution. *represents major element glass data as presented in Smith et al. (2013) and C = Component.

Supplementary Table 1: Eruption deposits the focus of geochemical characterisation spanning the Japanese Islands. Sampling localities of tephra deposits analysed, along with eruption details, dispersal, eruption magnitudes and volumes estimates follow Machida and Arai (2003), and the LaMEVE database (Crosweller et al, 2012).

Figure 1: A map of the Japanese islands, showing the volcanic centres that were active in the Late Quaternary and the location of the Lake Suigetsu (SG06) record (black square). Those volcanoes labelled in bold have been subjected to detailed major and trace element characterisation for the purpose of geochemically characterising the different volcanic region (**Table 1**). Labelled in red are the portions of the Japanese Island arc which are referred to through the manuscript. Isopach maps are presented for the Late Quaternary key widespread Japanese tephrostratigraphic markers following Machida and Arai (2003), and for tephra labelling of the individual eruption deposits refer to **Table 1**. HVZ is the Hohi Volcanic Zone (HVZ) in central-northern Kyushu and is marked by a red dotted envelope.

Figure 2: Major element geochemical variability of volcanic glasses analysed from large magnitude silicic eruption of Japanese volcanic centres spanning the last ca. 150 ka. Glasses at Japanese volcanic sources range from Low-K (Tholeiitic) to High-K (Calc-alkaline)/Shoshonitic affinities, with deposits of the large magnitude eruptions investigated dominated rhyolitic tephra units (>70 wt.% SiO_2). Error bars on plots represent reproducibility, calculated as a 2 x standard deviation of replicate analysis of MPI-DING StHs6/80-G

Figure 3: Selected major and trace elements useful for recognising chemo-spatial variations in volcanic glasses erupted in the different Japanese volcanic regions.

Figure 4: Average Primitive Mantle normalised volcanic glass compositions for representative near-source (proximal) large magnitude eruption deposits investigated here and considered representative of the various arc regions of Japan. Primitive mantle values used for normalisation follow Sun and McDonough (1989). Envelope for SWJA eruption deposits of Daisen and Sambe volcanoes follow Albert et al. (in press).

Figure 5: Trace element bi-plots considered useful for depicting the compositional variation of the eruptive products investigated from the various Japanese sources. The envelope for Daisen and Sambe volcanoes (SWJA) are based on data presented in Albert et al. (in press), interestingly Kuju volcano share a similar low-Y feature. Error bars on plots represent reproducibility, calculated as a 2 x standard deviation of replicate analysis of MPI-DING StHs6/80-G

Figure 6: Geochemical variability in the near-source volcanic glasses of Aso caldera eruption deposits spanning between ca. 50 and 135 ka. Shown are glass data for SG06 tephra deposit related to large magnitude eruptions at Aso caldera (SG06-3912/ACP4; SG06-4963/Aso-4 and SG06-5287/Aso-A). Also presented are a selection of distal ash layers related to explosive volcanism at Aso caldera, and in some instances have been used to construct age-depth models for their host sedimentary records (Schindlebeck et al. 2018; Sagawa et al., 2018). Error bars on plots represent reproducibility, calculated as a 2 x standard deviation of replicate analysis of MPI-DING StHs6/80-G

Figure 7: SG06 tephra layers discussed compared to the near-source (proximal) volcanic glass data sets presented and discussed here. Error bars on plots represent reproducibility, calculated as a 2 x standard deviation of replicate analysis of MPI-DING StHs6/80-G.

Figure 8: Average Primitive Mantle normalised volcanic glass compositions for representative SG06 visible tephra layers investigated and discussed here. Primitive mantle values used for normalisation follow Sun and McDonough (1989). Envelope for SWJA (Daisen and Sambe) volcanoes follow Albert et al. (in press), with the exception of the Izu Arc Basalts field generated using data presented in Schindlebeck et al., (2018), the remaining envelopes are based on near-source data presented in this study.

Figure 9: Trace element volcanic glass data from large magnitude eruption deposits from the Kyushu SVR compared distal equivalents preserved in the Lake Suigetsu (SG06) sedimentary record. References: (1) Kimura et al., 2015; (2) Maruyama et al., 2016. Error bars on plots represent reproducibility, calculated as a 2 x standard deviation of replicate analysis of MPI-DING StHs6/80-G.

Figure 10: Major and trace element glasses analyses of Lake Suigetsu tephra deposits SG06-3485, SG06-6344, SG06-6413 and SG06-6634 compared to potential volcanic source data either included in this study or existing datasets (1) Hakone: Suzuki et al., unpublished; (2) Akagi: Suzuki et al., unpublished (3) Fuji: Kaneko et al., 2010; (4) Fuji: Togahsi and Terashima, 1997 (5) Izu-Bonin Arc: Schindlebeck et al., (2018).

Figure 11: The integrated proximal-distal event stratigraphy of SG06 visible tephra layers, with correlations to other sedimentary records are also depicted including Lake Biwa (**Fig. 1**). The SG06 tephra ages are shown as IntCal13 yrs BP in the radiocarbon timeframe (95.4 %). Beyond the annually laminated and ^{14}C dated portion of the sequence, the age-depth model is based on a linear interpolation that is anchored to deeper chronological tie points, which now include the new ^{40}Ar/^{39}Ar age of the Aso-4 eruption deposit (e.g., SG06-4963). All ages reported that are outside the ^{14}C timeframe are provided in ka with 2σ errors (equivalent to 95.4% probability range).

Supplementary Figure 1: Major element volcanic glass data from large magnitude eruption deposits from the Kyushu SVR compared distal equivalents preserved in the Lake Suigetsu (SG06) sedimentary record. Error bars on plots represent reproducibility, calculated as a 2 x standard deviation of replicate analysis of MPI-DING StHs6/80-G.

Volcano	Eruption *	Tephra	Magnitude (M)	Volume (km³)	Dispersal	Eruption style	Sampled	Sample Ref. (ITJ)	Age cal yrs BP or Ka (95.4%)
Kyushu Southern Volcanic Region (SVR)									
Kikai	**Akahoya ***	K-Ah	7.3	150	NE	Ign. (+Co)	ash	3 / 20	7,165-7,303
	Tozurahara*	K-Tz	6.0	150	NE (radial)	Ign. (+Co)	ash	241 / 240	~95
Ata (Ibusuki Volcanic field)	Ikeda	Ik	5.4	2.3	E	Plinian Fall	Pum	53	6,600
	Ata*	Ata	7.5	350	NE	Ign. (+Co)	Pum./ash	9 / 51 / 24	98-100
Aira/Sakruj ima	Satsuma	Sz-S	5		S (radial)	Plinian Fall	Pum	2	12,800
	Tanzawa*	AT	7.9	463	NE (radial)	Plinian Fall	Pum	5	30,009 ± 189
						Ign. (+Co)	Pum/ash	8	
	Iwato	A-Iw	6.0	9.5	E	Plinian fall; Ign.	Pum/ash	54	~55
Kyushu Central Volcanic Region (CVR)									
Aso Caldera	ACP	ACP3	-	-	E	Plinian Fall	Pum	204	51
	ACP	ACP4	4.6	0.43	E (radial)	Plinian Fall	Pum	205	~51
	ACP	ACP5	4.2	0.15	NE	Plinian Fall	Pum	206	-
	ACP	ACP6	4.6	0.21	E	Plinian Fall	Pum/ ash	207	~60
	Aso-4*	Aso-4	7.7	600		Ign. (+Co)	Pum (Upper)	42	~87-88 ka (MIS5b)
							Pum (middle)	41	
							Pum.(base)	40	
	Aso-Y	Aso-Y	4.0	0.1	E?	Sub-Plinian Fall	Pum	38	
	Aso-A	Aso-A	5.9		ENE	Plinian Fall	Pum	11, 38	
	Aso-B	Aso-B	5.9	1.0	ENE	Sub-Plinian Fall	ash	34	90-100
	Aso-C	Aso-C	5.9		ENE	Plinian Fall	Pum	29, 32	
	Aso-D	Aso-D	5.9		ENE	Plinian Fall	Pum	10, 25	
	Aso-I	Aso-I	5		ENE	Plinian Fall	Pum	242	
	Aso-K	Aso-K	5.0	1.0	ENE	Plinian Fall	Pum	243	> 100 < 123
	Aso-M	Aso-M	5		ENE	Plinian Fall	Pum	244	
	Aso-N	Aso-N	5		ENE	Plinian Fall	Pum	245	
	Aso-3*	Aso-3 Ig. Aso-3-A Aso-3-W	7.4	150	ENE	Ign. (+Co)	Pum/scoria/ ash	254	~123-135
						Ign. (+Co)	Pum/ash	44	
						Plinian Fall	Pum	43	
Kuju (HVZ)	Pumice 1/Handa	Kj-P1/Hd	5.3	2.0	E	Plinian fall, Ign.	Pum	237, 248-250	54.4 ± 1.6
	Kuju-D	Kj-D	-			Plinian fall	Pum	246-247	-
	Miyagi	Kj-Mg	-		S	Ign.	ash	18	>Aso-3

Table 1 (Part 1)

Volcano	Eruption *	Tephra	Magnitude (M)	Volume (km³)	Dispersal	Eruption style	Sampled	Sample Ref. (ITJ)	Age cal yrs BP or Ka (95.4%)
South-West Japan Arc (SWJA)									
Daisen	Kusatanihara Pum.	DKs(P)	5.0		E	Fall, Ign.	Pum		-
	Higashidaisen Pum.	DHg (HgP)	5.6	3.6	E	Plinian Fall	Pum		28,888 ± 92
	Sasaganaru	DSs (Sh)	5.6	3.6	E	Fall, Ign.	Pum	91, 69, 70	29, 837 ± 96
	Kurayoshi Pum.*	DKP	6.5	32	E	Plinian Fall	Pum	68	59.6 ± 5.5
	Sekigane Pum.	DSP	4.9	0.85	E	Plinian Fall	Pum	67	61.1 ± 5.8
Sambe	Taiheizan	Th-pfl	4.4	0.25	E	Ign. (b&a)	Pum	209-210	4036 ± 32
	Shigaku	S2-fl	4.0		E	Ign. (b&a)	Pum	215-217	5501 ± 20
	Midorigaoka	Md-fl			E	Ign.	Pum	234-236	19551 ± 80
	Ukinuno	Uk-pfa(=U2)	5.8	1	ESE	Plinian Fall	Pum	22, 223	-
	Oda	Od-fl(=U1)			ESE	Ign.	Pum	226, 227	-
	Ikeda Pum.	Ik-pfa(SI)	6.0	10	E	Plinian Fall	Pum	71, 228-229	46,295 ± 418
	Ohda pum.	SOd	6.1	13	E	Ign.	Pum	100	
	Unnan pum.	Sun	6.1	13	E	Plinian Fall	Pum	99	53.8 ± 1.2
Izu-Bonin Arc									
Hakone	Hk-TAu8	Hk-TAu8	-	-		Plinian Fall	Pum	255	125-182 ka
North East Japan Arc (NEJA)									
Ontake	**Daiichi Pum.***	On-Pm1	6.7	50	E	Plinian Fall	Pum	80	~95
Towada	Hachinhoe	To-H	6.7	50	E	Plinian Fall + Ign.	Pum	96-97	15706 ± 226 B2k
Shikotsu	**Shikotsu-1***	Spfa-1	7.0	200	SE	Plinian Fall + Ign.	Pum	132	45,105–46,560
Toya	Toya-2*	Toya-2	7.3	170	Radial	Ign.	Pum	81	112-115 (MIS 5d)
Southern Kurile Arc									
Kutcharo	**Shoro (1)***	Kc-Sr	7.2	170	SE	Plinian Fall + Ign.	ash	95	39,265-45,070
	Kc-2/3	Kc-2/3	6.4	25	N-NNE	Ign.	ash/Pum	198-199	
	Kc-Hb/4*	Kc-Hb	7.2	175	W	Plinian Fall + Ign.	pumice	104, 238	
Mashu	Mashu-f	Ma-f	6.0	18.6	ESE	Ign.	Pum/ash	126	7,500-7,620

Table 1 (Part 2)

Sample	Bore hole			Composite depth: Base	Thick-ness	n	Major element glass compositions		n	Trace element glass concentrations (ppm), Ratio (1σ)					SG06 Age		Source Arc	Volcano/proximal unit
(SG06-)	A	B	C	(cm)	(cm)	n	SiO₂	K₂O	n	Rb	Y	Zr	Th	Y/Th	(IntCal13. yrs BP; 95.4%)	Interpolated (ka; 2σ)	Grouping	Albert et al.,(in press); This study
588	A-03-14	B-03-03a		587.8	0.2	25	74.33-77.97	2.25-3.99	13	58-186	3.3-4.3	79-108	9.1-13.0	0.34 ± 0.04	4,036 ± 32		SWJA	Sambe/Th-pd
967	A-06-01	**B-05-04**	C-07-γ	967.2	2.8		72.60-74.60	2.77-3.03	12	68-92	29.7-39.3	160-225	5.6-8.3	4.54 ± 0.50	7,253 ± 46		Kyushu SVZ	Kikai/K-Ah
1965	A-11-00	B-10-02	-	1964.4	0.7	27	76.19-77.43	2.41-3.96	13	64-172	2.8-5.7	48-77	8.8-13.3	0.33 ± 0.07	19,551 ± 80		SWJA	Sambe/Md-fl
2504	A-13-07	B-12-150.8	-	2503.5	0.1	11	74.43-77.74	3.08-3.88	9	79-179	3.8-8.7	82-146	8.5-10.4	0.54 ± 0.19	28,449 ± 78		SWJA	Daisen/DMs
2534	A-13-08	B-13-02	-	2534.3	0.6	25	75.52-76.77	3.04-3.87	14	85-106	3.5-6.5	72-119	8.3-10.4	0.54 ± 0.10	28,888 ± 72		SWJA	Daisen/HgP
2601		B-13-06a		2600.5	0.2	25	72.67-77.91	2.75-4.68	12	64-286	2.8-5.4	78-124	6.8-14.3	0.42 ± 0.06	29,830 ± 96		SWJA	Daisen/DSs (OdA)
2602	-	B-13-06b	-	2601.4	0.4	28	74.14-76.58	2.96-4.16	20	70-146	3.6-4.9	83-128	6.3-10.6	0.45 ± 0.06	29,837 ± 96		SWJA	Daisen/DSs (Sh)
2650	A-14-01	**B-13-Bottom**	-	2650.2	35.1	35	77.02-78.41	3.24-3.55	19	130-160	19.6-22.4	106-122	11.6-13.3	1.67 ± 0.07	30,078 ± 96		Kyushu SVZ	Aira/AT
3485		**B-18-03**		3485.3	0.5	13	51.11-56.43	0.33-0.67	7	7-24	14.6-17.4	39-49	0.4-0.7	31 ± 14	43,713 ± 300		Izu-Bonin	Fuji-Ko/Unknown
3668	A-19-04	B-19-03	-	3668.0	0.3	50	75.54-78.54	2.63-4.89	13	76-198	3.8-9.2	45-65	5.9-14.1	0.67 ± 0.07	46,295 ± 418		SWJA	Sambe/SI
						4	77.62-78.09	3.11-3.49	5	124-477	20.8-36.3	113-131	8.9-12.2	2.56 ± 0.96	46,295 ± 418		Kyushu SVR	Unknown
3912	-	**B-20-α**	-	3911.6	0.1	17	69.64-73.63	4.46-4.90	9	138-194	29.0-44.9	271-353	12.9-18.2	2.41 ± 0.20		50.0 ± 0.2	Kyushu CVR	Aso/ACP4
3974	-	B-20-07	-	3974.0	0.0	23	74.60-78.29	2.70-4.42	9	20-128	1.2-5.5	24-122	2.7-12.5	0.47 ± 0.09		50.9 ± 0.4	SWJA	Daisen/Unknown
4124	-	B-21-03	C-17-06	4123.9	0.2	14	76.33-77.77	3.95-4.59	14	89-118	6.4-8.7	21-27	4.3-6.2	1.58 ± 0.11		53.8 ± 1.2	SWJA	Sambe/Sod
4141	-	B-21-04	-	4141.1	1.3	40	76.87-78.44	3.77-4.24	17	99-142	4.7-8.6	89-121	9.4-13.1	0.62 ± 0.10		54.4 ± 1.6	Kyushu CVR	Kuju/Kj-Hd/P-1 (SAN1)
4281	-	B-22-01	C-18-04	4281.0	0.3	19	73.27-76.69	2.67-2.97	10	66-93	3.8-5.9	74-132	4.2-8.5	0.61 ± 0.18		59.6 ± 5.5	SWJA	Daisen/DKP
4318	A-23-01	**B-22-03**	-	4318.3	1.5	9	45.10-52.18	0.33-0.77	-	-	-	-	-	-		61.1 ± 5.9	SWJA	Daisen/DSP
						29	67.12-72.55	1.99-2.56	12	56-82	6.1-8.6	116-146	5.2-7.3	1.04 ± 0.38		61.1 ± 5.9	SWJA	
4963	A-28-01	**B-28-01**	C-19-03	4962.3	3.5	42	70.06-72.38	4.17-4.82	57	41-199	9.3-36.1	69-321	3.9-18.1	2.05 ± 0.12		**86.4 ± 1.1	Kyushu CVR	Aso/Aso-4
5181	A-29-01	**B-29-04**	-	5180.2	2.4	30	77.76-78.50	3.14-3.40	14	100-130	28.5-34.2	150-179	8.3-10.3	3.35 ± 0.07		94.5 ± 4.8	Kyushu SVR	Kikai/K-Tz
5287	-	-	**C-21-01**	5286.6	4.0	18	69.16-70.31	4.43-5.80	21	129-167	25.7-33.9	217-305	11.3-16.2	2.24 ± 0.17		97.9 ± 6.0	Kyushu CVR	Aso/Aso-A
5353	**A-30-02**	B-30-02	-	5352.3	1.5	26	72.44-74.61	2.64-2.98	12	88-105	34.3-41.2	190-219	7.6-9.6	4.13 ± 0.13		99.3 ± 6.0	Kyushu SVR	Ata/Ata Ignimbrite
6344	**A-37-01**	B-37-02		6364.9	0.8	21	70.12-73.77	0.96-1.13	6	12-16	23.8-31.7	74-98	0.7-0.9	33-38		123.3 ± 7.5	Izu-Bonin	Hakone
6412	**A-37-07**	B-38-03	-	6433.6	0.4	30	69.93-73.27	1.87-2.55	11	50-107	45.4-55.6	201-245	7.7-9.2	6.0 ± 0.6		124.5 ± 7.7	Kyushu SVR	Unknown
6457	A-38-α	**B-38-07**	-	6478.2	0.1	22	74.52-77.45	2.84-5.44	4	75-109	4.9-6.2	70-104	8.4-10.5	0.59 ± 0.05		126.2 ± 8.2	SWJA	DMP?
6634	A-40-02	**B-40-04 a**	-	6655.2	0.1	34	72.77-77.55	2.04-2.67	11	43-88	21.3-40.6	138-267	3.7-7.1	5.77 ± 0.12		130.8 ± 9.2	NEJA	Unknown

Volcano / Arc: Kikai Caldera; Ata Caldera (*Ibuski Volcanic Field*); Aira (+ Sakurajima) — Arc: Kyushu (Kyushu Southern Volcanic Region)

	Akahoya (K-Ah) Takatoge Pass ITJ3 Avg.	±1σ	Akahoya (K-Ah) Doimakino ITJ20 Avg.	±1σ	Tozurahara (K-Tz) Yaku Island ITJ240 Avg.	±1σ	Tozurahara (K-Tz) Tane Island ITJ241 Avg.	±1σ	Ata Fumoto Coast ITJ9 Avg.	±1σ	Ata East of Fumoto ITJ51 Avg.	±1σ	Ata Noga Cave ITJ24 Avg.	±1σ	Ikeda Pumice East of Fumoto ITJ53 Avg.	±1σ	Iwato (A-Iw) Kirishima ITJ54 Avg.	±1σ	AT-Osumi Fall Fumoto Coast ITJ5 Avg.	±1σ	AT-Ito Ign. Fumoto Coast ITJ8 Avg.	±1σ	Sakurajima-S (Sz-S) Takatoge pass ITJ2 Avg.	±1σ
wt.%																								
SiO_2	73.67	1.47	73.93	1.02	78.07	0.18	78.05	0.19	74.29	0.42	74.35	0.27	74.69	0.16	77.73	0.18	77.56	0.19	77.72	0.19	78.01	0.24	75.13	1.34
TiO_2	0.56	0.13	0.55	0.05	0.25	0.03	0.25	0.03	0.49	0.03	0.49	0.04	0.49	0.04	0.16	0.03	0.13	0.03	0.14	0.02	0.13	0.03	0.06	0.01
Al_2O_3	13.58	0.47	13.30	0.24	11.82	0.11	11.71	0.13	13.50	0.18	13.17	0.11	13.06	0.12	12.40	0.11	12.54	0.10	12.62	0.10	12.57	0.13	13.53	0.66
FeOt	2.60	0.48	2.56	0.40	1.07	0.08	1.11	0.07	2.31	0.22	2.16	0.10	2.14	0.09	0.99	0.06	1.02	0.07	1.29	0.08	1.15	0.18	1.87	0.24
MnO	0.09	0.05	0.08	0.05	0.05	0.03	0.05	0.03	0.11	0.04	0.10	0.04	0.10	0.04	0.06	0.04	0.05	0.04	0.05	0.03	0.06	0.04	0.36	0.14
MgO	0.51	0.15	0.51	0.13	0.20	0.03	0.20	0.02	0.44	0.05	0.46	0.02	0.45	0.03	0.15	0.02	0.14	0.02	0.12	0.01	0.12	0.02	0.35	0.08
CaO	2.16	0.45	2.10	0.33	1.10	0.04	1.11	0.02	1.87	0.09	1.89	0.07	1.88	0.05	0.92	0.04	0.99	0.05	1.12	0.04	1.10	0.05	1.83	0.41
Na_2O	4.01	0.14	4.03	0.16	3.93	0.15	3.99	0.19	4.01	0.14	4.25	0.17	4.12	0.24	3.79	0.13	3.55	0.12	3.43	0.13	3.36	0.13	3.72	0.05
K_2O	2.72	0.23	2.71	0.14	3.33	0.10	3.34	0.08	2.91	0.05	2.90	0.06	2.83	0.08	3.56	0.10	3.87	0.08	3.49	0.08	3.49	0.01	3.10	0.25
P_2O_5	0.09	0.04	0.09	0.04	0.02	0.02	0.02	0.02	0.07	0.02	0.06	0.02	0.06	0.02	0.03	0.02	0.02	0.02	0.02	0.02	0.03	0.02	0.05	0.02
Cl	-	-	0.15	0.02	0.16	0.02	0.16	0.01	-	-	0.17	0.03	0.17	0.02	0.20	0.01	0.14	0.03	-	-	-	-	-	-
n	18		27		21		26		12		23		17		15		29		18		15		5	
(ppm)																								
Rb	87.6	15.6	76.1	3.5	102.6	3.9	102.7	6.2	100.6	5.1	90.2	2.5	95.4	2.8	129.1	6.4	152.5	1.4	145.2	4.8	153.5	9.7	-	-
Sr	147	14	141	12	64	4	69	2	124	2	132	5	130	4	66.6	15.9	78.8	15.7	79.4	2.2	78.8	3.5	-	-
Y	35.9	3.8	32.5	1.8	30.8	1.8	31.8	1.4	40.4	1.7	41.5	1.1	40.7	1.4	22.7	0.3	20.2	0.6	21.4	0.9	21.2	1.0	-	-
Zr	221	28	202	10	165	8	171	6	217	4	224	5	218	4	103.1	1.2	95.3	1.9	119.6	4.4	115.9	4.1	-	-
Nb	6.6	1.3	6.4	0.4	5.5	0.5	5.8	0.3	10.1	0.6	10.3	1.2	9.4	0.1	7.2	0.2	7.7	0.0	8.0	0.4	8.4	0.6	-	-
Ba	423	59	436	21	501	18	529	24	444	15	459	32	446	25	494.2	6.8	608.0	15.5	566.2	15.9	572.4	28.4	-	-
La	18.6	2.4	19.0	1.1	18.1	1.0	18.9	0.9	24.3	0.5	24.2	1.4	25.0	0.3	22.1	0.3	26.6	1.4	25.6	0.6	25.5	1.0	-	-
Ce	42.5	5.6	44.6	1.6	40.9	2.1	44.8	2.7	56.4	2.0	54.5	2.4	57.8	1.4	46.6	0.3	50.9	1.4	51.8	2.2	52.7	1.9	-	-
Pr	5.4	0.7	5.4	0.2	4.7	0.2	5.0	0.2	6.5	0.2	6.9	0.5	6.8	0.3	5.1	0.2	5.2	0.2	5.2	0.3	5.2	0.2	-	-
Nd	22.1	3.0	22.0	1.2	17.8	1.2	19.8	1.0	27.5	1.2	27.0	2.0	29.5	0.6	18.8	0.4	18.2	0.7	19.7	2.2	19.0	0.8	-	-
Sm	5.4	0.7	5.1	0.4	4.1	0.3	4.6	0.3	6.6	0.4	6.9	0.5	6.6	0.6	3.5	0.2	3.5	0.2	4.0	0.2	4.0	0.1	-	-
Eu	1.2	0.2	1.1	0.1	0.6	0.1	0.6	0.1	1.4	0.1	1.5	0.3	1.6	0.1	0.5	0.1	0.5	0.0	0.5	0.0	0.5	0.1	-	-
Gd	5.2	0.8	5.1	0.5	4.1	0.5	4.2	0.4	6.4	0.3	6.6	0.2	6.3	0.1	3.1	0.2	3.1	0.1	3.4	0.3	3.5	0.2	-	-
Dy	5.9	0.8	5.5	0.4	4.8	0.4	4.9	0.2	7.3	0.4	7.4	0.5	7.6	0.5	3.4	0.1	3.4	0.0	3.7	0.4	3.7	0.2	-	-
Er	3.9	0.5	3.6	0.2	3.3	0.2	3.6	0.2	4.5	0.2	4.4	0.4	4.6	0.2	2.5	0.1	2.2	0.1	2.4	0.1	2.3	0.2	-	-
Yb	4.1	0.6	3.8	0.3	3.8	0.3	4.2	0.2	4.7	0.2	4.7	0.4	4.7	0.4	2.9	0.1	2.4	0.1	2.7	0.1	2.5	0.2	-	-

Hf	5.8 ± 0.8	5.7 ± 0.4	4.9 ± 0.4	5.4 ± 0.5	6.0 ± 0.3	6.3 ± 0.4	6.5 ± 0.8	3.6 ± 0.2	3.2 ± 0.2	3.8 ± 0.2	3.6 ± 0.3	-
Ta	0.5 ± 0.1	0.4 ± 0.0	0.4 ± 0.0	0.5 ± 0.0	0.7 ± 0.0	0.8 ± 0.2	0.7 ± 0.1	0.6 ± 0.0	0.7 ± 0.0	0.8 ± 0.1	0.8 ± 0.1	-
Th	8.1 ± 1.2	7.6 ± 0.4	9.2 ± 0.6	10.0 ± 0.4	9.2 ± 0.2	9.6 ± 0.6	9.6 ± 0.5	10.6 ± 0.1	13.3 ± 0.5	12.6 ± 0.6	12.5 ± 0.6	-
U	2.1 ± 0.3	2.2 ± 0.1	2.6 ± 0.2	2.8 ± 0.2	2.4 ± 0.1	2.3 ± 0.2	2.6 ± 0.3	2.8 ± 0.1	3.1 ± 0.1	3.1 ± 0.2	3.1 ± 0.2	-
La/Yb	4.6 ± 0.6	5.1 ± 0.2	4.8 ± 0.2	4.5 ± 0.1	5.2 ± 0.2	5.1 ± 0.7	5.2 ± 0.6	7.6 ± 0.4	11.0 ± 0.8	9.6 ± 0.5	10.3 ± 0.7	
Zr/Th	27.2 ± 1.2	26.6 ± 0.6	18.1 ± 0.5	17.2 ± 0.2	23.5 ± 0.6	23.5 ± 1.0	22.7 ± 1.7	9.7 ± 0.2	7.2 ± 0.1	9.5 ± 0.3	9.3 ± 0.4	
Nb/Th	0.8 ± 0.1	0.8 ± 0.1	0.6 ± 0.05	0.6 ± 0.02	1.09 ± 0.07	1.08 ± 0.06	0.98 ± 0.06	0.68 ± 0.02	0.58 ± 0.02	0.64 ± 0.05	0.68 ± 0.07	
n	10	14	14	5	8	3	10	3	4	8	10	

Volcano	Aso Caldera											
Arc	Kyushu (Kyushu Central Volcanic Region)											
Eruption	Aso-3(W)	Aso-3(A)	Aso-3 Ign	Aso-N	Aso-M	Aso-K	Aso-I	Aso-D	Aso-C	Aso-B	Aso-A	Aso-Y
Locality	Noga Cave	Noga Cave	Noga Cave	Noga Cave	Noga Cave	Noga Cave	Noga Cave	Noga Cave	Noga Cave	Noga Cave	Noga Cave	Noga Cave
Sample	ITJ43	ITJ44	ITJ254	ITJ245	ITJ244	ITJ243	ITJ242	ITJ10, ITJ25	ITJ32	ITJ34	ITJ11, ITJ36	ITJ38
wt.% Avg. ± 1σ												
SiO₂	69.92 ± 0.22	70.10 ± 0.51	68.69 ± 2.39	72.81 ± 0.17	68.06 ± 0.32	68.41 ± 0.37	68.2 ± 0.3	69.53 ± 0.29	70.13 ± 0.15	70.06 ± 0.20	69.90 ± 0.26	72.47 ± 0.26
TiO₂	0.60 ± 0.05	0.60 ± 0.07	0.69 ± 0.05	0.27 ± 0.03	0.74 ± 0.04	0.75 ± 0.04	0.7 ± 0.0	0.63 ± 0.04	0.64 ± 0.05	0.63 ± 0.05	0.63 ± 0.05	0.36 ± 0.06
Al₂O₃	15.14 ± 0.10	15.04 ± 0.15	15.34 ± 0.37	13.97 ± 0.15	15.53 ± 0.20	15.62 ± 0.13	15.5 ± 0.1	15.22 ± 0.11	15.00 ± 0.26	15.08 ± 0.11	15.08 ± 0.15	14.75 ± 0.10
FeOt	2.40 ± 0.12	2.39 ± 0.22	2.98 ± 0.99	1.83 ± 0.08	3.04 ± 0.16	2.97 ± 0.10	2.9 ± 0.2	2.49 ± 0.15	2.34 ± 0.09	2.28 ± 0.13	2.30 ± 0.11	1.38 ± 0.14
MnO	0.10 ± 0.05	0.12 ± 0.04	0.12 ± 0.04	0.06 ± 0.02	0.12 ± 0.04	0.11 ± 0.04	0.1 ± 0.0	0.10 ± 0.04	0.11 ± 0.05	0.12 ± 0.04	0.11 ± 0.04	0.11 ± 0.03
MgO	0.56 ± 0.03	0.56 ± 0.09	0.78 ± 0.39	0.16 ± 0.02	0.83 ± 0.06	0.79 ± 0.04	0.8 ± 0.0	0.66 ± 0.04	0.66 ± 0.06	0.61 ± 0.03	0.63 ± 0.03	0.29 ± 0.05
CaO	1.67 ± 0.08	1.64 ± 0.09	2.15 ± 0.85	0.82 ± 0.04	2.20 ± 0.07	2.24 ± 0.20	2.3 ± 0.1	1.95 ± 0.11	1.73 ± 0.09	1.74 ± 0.06	1.80 ± 0.07	0.97 ± 0.08
Na₂O	4.33 ± 0.08	4.31 ± 0.13	4.19 ± 0.19	3.66 ± 0.17	4.46 ± 0.20	4.10 ± 0.18	4.5 ± 0.2	4.65 ± 0.11	4.56 ± 0.08	4.54 ± 0.04	4.66 ± 0.07	4.29 ± 0.02
K₂O	5.05 ± 0.10	5.00 ± 0.12	4.79 ± 0.47	6.23 ± 0.09	4.72 ± 0.11	4.75 ± 0.10	4.6 ± 0.1	4.54 ± 0.10	4.61 ± 0.07	4.70 ± 0.08	4.67 ± 0.10	5.21 ± 0.13
P₂O₅	0.10 ± 0.02	0.11 ± 0.04	0.18 ± 0.13	0.04 ± 0.03	0.18 ± 0.04	0.16 ± 0.03	0.2 ± 0.0	0.13 ± 0.02	-	-	0.11 ± 0.02	0.04 ± 0.01
Cl	0.13 ± 0.02	0.13 ± 0.03	0.11 ± 0.03	0.14 ± 0.01	0.10 ± 0.01	0.10 ± 0.02	0.1 ± 0.0	0.11 ± 0.03	0.12 ± 0.02	0.13 ± 0.02	0.12 ± 0.02	0.13 ± 0.02
n	30	26	27	29	8	21	23	26	9	13	38	12
(ppm)												
Rb	175.5 ± 6.5	181.0 ± 15.4	180.6 ± 11.7	265.0 ± 9.5	177.5 ± 5.8	153.0 ± 8.7	163.7 ± 8.7	174.0 ± 24.5	117.6 ± 12.7	117.0 ± 7.7	165.8 ± 10.6	169.0 ± 2.2
Sr	256.4 ± 44.2	280.3 ± 98.4	297.2 ± 78.8	66.4 ± 22.7	351.0 ± 11.9	283.2 ± 20.7	291.8 ± 16.0	278.1 ± 21.6	166.8 ± 14.4	168.5 ± 6.8	247.2 ± 9.8	152.2 ± 24.7
Y	32.2 ± 0.9	31.5 ± 1.7	33.9 ± 1.6	36.5 ± 0.8	34.3 ± 2.8	32.2 ± 2.9	32.0 ± 1.9	36.6 ± 5.0	22.7 ± 1.2	23.8 ± 1.6	34.6 ± 3.4	33.2 ± 0.4
Zr	292.1 ± 9.5	283.0 ± 10.2	293.6 ± 27.5	402.0 ± 12.2	302.1 ± 19.1	272.4 ± 20.6	279.5 ± 12.4	314.2 ± 43.8	191.6 ± 10.3	193.8 ± 8.6	300.9 ± 18.5	290.5 ± 8.0

	Avg	±1σ	Avg	±1σ	Avg	±1σ	Avg	±1σ	Avg	±1σ	Avg	±1σ	Avg	±1σ	Avg	±1σ	Avg	±1σ	Avg	±1σ	Avg	±1σ	Avg	±1σ
Nb	17.0	0.5	16.9	0.7	17.1	1.4	21.0	0.8	17.8	0.6	16.0	1.0	16.7	1.1	19.2	3.2	11.8	0.3	11.3	1.1	17.2	1.6	15.6	0.3
Ba	840.9	13.4	780.6	59.8	842.7	46.7	387.4	100.3	878.0	32.5	799.7	59.9	798.8	73.5	895.0	96.2	608.2	43.1	609.0	30.8	854.9	54.5	795.4	32.8
La	35.8	0.8	36.5	2.3	36.7	1.9	44.1	0.9	39.4	3.3	33.8	2.0	35.6	2.3	35.9	4.1	23.5	2.0	25.1	1.2	33.4	1.7	34.6	1.0
Ce	78.0	1.9	83.1	20.3	80.7	3.0	94.3	3.7	86.0	4.9	77.2	8.3	77.1	3.2	79.7	9.1	50.8	2.3	54.0	2.5	74.5	4.5	75.7	2.4
Pr	9.0	0.2	9.2	0.5	9.3	0.3	10.3	0.3	9.8	0.5	8.7	0.5	8.9	0.5	9.3	1.2	6.1	0.5	6.5	0.5	8.4	0.6	8.8	0.3
Nd	36.1	1.0	36.6	2.1	38.1	1.7	40.6	1.0	40.7	3.6	36.7	3.1	37.2	2.4	38.0	4.5	25.2	1.1	25.4	1.8	35.1	3.0	35.0	1.2
Sm	7.6	0.3	7.6	0.4	8.0	0.5	8.3	0.4	8.2	0.7	8.1	1.3	7.7	0.7	7.9	1.2	5.1	0.3	5.4	0.7	7.2	0.8	7.4	0.2
Eu	1.5	0.1	1.5	0.2	1.6	0.1	0.8	0.1	1.7	0.1	1.5	0.1	1.5	0.2	1.7	0.2	1.1	0.1	1.1	0.1	1.5	0.1	1.3	0.1
Gd	6.0	0.3	6.2	0.4	6.7	0.3	6.7	0.3	6.9	0.6	6.1	0.4	6.2	0.6	6.9	1.0	4.2	0.3	4.5	0.4	6.5	0.7	5.8	0.2
Dy	5.7	0.2	5.8	0.3	6.1	0.3	6.3	0.3	6.7	0.5	5.6	0.5	6.0	0.4	6.5	1.0	3.9	0.3	4.4	0.4	6.1	0.6	5.7	0.2
Er	3.5	0.1	3.3	0.2	3.7	0.2	3.9	0.1	3.7	0.5	3.5	0.3	3.5	0.4	3.9	0.6	2.4	0.2	2.6	0.2	3.7	0.4	3.6	0.1
Yb	3.6	0.1	3.5	0.2	3.7	0.3	4.3	0.2	4.1	0.5	3.7	0.5	3.8	0.1	4.2	0.6	2.8	0.3	2.9	0.2	4.0	0.4	3.9	0.1
Hf	7.8	0.3	7.4	0.4	7.4	0.7	10.6	0.4	7.5	0.3	7.3	0.6	7.5	0.6	8.0	1.0	4.9	0.5	5.6	0.5	7.6	0.6	7.8	0.3
Ta	1.2	0.0	1.2	0.0	1.2	0.1	1.7	0.1	1.3	0.1	1.2	0.1	1.2	0.1	1.2	0.2	0.9	0.1	0.9	0.1	1.2	0.1	1.2	0.0
Th	16.1	0.5	15.0	0.9	15.9	1.5	27.1	0.7	16.8	1.2	15.6	0.9	15.5	0.6	16.2	2.1	10.7	0.4	11.4	0.9	15.1	0.8	15.9	0.7
U	4.8	0.2	4.8	0.1	4.8	0.4	8.0	0.3	5.5	0.9	4.4	0.1	4.9	0.2	5.0	0.6	3.5	0.5	3.3	0.2	4.6	0.4	4.8	0.2
La/Yb	9.9	0.2	10.5	0.4	9.9	0.7	10.2	0.4	5.3	6.9	5.7	4.1	5.5	1.2	8.6	0.7	8.6	1.0	8.7	0.8	8.5	0.8	8.9	0.3
Zr/Th	18.1	0.2	19.0	1.0	18.5	0.8	14.8	0.5	7.6	10.2	8.3	6.0	8.0	1.7	19.4	1.0	17.9	0.9	17.0	1.1	19.9	1.0	18.2	0.3
Nb/Th	1.05	0.01	1.14	0.09	1.08	0.09	0.77	0.04	0.41	0.52	0.43	0.31	0.42	0.09	1.18	0.04	1.10	0.04	0.99	0.07	1.14	0.01	0.98	0.03
n	6		6		16		10		4		7		6		11		8		12		16		6	

Volcano: Aso (ITJ40, ITJ142 ×3) · Aso Central Pumice Cone (ACP) · Kuju (Hohi Volcanic Zone)
Arc: Kyushu (Kyushu Central Volcanic Region)

wt.%	Aso-4 Noga Cave ITJ40 (Comp.1) Avg.	±1σ	Aso-4 Noga Cave ITJ142 (Comp.1?) Avg.	±1σ	Aso-4 Noga Cave ITJ142 (Comp.2) Avg.	±1σ	Aso-4 Noga Cave ITJ142 (Comp.3) Avg.	±1σ	ACP 6 Mizunomoto ITJ207 Avg.	±1σ	ACP 5 Namino ITJ206 Avg.	±1σ	ACP 4 Mizunomoto ITJ205 Avg.	±1σ	ACP 3 Mizunomoto ITJ204 Avg.	±1σ	Kj-Mg NE Aso C. Rim ITJ18 Avg.	±1σ	Kj-D Tanbara ITJ246/7 Avg.	±1σ	Kj-Hd Yumiori ITJ237 Avg.	±1σ	Kj-P1 Yumiori ITJ237 Avg.	±1σ
SiO₂	72.17	0.39	72.32	0.26	71.18	0.35	67.16	0.48	70.10	0.64	70.16	0.27	71.70	0.21	74.03	0.43	77.40	0.38	77.40	0.62	77.56	0.30	78.02	0.35
TiO₂	0.41	0.05	0.43	0.03	0.45	0.03	0.61	0.06	0.62	0.06	0.59	0.08	0.47	0.04	0.33	0.05	0.18	0.04	0.21	0.05	0.20	0.03	0.18	0.04
Al₂O₃	14.78	0.12	14.95	0.14	15.48	0.18	16.52	0.24	15.09	0.21	15.10	0.19	14.85	0.12	13.95	0.10	12.59	0.11	12.59	0.11	12.52	0.16	12.43	0.17
FeOt	1.59	0.26	1.50	0.09	1.74	0.00	3.09	0.37	2.33	0.27	2.49	0.04	1.74	0.01	1.24	0.01	0.91	0.01	0.95	0.05	1.03	0.00	0.79	0.05
MnO	0.10	0.05	0.13	0.03	0.12	0.03	0.16	0.04	0.11	0.05	0.13	0.04	0.11	0.05	0.05	0.04	0.06	0.05	0.07	0.04	0.05	0.03	0.05	0.05
MgO	0.34	0.06	0.38	0.03	0.48	0.04	1.05	0.12	0.64	0.10	0.62	0.09	0.40	0.04	0.20	0.04	0.25	0.07	0.21	0.07	0.22	0.03	0.21	0.02
CaO	1.08	0.06	1.11	0.05	1.47	0.09	2.90	0.19	1.90	0.23	1.75	0.02	1.27	0.07	0.70	0.08	1.23	0.05	1.15	0.08	1.28	0.09	1.17	0.07

(Top rows of the major-element section are cut off at the page top; transcription begins at Na₂O.)

Major elements (wt.%) and trace elements (ppm). Each sample is reported as Avg. and ±1σ. Twelve data columns are present; the footer (below) labels nine samples.

	1 Avg	1 ±1σ	2 Avg	2 ±1σ	3 Avg	3 ±1σ	4 Avg	4 ±1σ	5 Avg	5 ±1σ	6 Avg	6 ±1σ	7 Avg	7 ±1σ	8 Avg	8 ±1σ	9 Avg	9 ±1σ	10 Avg	10 ±1σ	11 Avg	11 ±1σ	12 Avg	12 ±1σ
Na_2O	4.56	0.14	4.45	0.16	4.47	0.32	4.72	0.28	4.64	0.15	4.38	0.13	4.66	0.13	4.19	0.25	3.40	0.14	3.25	0.16	2.87	0.30	2.89	0.18
K_2O	4.78	0.10	4.51	0.03	4.39	0.08	3.47	0.18	4.34	0.18	4.55	0.12	4.62	0.08	5.15	0.11	3.78	0.09	3.98	0.13	4.05	0.07	4.05	0.09
P_2O_5	0.07	0.03	0.08	0.03	0.09	0.02	0.23	0.04	0.12	0.03	0.10	0.04	0.06	0.02	0.03	0.02	0.02	0.02	0.03	0.03	0.03	0.02	0.04	0.02
Cl	0.13	0.02	0.14	0.01	0.14	0.02	0.10	0.02	0.11	0.01	0.12	0.03	0.13	0.02	0.13	0.02	0.19	0.03	0.15	0.05	0.17	0.02	0.17	0.03
n	11		5		21		14		16		7		25		25		15		6		26		15	
(ppm)																								
Rb	151.3	11.3	142.5	15.2	150.7	10.9	109.9	7.8	154.8	-	-	-	150.3	6.9	173.5	2.4	109.1	-	-	-	126.1	-	116.3	-
Sr	151.3	16.1	174.4	16.8	240.5	26.2	493.2	53.2	228.0	-	-	-	149.7	10.9	58.7	8.5	190.1	-	-	-	230.0	-	205.3	-
Y	29.2	2.6	22.6	2.9	27.3	1.8	29.1	1.9	31.9	-	-	-	33.7	2.1	31.3	6.4	7.2	-	-	-	8.0	-	6.7	-
Zr	259.7	20.8	205.2	26.4	241.7	18.7	183.5	12.5	271.0	-	-	-	285.6	15.6	261.2	42.8	90.9	-	-	-	123.3	-	93.4	-
Nb	15.2	0.9	12.9	1.6	14.5	1.4	11.5	0.7	15.3	-	-	-	16.4	1.2	16.2	0.8	9.9	-	-	-	13.4	-	11.6	-
Ba	786.1	32.0	672.6	87.5	823.1	76.3	713.8	47.3	774.4	-	-	-	800	46	705	70	904	-	-	-	1053.0	-	918	-
La	31.8	2.7	26.2	3.1	32.4	2.6	30.9	2.1	30.9	-	-	-	31.5	1.8	30.1	5.1	21.5	-	-	-	28.5	-	23.9	-
Ce	73.2	5.3	59.8	5.4	69.3	4.6	67.8	3.4	67.5	-	-	-	66.6	4.9	67.1	8.8	39.5	-	-	-	45.9	-	40.1	-
Pr	8.2	0.6	6.9	0.6	8.0	0.4	8.1	0.5	7.9	-	-	-	8.1	0.5	7.6	1.2	3.6	-	-	-	4.3	-	3.7	-
Nd	31.7	2.7	26.1	3.0	30.4	2.5	33.9	1.9	31.9	-	-	-	33.5	2.4	30.4	4.9	11.0	-	-	-	13.5	-	11.6	-
Sm	6.8	0.8	5.4	0.2	6.0	0.5	7.1	0.4	6.9	-	-	-	7.0	0.5	6.5	0.8	1.7	-	-	-	1.3	-	1.8	-
Eu	1.3	0.2	1.2	0.1	1.3	0.1	1.9	0.1	1.4	-	-	-	1.3	0.1	1.0	0.1	0.4	-	-	-	1.0	-	0.4	-
Gd	5.4	0.7	5.1	0.9	5.5	0.6	6.4	0.6	5.9	-	-	-	5.8	0.5	5.5	0.6	1.5	-	-	-	1.4	-	1.5	-
Dy	5.1	0.7	4.3	0.6	4.9	0.6	5.4	0.4	5.5	-	-	-	5.8	0.4	5.5	0.9	1.1	-	-	-	1.6	-	1.1	-
Er	3.2	0.2	2.4	0.1	3.0	0.3	3.1	0.2	3.4	-	-	-	3.6	0.3	3.5	0.5	0.7	-	-	-	0.9	-	0.8	-
Yb	3.5	0.4	2.8	0.4	3.4	0.3	3.3	0.2	3.7	-	-	-	3.9	0.3	4.0	0.3	1.1	-	-	-	1.2	-	1.0	-
Hf	6.9	0.5	5.5	0.9	6.7	0.6	5.3	0.5	7.2	-	-	-	7.4	0.5	7.1	1.3	2.9	-	-	-	3.7	-	3.2	-
Ta	1.0	0.1	0.8	0.1	1.0	0.0	0.8	0.1	1.1	-	-	-	1.1	0.1	1.1	0.2	0.9	-	-	-	1.2	-	1.1	-
Th	14.6	1.3	11.3	1.4	13.7	0.8	10.2	0.7	13.7	-	-	-	13.3	1.2	14.0	3.3	10.4	-	-	-	14.0	-	12.4	-
U	4.6	0.4	3.9	0.5	4.4	0.3	3.1	0.2	4.1	-	-	-	3.9	0.3	4.3	0.5	2.5	-	-	-	3.5	-	2.7	-
La/Yb	9.1	0.5	9.8	0.9	9.6	0.6	9.4	0.3	8.5	-	-	-	8.2	0.3	7.6	0.8	20.3	-	-	-	23.0	-	23.6	-
Zr/Th	17.8	0.6	18.2	1.0	17.7	0.7	18.0	0.4	19.8	-	-	-	21.6	1.3	19.2	2.6	8.7	-	-	-	8.8	-	7.5	-
Nb/Th	1.04	0.06	1.15	0.14	1.06	0.08	1.14	0.06	1.13	-	-	-	1.25	0.13	1.22	0.29	0.95	-	-	-	0.95	-	0.93	-
n	6		5		5		10		1				14		8		1				1		1	

Volcano	Hakone	Ontake	Towada	Shikotsu	Toya	Kutcharo			Mashu
Arc	Izu-Bonin	NEJA (Norikura)	NEJA	NEJA	NEJA	Southern Kurile Arc			
Eruption	Hk-TAu8	On-Pm1	To-H	Spfa-1	Toya	Kc-Hb	Kc-2/3	Kc-Sr	Mashu-f
Locality		Omachi	Mitateyama	MIsawa	Narugo	Raiun		Shoro	Naka-shunbetsu
Sample	ITJ255	ITJ79	ITJ96	ITJ132	ITJ81	ITJ238	ITJ198	ITJ95	ITJ126
wt.%	Avg. ±1σ	Avg. ±1σ	Avg. ±1σ	Avg. ±1σ	Avg. ±1σ	Avg. ±1σ	Avg. ±1σ	Avg. ±1σ	Avg. ±1σ

SiO$_2$	73.05	*1.54*	75.28	0.45	71.70	0.21	77.44	0.18	78.08	0.15	77.73	0.16	76.18	1.15	77.48	0.39	71.70	0.98
TiO$_2$	0.67	*0.14*	0.08	0.03	0.47	0.04	0.16	0.03	0.04	0.03	0.35	0.04	0.38	0.08	0.30	0.03	0.67	0.05
Al$_2$O$_3$	12.83	*0.29*	13.91	0.37	14.85	0.12	12.52	0.07	12.67	0.10	12.04	0.10	12.67	0.41	12.34	0.30	14.02	0.47
FeOt	3.63	*0.64*	1.13	0.15	1.74	0.11	1.51	0.08	0.95	0.06	1.58	0.08	1.88	0.35	1.43	0.09	3.47	0.34
MnO	0.11	*0.04*	0.16	0.04	0.11	0.05	0.07	0.05	0.09	0.03	0.10	0.06	0.11	0.05	0.08	0.04	0.18	0.04
MgO	0.81	*0.20*	0.24	0.02	0.40	0.04	0.16	0.02	0.04	0.02	0.29	0.02	0.39	0.11	0.29	0.03	0.94	0.28
CaO	3.10	*0.55*	1.54	0.11	1.27	0.07	1.47	0.05	0.37	0.03	1.39	0.05	1.81	0.29	1.65	0.11	3.76	0.35
Na$_2$O	4.36	*0.15*	3.91	0.16	4.66	0.13	3.91	0.13	4.86	0.10	4.34	0.15	4.49	0.15	3.97	0.16	4.25	0.15
K$_2$O	1.13	*0.13*	3.53	0.09	4.62	0.08	2.58	0.06	2.74	0.14	1.95	0.06	1.87	0.10	2.19	0.05	0.72	0.06
P$_2$O$_5$	0.15	*0.04*	0.04	0.02	0.06	0.02	0.02	0.02	0.02	0.02	0.04	0.03	0.05	0.02	0.03	0.02	0.17	0.05
Cl	0.15	*0.03*	0.17	0.04	0.13	0.02	0.17	0.02	0.14	0.02	0.18	0.02	0.17	0.04	0.26	0.04	0.11	0.02
n	*13*		*9*		*19*		*20*		*16*		*27*		*22*		*23*		*13*	
(ppm)																		
Rb	18.1	3.9	102.8	62.8	27.5	3.6	69.6	1.85	61.0	2.0	42.6	0.6	41.4	2.0	51.3	3.7	11.6	0.7
Sr	247.6	97.3	121.8	98.4	201.6	41.9	126.7	5.63	22.8	3.0	123	9	167	33	124	15	213	23
Y	33.8	5.1	13.2	10.8	35.4	3.1	36.0	0.70	53.9	3.9	42.4	4.3	42.3	0.5	28.8	3.6	37.0	3.4
Zr	112.6	14.8	129.5	82.8	127.9	8.4	143.8	2.65	80.5	5.8	151.0	13.3	154.3	5.9	165.0	10.7	84.5	6.8
Nb	1.9	0.4	10.1	5.9	5.0	0.5	6.8	0.08	5.6	0.6	2.6	0.1	2.7	0.1	3.2	0.4	0.9	0.1
Ba	416.7	101.7	683	389	401.6	46.7	741	8	883	78	552	34	578	21	649	49	275	22
La	6.5	1.2	21.3	10.0	12.5	1.4	16.1	0.39	14.3	0.5	13.6	1.1	14.6	0.3	13.9	1.1	6.3	0.5
Ce	17.4	4.0	40.3	20.9	30.3	3.1	37.1	0.72	39.0	2.2	33.0	2.3	35.2	0.5	33.9	2.6	17.1	1.3
Pr	2.6	0.6	4.2	2.3	3.8	0.3	4.6	0.09	4.7	0.3	4.3	0.3	4.5	0.1	4.0	0.3	2.5	0.2
Nd	14.2	3.2	14.9	9.6	18.2	1.5	19.9	0.28	21.1	0.7	20.3	1.8	21.1	0.6	16.2	1.8	13.3	1.3
Sm	4.4	0.7	-	-	5.1	1.2	5.1	0.14	6.5	0.4	5.5	0.5	5.7	0.2	5.0	0.7	4.2	0.5
Eu	1.2	0.1	-	-	1.2	0.1	0.9	0.04	0.6	0.1	1.3	0.1	1.4	0.1	1.0	0.1	1.3	0.1
Gd	5.0	1.1	2.3	1.9	5.2	0.6	5.1	0.16	7.1	0.6	5.9	0.5	6.0	0.2	4.6	0.7	5.1	0.5
Dy	6.0	1.1	0.4	1.9	6.0	0.8	6.0	0.18	9.0	0.7	7.2	0.6	7.2	0.2	4.7	0.7	6.4	0.7
Er	3.8	0.6	0.2	1.2	3.9	0.6	3.9	0.10	5.7	0.6	4.8	0.5	4.7	0.1	3.4	0.5	4.1	0.4
Yb	4.0	0.6	1.7	1.4	4.2	0.2	4.2	0.14	6.1	0.7	5.2	0.4	5.1	0.2	3.8	0.4	4.4	0.4
Hf	3.5	0.4	3.8	2.1	3.8	0.0	4.4	0.16	3.5	0.2	4.4	0.4	4.6	0.2	4.7	0.3	2.7	0.2
Ta	0.2	0.0	0.9	0.4	0.3	0.0	0.5	0.01	0.4	0.0	0.2	0.0	0.2	0.0	0.3	0.1	0.1	0.0
Th	1.0	0.2	10.4	4.5	3.2	0.3	6.3	0.15	5.8	0.2	4.3	0.5	4.6	0.1	5.6	0.3	1.1	0.1
U	0.6	0.1	2.7	1.4	0.9	0.3	2.0	0.05	2.2	0.2	1.4	0.1	1.5	0.1	2.0	0.2	0.4	0.0
La/Yb	1.6	0.2	19.4	2.4	3.01	0.05	3.9	0.1	2.4	0.2	2.6	0.1	2.9	0.1	3.6	0.4	1.4	0.1
Zr/Th	121.3	19.4	12.7	0.6	40.06	2.92	22.9	0.3	14.0	0.9	35.0	1.1	33.5	0.7	29.7	1.9	76.1	2.6
Nb/Th	2.04	0.09	0.9	0.1	1.56	0.19	1.08	0.03	0.97	0.09	0.6	0.0	0.58	0.03	0.59	0.08	0.85	0.04
n	*7*		*8*		*12*		*12*		*8*		*7*		*6*		*15*		*8*	

Table 3

Tephra	SG06-0967*		SG06-2650*		SG06-3485*		SG06-3668 (C2)		SG06-3912*		SG06-4963 (C1)*		SG06-4963 (C2)*		SG06-5181*		SG06-5287*		SG06-5553*		SG06-6344*		SG06-6313		SG06-6634*	
Event Layer	A-06-01		B-13 Bottom		B-18-03		B-19-03		B-20-α																	
wt.%	Avg.	±1σ	Avg.	±1σ	Avg.	±1σ	Avg.	±1σ	Avg.	±1σ	Avg.	±1σ	Avg.	±1σ	Avg.	±1σ	Avg.	±1σ	Avg.	±1σ	Avg.	±1σ	Avg.	±1σ	Avg.	±1σ
SiO$_2$	74.09	0.49	77.64	0.31	53.83	0.63	77.87	0.16	71.51	0.53	71.94	0.23	70.88	0.36	78.06	0.18	69.57	0.20	74.06	0.41	71.33	1.50	72.18	0.87	76.07	1.38
TiO$_2$	0.54	0.03	0.14	0.03	1.32	0.19	0.13	0.03	0.49	0.05	0.42	0.03	0.48	0.03	0.25	0.03	0.60	0.03	0.50	0.03	0.75	0.11	0.49	0.03	0.39	0.09
Al$_2$O$_3$	13.17	0.17	12.41	0.15	17.01	1.49	12.31	0.12	14.90	0.26	14.92	0.14	15.45	0.17	11.91	0.07	15.40	0.12	13.25	0.29	13.87	0.96	13.96	0.27	12.60	0.50
FeOT	2.51	0.16	1.27	0.09	10.13	1.1	1.28	0.08	1.88	0.20	1.54	0.14	1.79	0.09	1.08	0.07	2.37	0.13	2.17	0.10	3.75	0.57	3.45	0.30	1.87	0.36
MnO	0.09	0.04	0.06	0.04	0.17	0.07	0.03	0.02	0.08	0.05	0.10	0.05	0.13	0.06	0.04	0.03	0.11	0.04	0.10	0.03	0.14	0.04	0.10	0.04	0.05	0.04
MgO	0.48	0.05	0.13	0.02	4.73	0.76	0.14	0.01	0.41	0.08	0.35	0.03	0.49	0.04	0.20	0.02	0.62	0.03	0.44	0.02	0.77	0.18	0.49	0.00	0.40	0.02
CaO	1.99	0.11	1.12	0.04	9.37	0.50	1.13	0.06	1.32	0.13	1.08	0.04	1.43	0.09	1.08	0.04	1.81	0.06	1.92	0.18	3.40	0.58	2.65	0.24	1.87	0.39
Na$_2$O	4.02	0.17	3.68	0.27	2.69	0.24	3.70	0.21	4.62	0.26	4.82	0.15	4.75	0.17	3.93	0.13	4.73	0.16	4.47	0.20	4.67	0.20	4.47	0.22	4.09	0.17
K$_2$O	2.89	0.07	3.39	0.08	0.48	0.09	3.35	0.13	4.59	0.14	4.63	0.12	4.37	0.12	3.28	0.07	4.55	0.09	2.87	0.07	1.01	0.08	2.14	0.08	2.41	0.18
P$_2$O$_5$	0.07	0.02	0.03	0.02	0.20	0.03	0.02	0.01	0.08	0.04	0.06	0.02	0.09	0.02	0.02	0.02	0.11	0.02	0.06	0.01	0.17	0.03	0.08	0.02	0.04	0.03
Cl	0.14	0.01	0.12	0.01	0.07	0.02	0.11	0.00	0.12	0.01	0.14	0.02	0.15	0.03	0.15	0.02	0.12	0.01	0.14	0.02	0.14	0.03	0.16	0.02	0.21	0.03
n							7								18.0		26		20		30					
(ppm)																										
Rb	84.7	6.1	147.7	7.8	11.7	6.0	232.9	152.8	165.6	16.8	172.1	14.7	137.2	17.9	105.9	6.7	152.7	9.8	97.7	3.6	15.1	1.6	76.6	22.1	60.8	14.2
Sr	136	4	79	2	345.2	43.2	81	8	167	13	164	11	247	59	65	6	236	31	130	8	232	59	163	69	123	16
Y	34.1	2.7	20.5	0.6	15.6	1.4	27.4	7.0	37.1	4.4	32.3	2.1	25.9	3.2	30.9	1.8	30.7	2.5	38.3	1.9	28.8	2.9	39.1	8.0	30.1	7.1
Zr	208	17	113	4	45.4	4.1	120	7	296	25	288	16	228	27	165	9	260	25	205	9	90.0	9.3	179.1	38.3	193.4	43.8
Nb	6.6	0.6	8.1	0.5	1.3	0.5	11.0	4.7	17.5	2.9	16.0	1.2	12.7	1.7	5.9	0.6	14.3	1.5	9.5	0.5	1.7	0.2	6.8	1.5	6.6	2.0
Ba	442	29	566	18	162.0	21.0	790	348	828	85	859	56	741	127	509	29	783	86	458	27	376	28	310	65	486	113
La	18.8	1.2	24.9	0.8	4.2	0.9	22.4	5.3	32.9	3.2	34.0	2.2	29.0	3.8	18.2	0.9	31.7	3.3	24.0	1.3	5.7	0.4	19.0	3.5	14.1	3.1
Ce	44.1	2.7	53.3	1.9	11.2	2.1	48.2	8.8	76.4	7.6	77.0	5.3	63.8	7.7	41.2	2.7	68.0	5.5	58.0	3.9	15.4	1.3	42.5	7.7	32.2	7.2
Pr	5.1	0.4	5.2	0.2	1.7	0.2	5.0	0.7	8.6	0.7	8.9	0.6	7.4	0.9	4.7	0.2	8.0	0.7	6.3	0.4	2.3	0.2	5.2	1.0	4.1	0.8
Nd	21.3	1.2	19.0	0.9	8.5	1.2	21.8	2.5	36.1	3.9	34.7	2.3	29.4	4.2	18.5	1.3	32.5	3.7	27.5	1.4	12.3	0.9	22.4	3.8	17.5	4.0
Sm	5.2	0.5	3.8	0.2	2.5	0.4	4.2	0.6	7.9	1.3	7.0	0.6	5.9	0.8	4.3	0.4	6.9	0.6	6.2	0.5	3.8	0.4	5.5	1.1	5.6	1.8
Eu	1.1	0.1	0.5	0.0	0.9	0.1	0.9	0.4	1.5	0.2	1.3	0.1	1.2	0.2	0.6	0.1	1.3	0.1	1.3	0.1	1.1	0.1	1.3	0.2	0.9	0.3
Gd	4.9	0.5	3.4	0.2	2.9	0.4	4.3	1.1	6.4	0.9	5.9	0.5	4.8	0.7	4.2	0.4	5.6	0.4	6.2	0.7	4.2	0.3	5.6	1.1	4.5	1.3

|																									
Dy	5.8	0.5	3.5	0.2	2.9	0.3	4.7	1.3	6.3	0.7	5.6	0.5	4.6	0.7	4.7	0.3	5.3	0.4	6.7	0.5	5.1	0.5	6.6	1.4	5.2 1.1
Er	3.7	0.4	2.3	0.2	1.6	0.2	2.8	0.6	4.0	0.6	3.5	0.3	2.8	0.3	3.5	0.4	3.1	0.4	4.4	0.4	3.2	0.4	4.4	1.0	3.2 0.6
Yb	3.9	0.4	2.5	0.2	1.7	0.3	3.0	0.4	4.2	0.6	3.8	0.3	3.0	0.5	3.9	0.3	3.3	0.4	4.7	0.4	3.3	0.3	4.6	1.2	3.5 0.9
Hf	5.8	0.6	3.5	0.2	1.4	0.2	3.3	0.3	7.9	1.0	7.7	0.7	6.1	0.8	4.9	0.4	6.1	0.6	5.6	0.4	2.8	0.3	5.0	1.3	5.3 1.2
Ta	0.5	0.0	0.7	0.0	0.1	0.0	0.9	0.2	1.3	0.2	1.2	0.1	0.9	0.2	0.5	0.1	1.0	0.1	0.7	0.1	0.1	0.0	0.5	0.1	0.5 0.1
Th	7.6	0.7	12.3	0.5	0.6	0.2	11.1	1.4	14.7	1.1	16.1	1.1	12.7	1.6	9.2	0.6	13.8	1.3	8.9	0.6	0.8	0.1	6.6	1.5	5.2 1.4
U	2.1	0.2	3.1	0.2	0.4	0.1	4.5	2.1	4.7	0.5	5.0	0.5	4.0	0.5	2.7	0.3	4.1	0.6	2.4	0.2	0.5	0.0	1.7	0.4	1.7 0.4
La/Yb	4.9	0.4	10.1	0.9	2.7	0.9	7.8	2.6	8.3	1.5	9.0	0.4	9.6	0.8	4.6	0.2	9.3	0.8	5.2	0.4	1.76	0.05	4.2	0.4	4.1 0.5
Zr/Th	27.6	1.6	9.2	0.3	78.9	21.0	11.0	2.0	20.4	1.0	17.9	0.6	18.0	0.8	17.9	1.0	18.9	1.2	23.2	0.8	110.3	4.9	27.4	1.2	37.4 2.1
Nb/Th	0.87	0.09	0.66	0.05	1.79	0.30	1.04	0.54	1.22	0.13	1.00	0.06	1.00	0.07	0.64	0.05	1.05	0.12	1.08	0.10	2.08	0.03	1.04	0.08	1.28 0.23
n	*12*		19		13		5		9		33		16		14		21		12		6		5		11

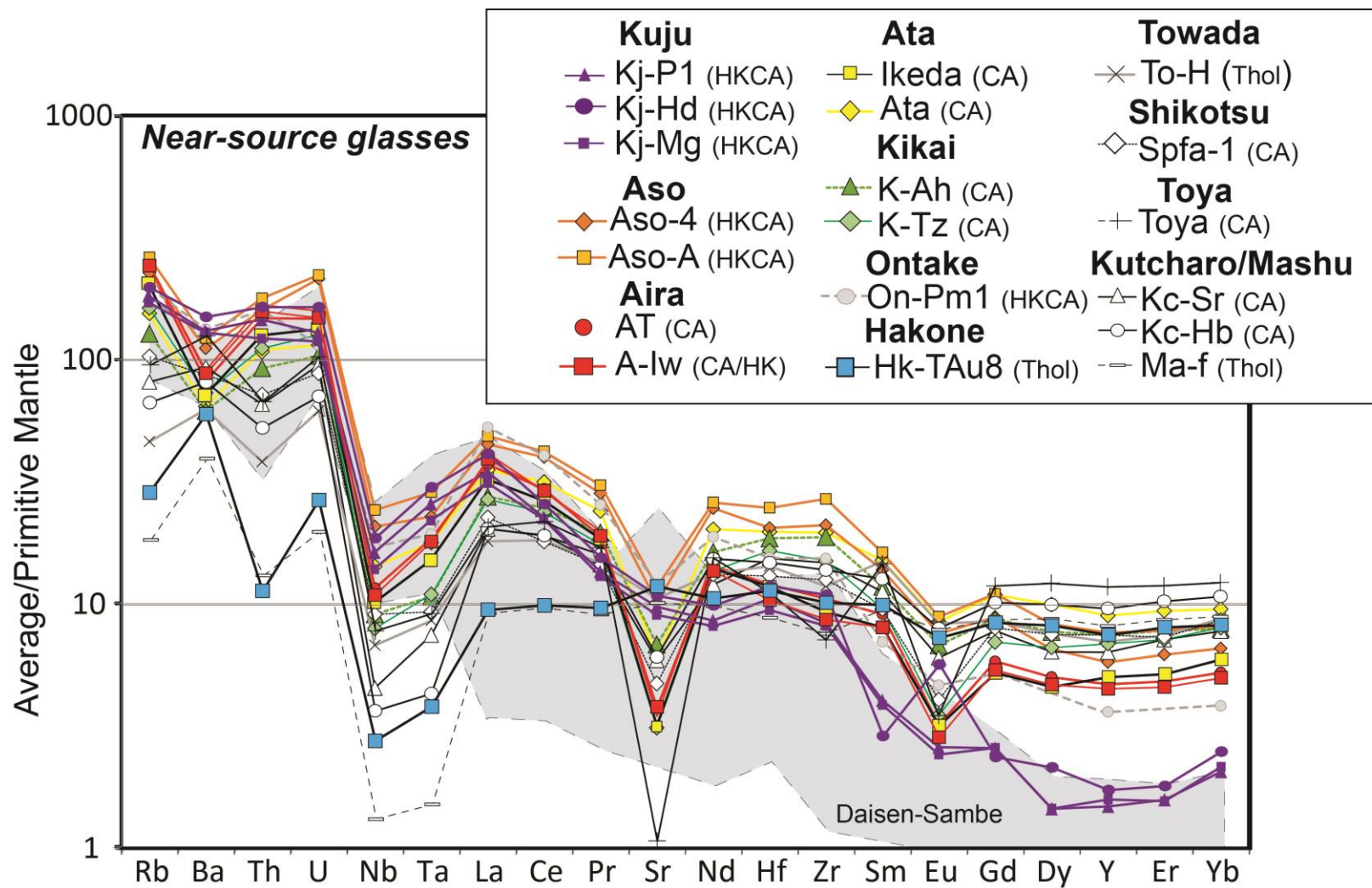**Table 4**
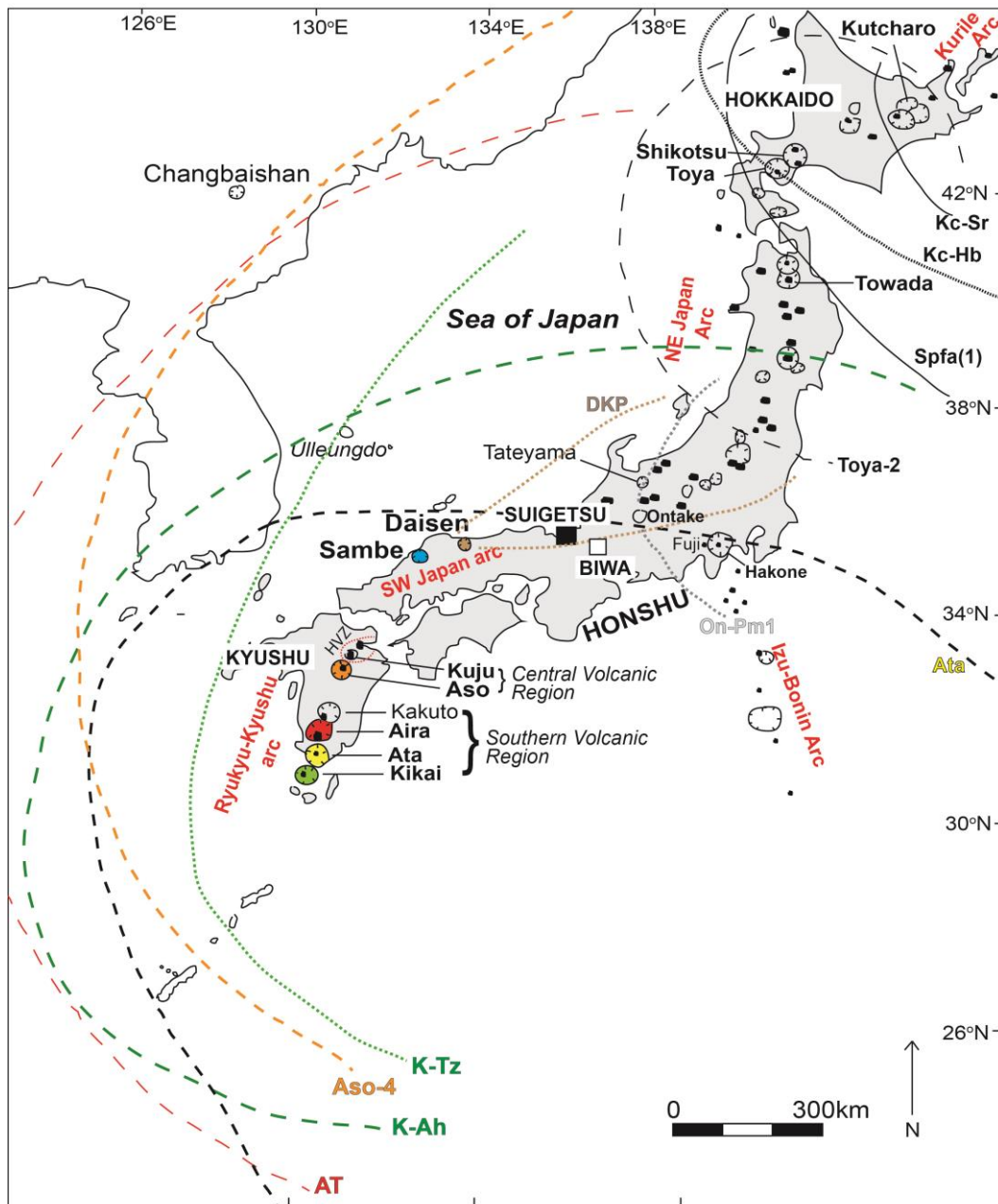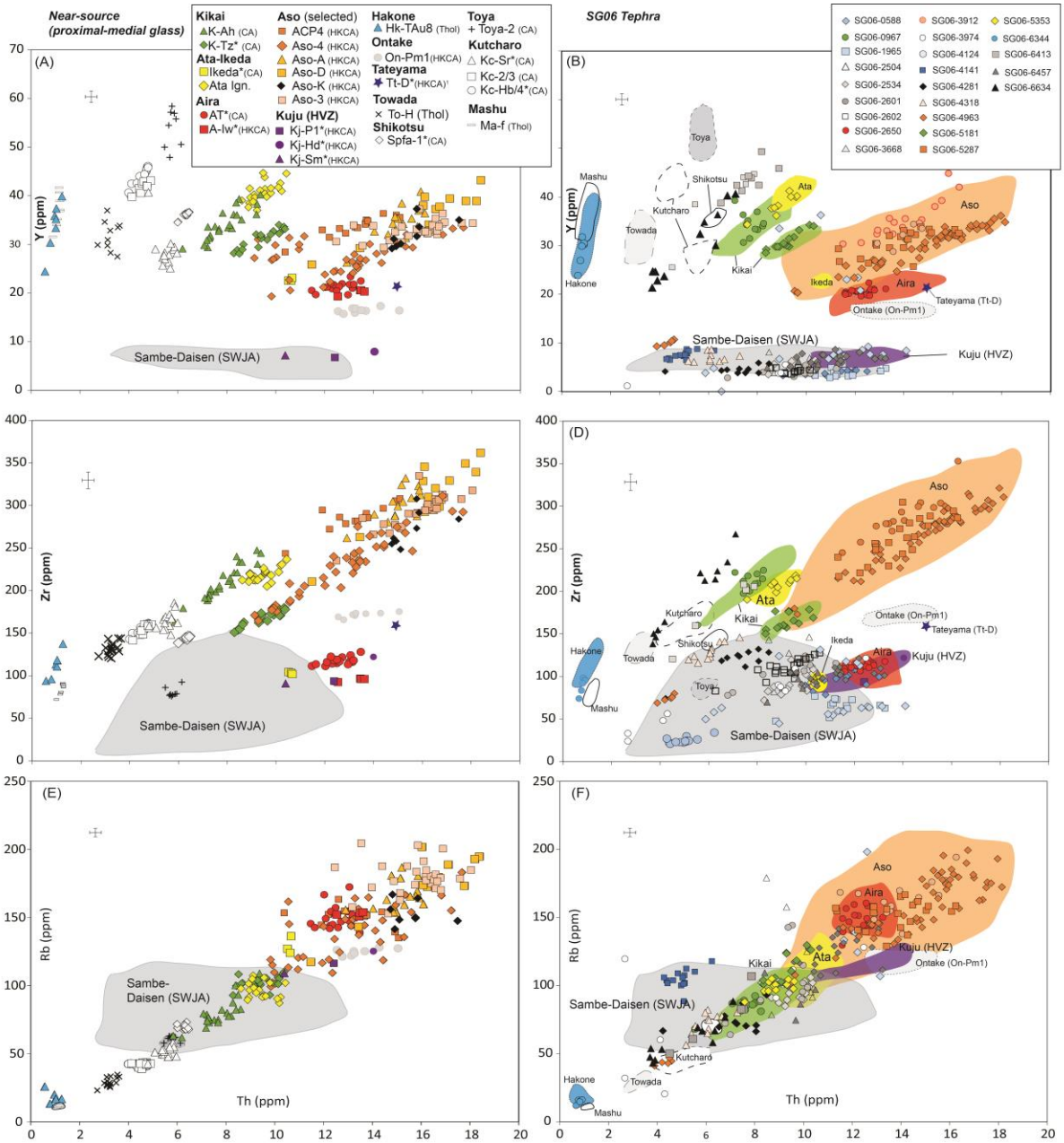
Figure 1.
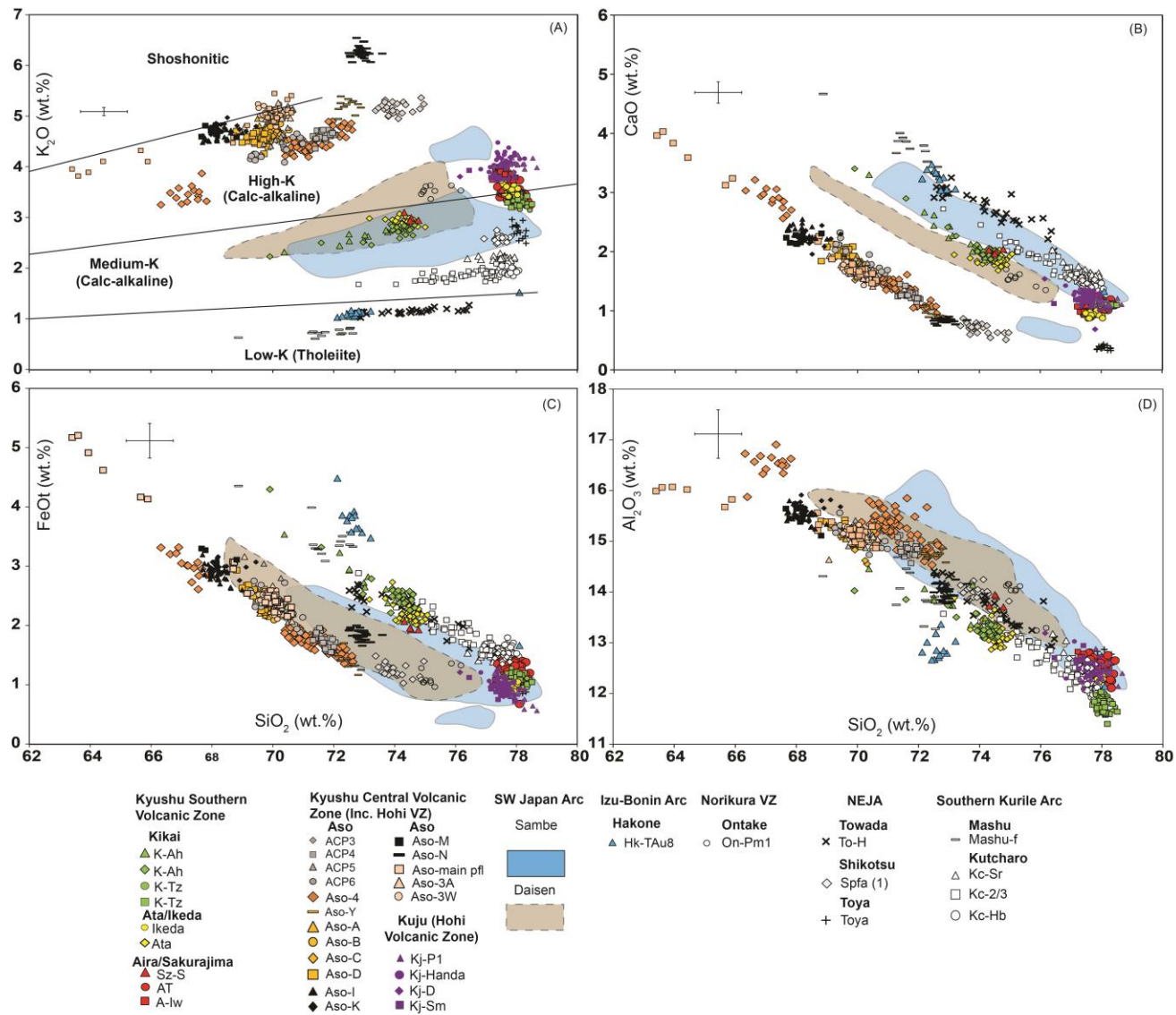
Figure 2
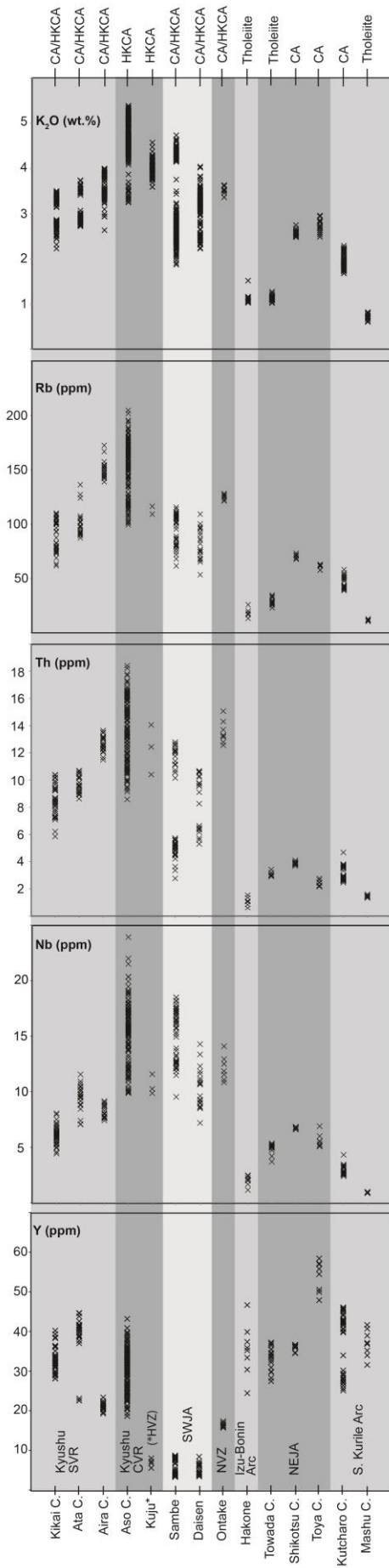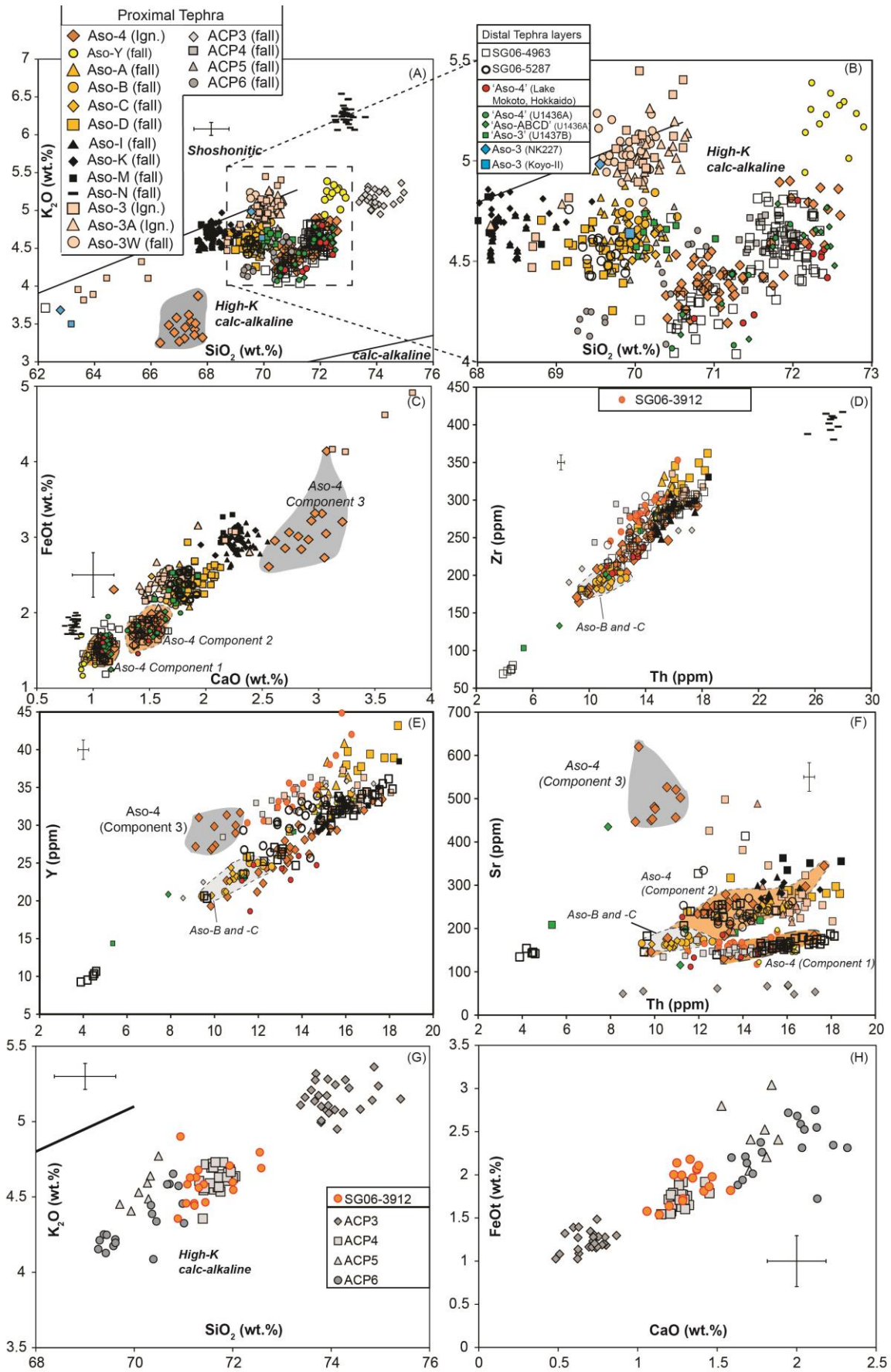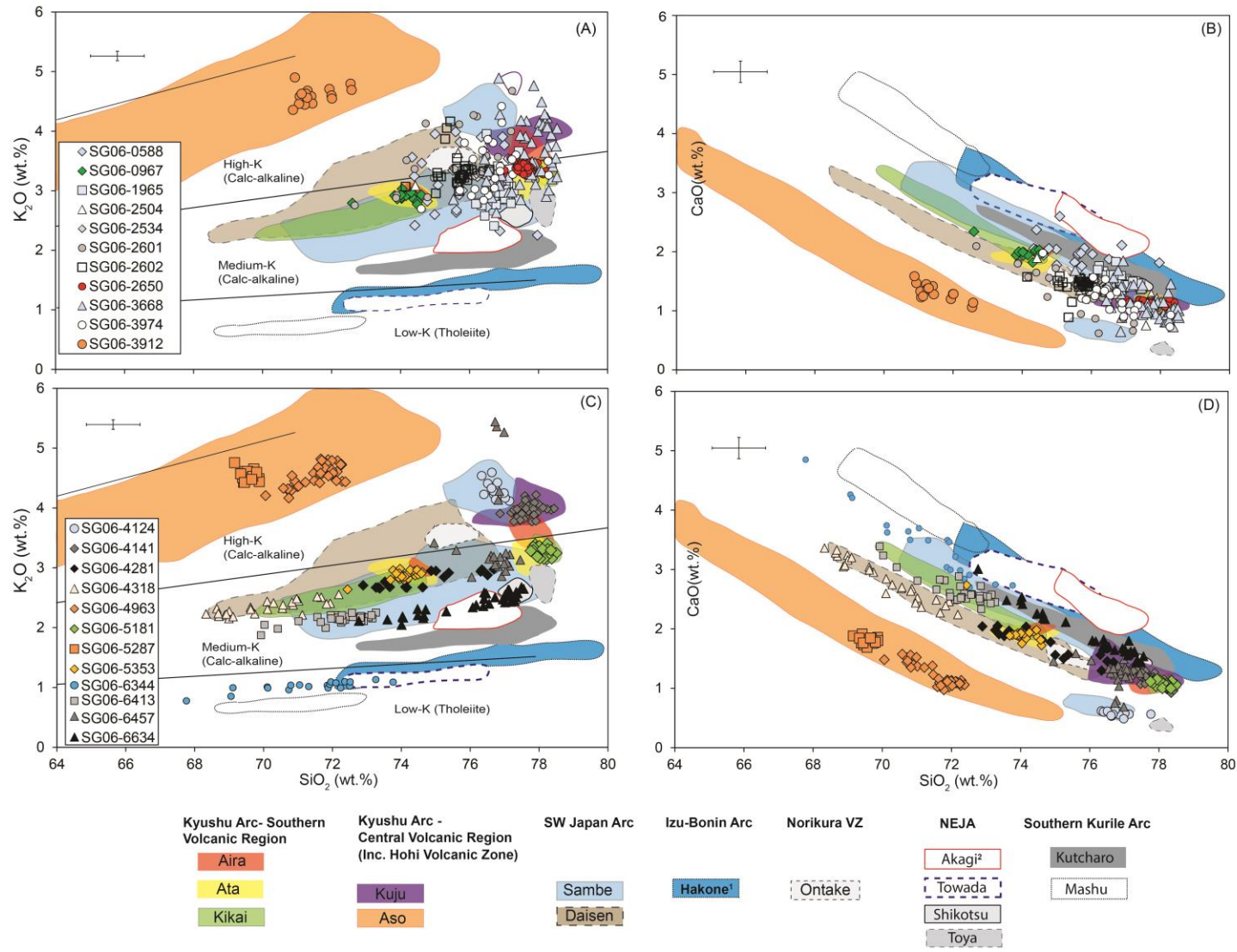
Figure 3

Figure 4

Figure 5

Figure 6

Figure 7

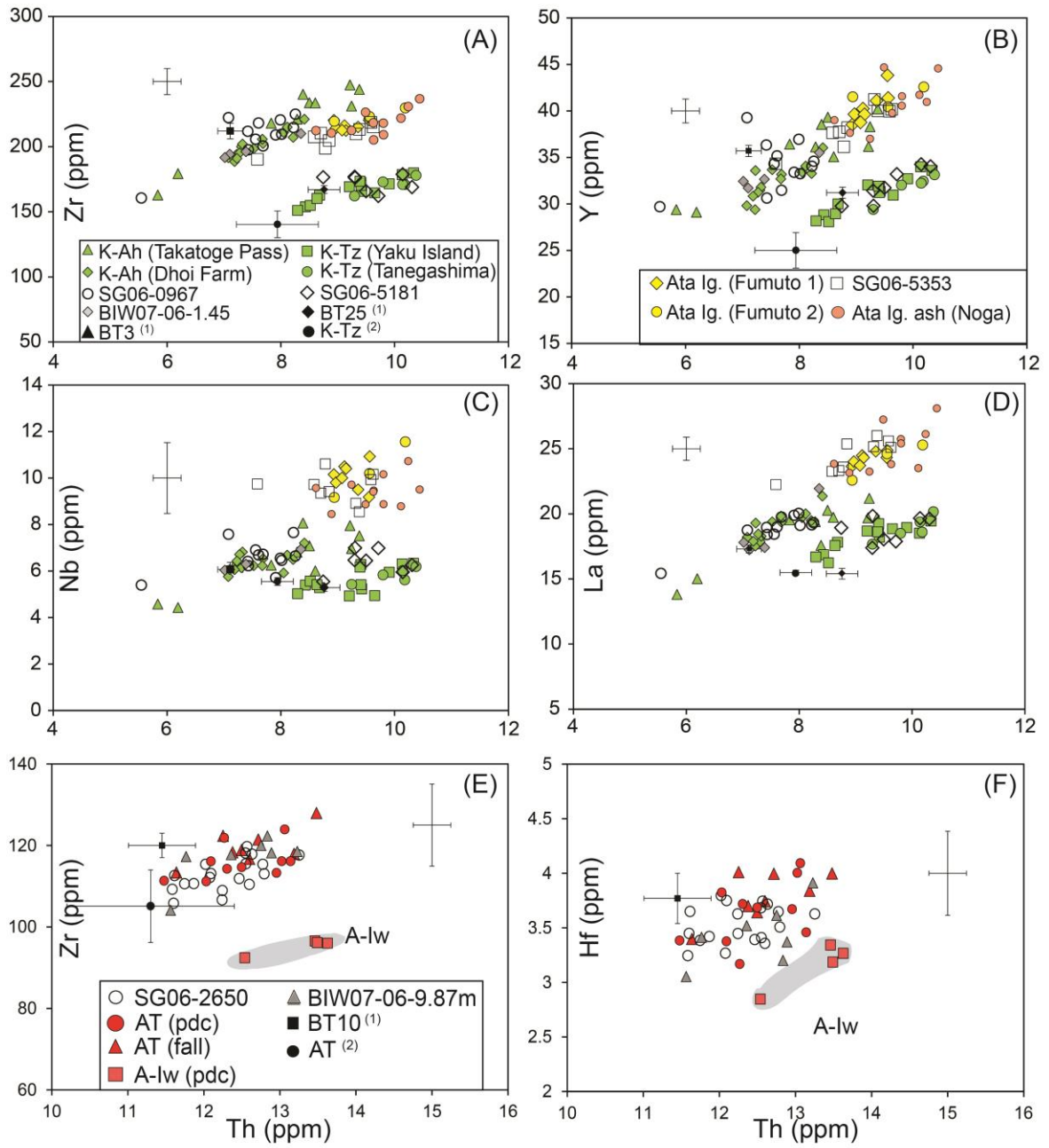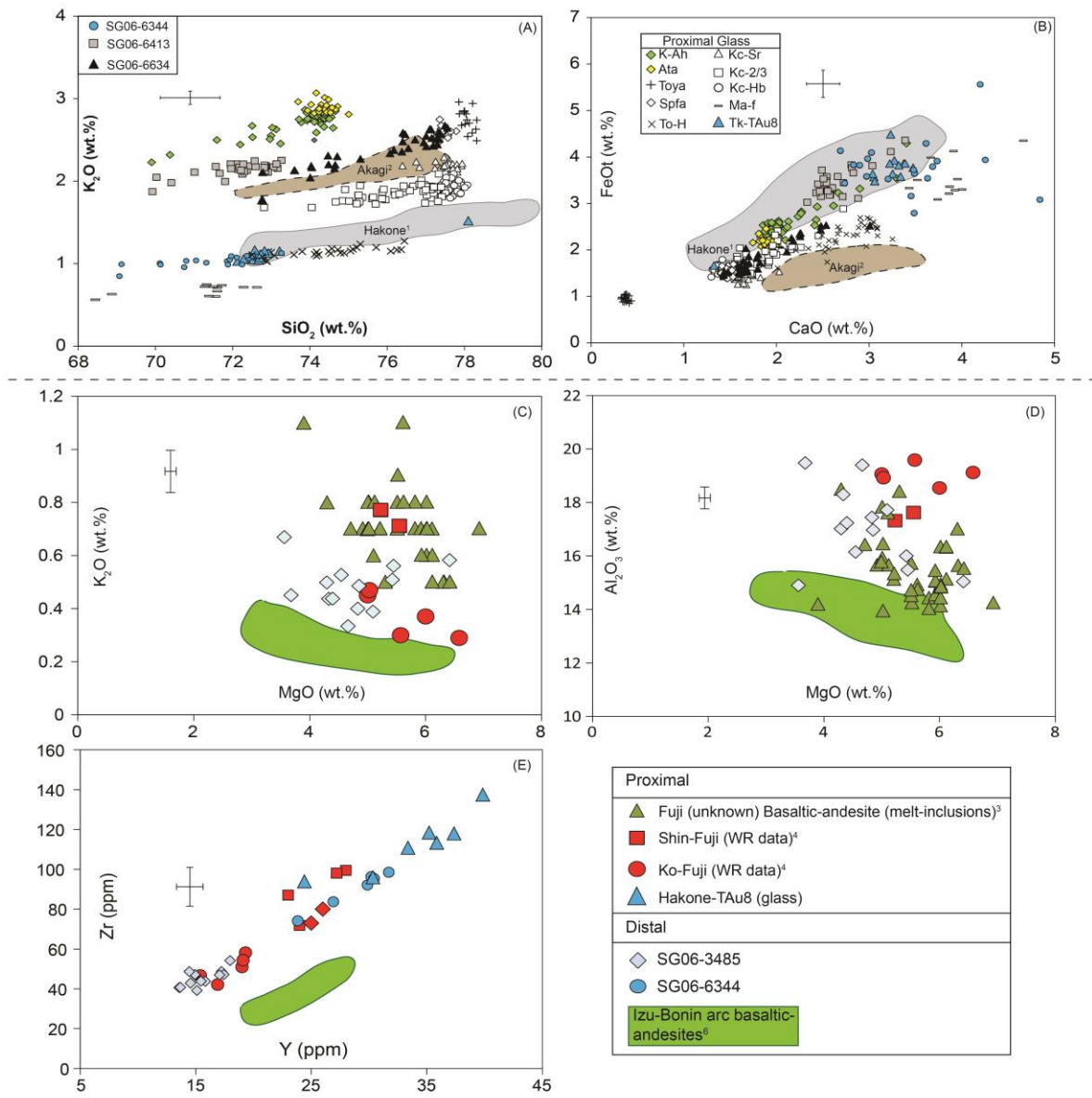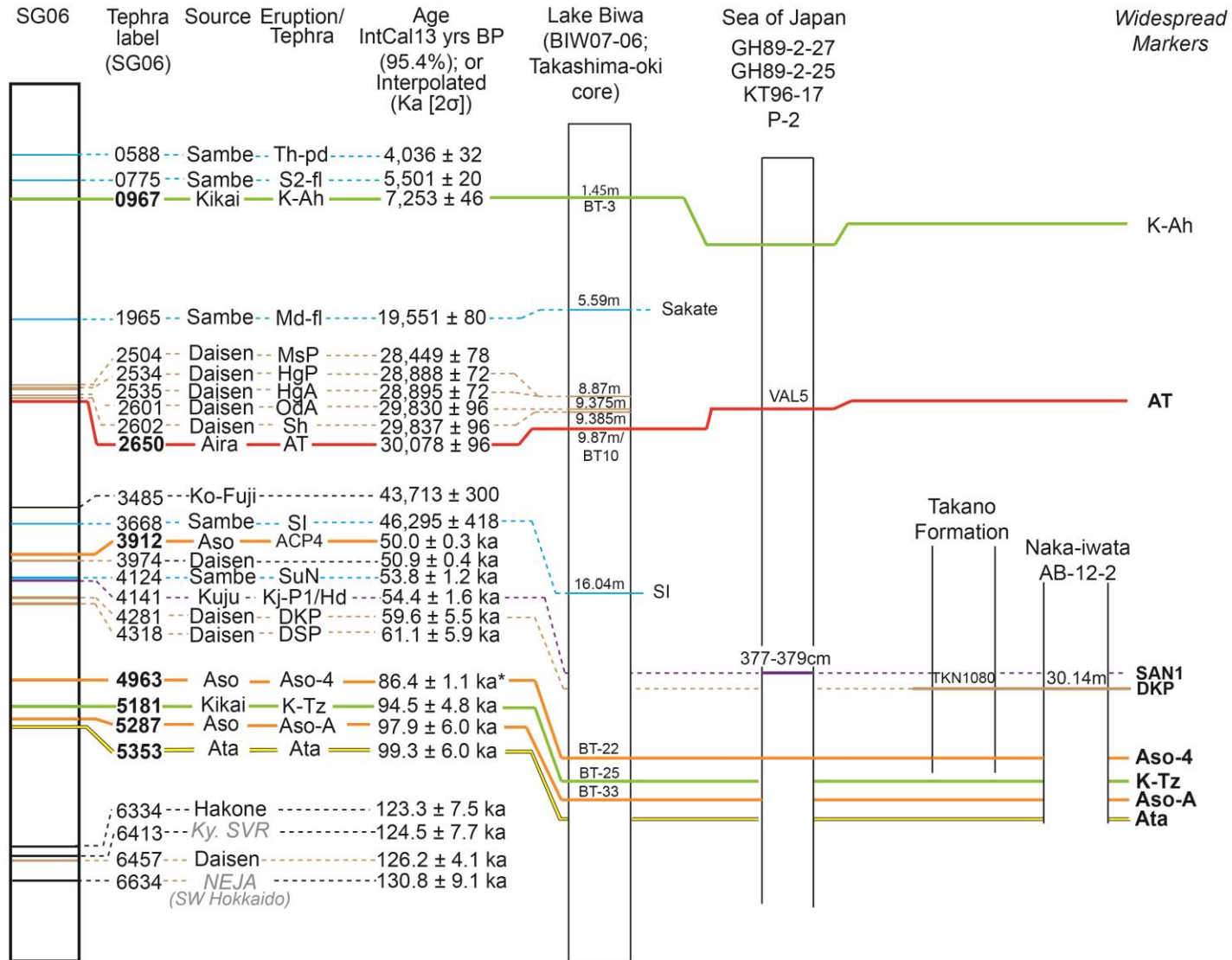# SG06 tephra- Excluding SWJA (Daisen - Sambe) derived layers
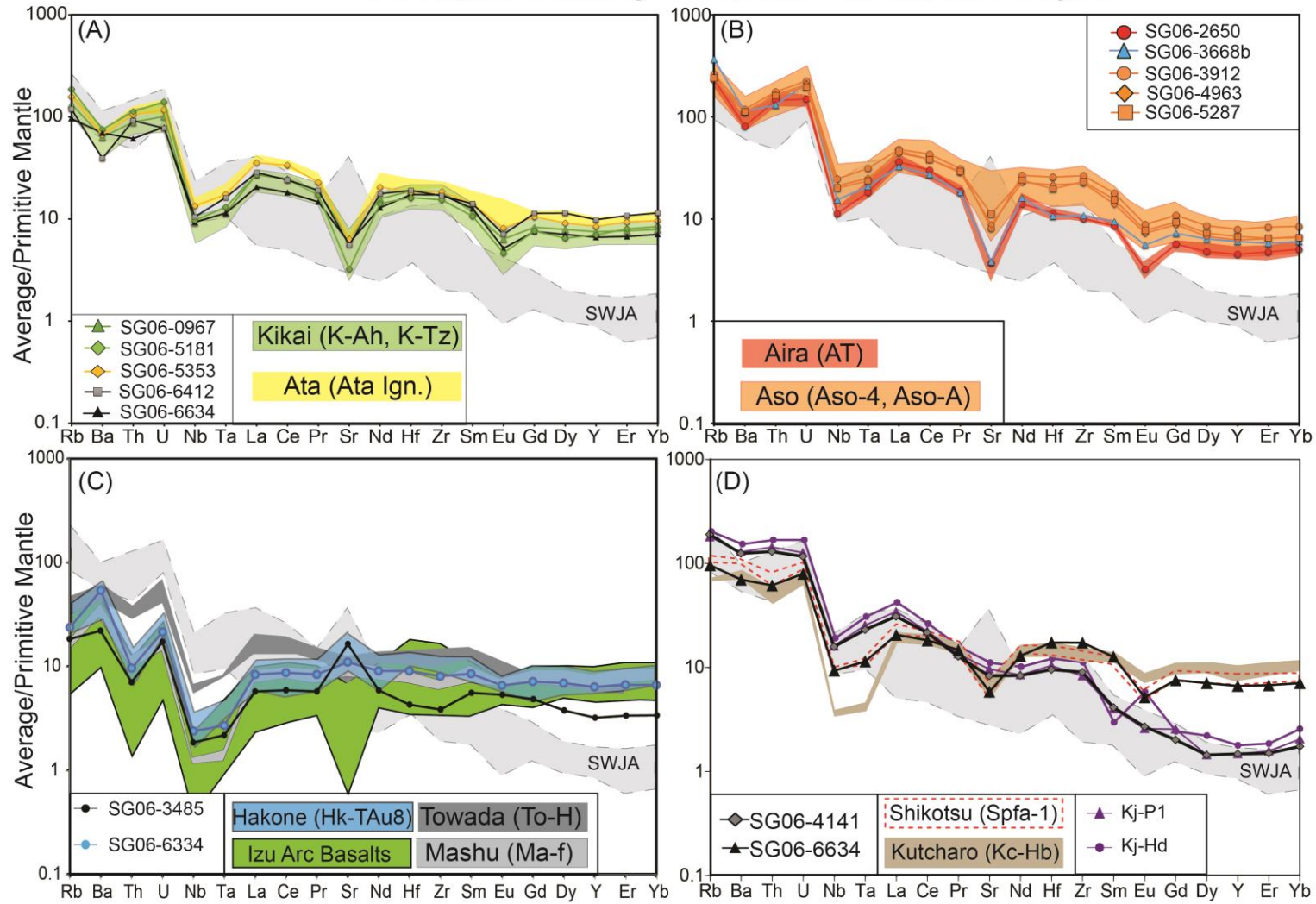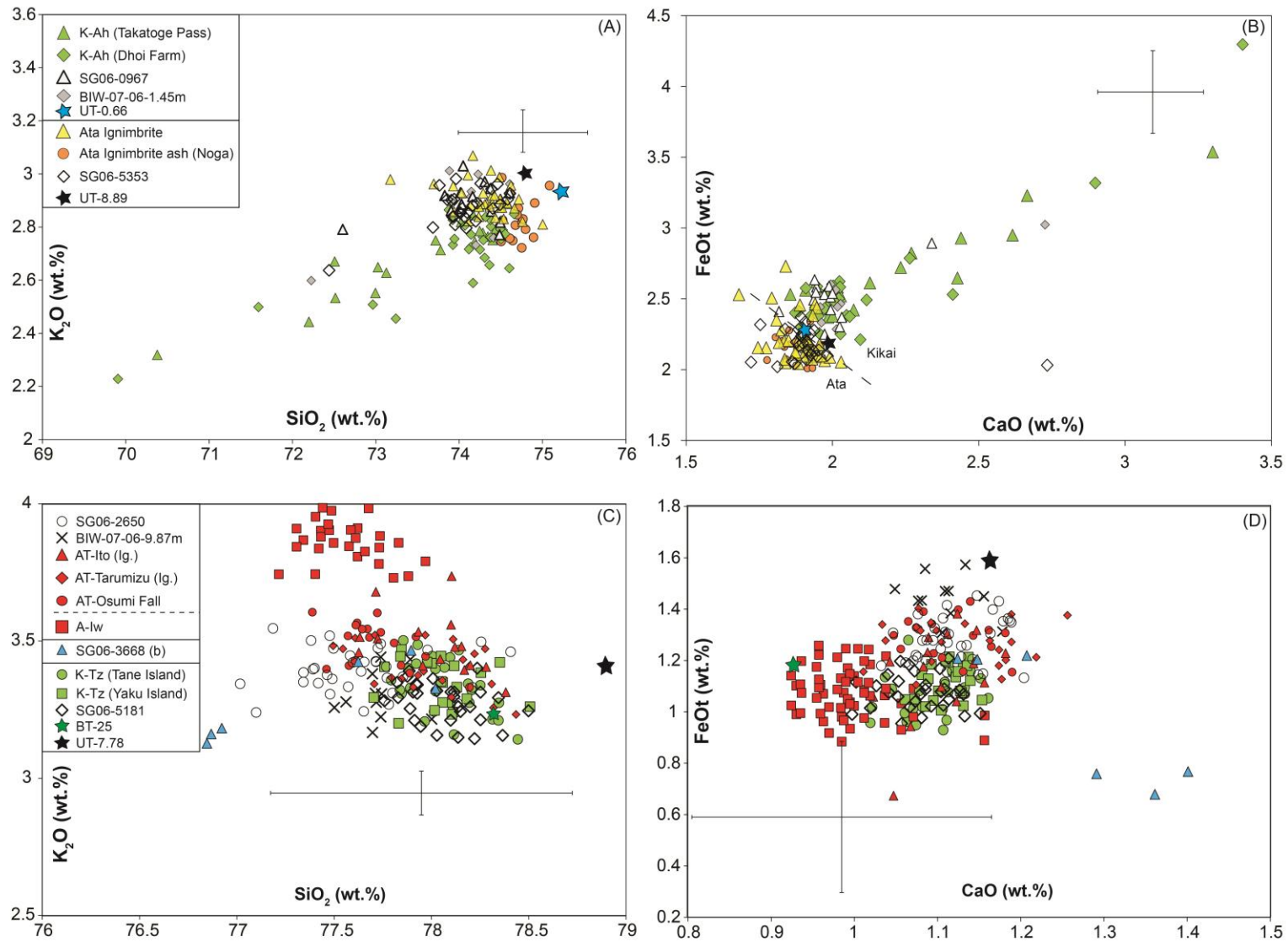

Figure 8

Figure 9

Figure 10

Figure 11

Supplementary Figure 1